NORTHWESTERN UNIVERSITY

Calibrating and Applying Sedimentary Leaf Wax Hydrogen Isotopes to Reconstruct Hydroclimate of Greenland during the Holocene and Last Interglacial

A DISSERTATION

SUBMITTED TO THE GRADUATE SCHOOL

IN PARTIAL FULFILLMENT OF THE REQUIREMENTS

for the degree

DOCTOR OF PHILOSOPHY

Field of Earth and Planetary Sciences

By

Jamie Marie McFarlin

EVANSTON, ILLINOIS

June 2019

Abstract

Records of temperature and precipitation during Quaternary interglacial periods on Greenland are notably scarce, limiting assessment of the magnitude and rate of local environmental response to orbitally-driven Arctic warming. It is largely unknown if warming across Greenland was spatially uniform through past interglacials, and if warming was accompanied by major changes to the hydrologic cycle, both of which have implications for the size of the Greenland Ice Sheet (GrIS). This dissertation research calibrates the relationship between the hydrogen (H) isotopic composition of modern sedimentary plant waxes and that of precipitation in Greenland for use as a proxy for paleo-precipitation isotopes. The data presented here demonstrate a robust relationship between the H isotopic composition of long-chain sedimentary plant waxes, commonly ascribed to terrestrial plants, and local precipitation on Greenland. These calibration data are used to reconstruct the H isotopic composition of terrestrial leaf water from lacustrine sedimentary waxes, and then combined with independent proxy evidence for the O isotopic composition of lake water (O isotopes of chironomid larvae) and summer air temperature (chironomid species assemblages) from the same lake records. This paired-proxy approach is employed to reconstruct atmospheric moisture during the Last Interglacial (~129 to 116 ka) and the Holocene (11.7 to 0 ka) in northwest Greenland, and the Holocene in south Greenland.

In northwest Greenland at Wax Lips Lake, maximum summer air temperatures during the Last Interglacial and Holocene, inferred from chironomid species assemblages, indicate pronounced regional warming. This warming was accompanied by relatively wet conditions, as evidenced by leaf water and lake water that are statistically indistinguishable. In contrast, during the cool late Holocene leaf water is significantly ^{2}H-enriched relative to lake water, indicating arid conditions that promoted evapotranspiration during the summer growth season. Relating these data

to published records of the extent of the GrIS through the Holocene indicates the local margin responded to summer air temperature more strongly than to atmospheric moisture. The maximum local retreat of the GrIS occurred during the early Holocene, a period characterized by high relative humidity and relatively warm summers. In contrast, re-advance of the local GrIS occurred during the cool late Holocene, when relative humidity, and by inference precipitation amounts, in northwest Greenland were relatively low.

In south Greenland, a comparison of the H isotopes of leaf wax to the O isotopes of chironomids at Pincushion Lake indicates no significant changes in relative humidity over the past 10,000 years (i.e. no periods when leaf water was enriched relative to lake water, indicative of arid conditions), likely reflecting a consistently wet maritime climate for much of the Holocene. Although other records from southwest, west, and southeast Greenland indicate periods of notable aridity during the Holocene, these records disagree on the timing of relatively wet vs. dry conditions. O isotopes in ice cores and dating of glacial geologic features indicate changes in the elevation and extent of the south GrIS through the Holocene, with major retraction in the early Holocene. Although there is no evidence from this data for arid conditions during the Holocene, the H isotopes of leaf wax express a similar magnitude of change in precipitation isotopes over the Holocene as isotopes of ice at NGRIP and GRIP. This suggests other climate drivers, in particular higher summer temperature in the early Holocene, were likely responsible for changes in the extent of the south GrIS.

This dissertation adds to the literature new plant biomarker data from Greenland across a broad climate gradient, and further advances biomarker methods by calculating water isotopes from proxy isotope data using new Greenland-specific calibrations, facilitating interpretation of isotopic changes in these proxies through geologic time.

Acknowledgements

The research presented in this dissertation was enabled by a warm community of people at Northwestern University, who offered years of guidance, insight, and support. I have appreciated the invaluable department staff, who helped with everything, from submitting grant proposals to printing posters; the academic faculty, for their dedication to teaching and eagerness to share knowledge; my graduate and undergraduate student peers, past and present, who provided comradery and motivation along the way; and my dearest friends here in Evanston, Renee French, Paul Hartzog, and Amanda Bartosiak, for being there for me through thick and thin.

Much of this work was collaborative, with laboratory assistance from members of the community here at Northwestern and beyond. In particular, I'd like to acknowledge and thank Andy Masterson, Melissa Chipman, Hannah Dion-Kirschner, Sohyun Lee, Jordan Todes, and Grace Schellinger for their help and scientific insight which directly improved this work.

The completion of this dissertation is a testament to the mentoring I received throughout my graduate career from my thesis committee: Yarrow Axford, Maggie Osburn, and Brad Sageman. I'd like to thank Brad, for being such a positive voice and such a wonderful teacher. I'd like to thank both of my PhD advisors, Maggie Osburn and Yarrow Axford, for not just encouraging me to scientifically explore, but also constantly providing the support to do so. And because it is the humans behind it that ultimately shape the work: Yarrow, thank you for sharing your passion, your creativity, and for opening the door for me to the world of Arctic climate and paleoclimate. You lit a fire. Maggie, thank you for fanning the flame. You took me on as your student sight-unseen, inspired me to work hard, and taught me how to be a better, braver scientist. It was the example set here between you both that helped me define what I hope to achieve.

Dedication

To my mother, for her example of kindness. To my sister, who taught me grit. To my brother, who inspired me to be creative. To my nephews, who brought such joy to my life. To my father, who showed me courage and wit.

And to my husband, who embodies them all.

Table of Contents

List of Tables

List of Figures

Chapter 1

Introduction

Arctic amplification of ongoing global warming drives faster change in high latitude regions of the northern hemisphere than the global average (Serreze et al., 2009; Miller et al., 2010). Annual surface air temperature at the Thule Air Base in northwest Greenland, for example, rose by at least 1.5°C between 1952 and 2012, compared to the global average of ~1°C for the same period (Hartmann et al., 2013; Wong et al., 2015). In the most recent decades, this trend is even larger, with an increase in annual air temperature at Thule >3°C between 1991 and 2012 (Wong et al., 2015). Ultimately, this warming is primarily because of increasing CO_2 and other greenhouse gases in the atmosphere, and in 2013 the Intergovernmental Panel on Climate Change (IPCC) concluded that under all carbon emissions pathways, a warming trend will continue into the coming centuries (Collins et al., 2013). Understanding the ongoing and future repercussions of changing global surface temperature is a major scientific challenge, with few places so clearly at risk from warming as the world's polar ice sheets.

The Greenland Ice Sheet (GrIS) contains enough ice to raise global sea level by ~7 m were it to melt entirely. At present it is unclear what amount of warming will lead to a total loss of the ice sheet and how quickly that will occur (Alley et al., 2010; Collins et al., 2013; Leary et al., 2013; Dutton et al., 2015; Bierman et al., 2016; Schaefer et al., 2016). GrIS observations and evolution models suggest that the GrIS mass budget is a function of ice discharge and surface mass balance (melt vs. accumulation), with climatologic controls on these levers that include ocean temperature, surface air temperature, and snowfall totals (van den Broeke et al., 2009; Collins et al., 2013; Helsen et al., 2013; Vernon et al., 2013; Plach et al., 2018). One way to test how responsive the GrIS is to climatic change is to use geologic records to observe how the

landscape changed, including the extent of the GrIS, during past periods of insolation-driven warming, when temperatures were warmer-than-present.

In 2013, when I started this PhD work, much of what was known about climate on Greenland during past warm periods came from the oxygen isotopes of ice cores drilled across the GrIS. That year, the oldest continuous record of Greenland ice, a folded-ice core through the Last Interglacial Period (LIG) (~129-116 cal ky BP), was published in *Nature*. It revealed notably warm temperatures over the northern GrIS at the NEEM core site (exceeding temperatures observed in partial records of LIG ice at other core sites), but only a modest change in the elevation of ice at that site (Dahl-Jensen et al., 2013). This perplexing finding, sometimes referred to as the 'NEEM Paradox' in literature (Goelzer et al., 2016), has since proven difficult for GrIS evolution models to match (Goelzer et al., 2016; Yau et al., 2016). The temperature estimate at NEEM for the LIG has been replicated (Landais et al., 2016; McFarlin et al., 2018), including by data presented in this dissertation, which begs the question: what else is missing in the model(s) or the geologic record? This remains a very difficult question to answer because there are so few records from the LIG on Greenland.

In contrast, the most recent period of interglacial warmth, the Holocene (11.7-0 cal ky BP), post-dates the Last Glacial Maximum and so deposition from this period has not been subject to widespread glacial erosion. There were (and continue to be) many more published observations of Holocene climate and ice extent across Greenland, relative to the LIG, from a diversity of ice, lacustrine, and stratigraphic archives (Anderson and Leng, 2004; Andresen et al., 2004; Frechette and de Vernal, 2009; Vinther et al., 2009; D'Andrea et al., 2011; Axford et al., 2013; Carlson et al., 2014; Sundqvist et al., 2014; Winsor et al., 2014; Corbett et al., 2015; Gajewski, 2015; Larsen et al., 2015; Winsor et al., 2015; Briner et al., 2016; Farnsworth, 2016; Thomas et al., 2016; Axford et al., 2017; Lasher et al., 2017). A picture of temperature and ice

sheet history through the Holocene is beginning to emerge for regions of the island, although there are still large areas, especially on the eastern coast, that are missing in the paleoclimate literature. At present, it remains unclear if the timing and/or magnitude of Holocene warming across Greenland was spatiotemporally heterogeneous or homogenous (Kaufman et al., 2004; Vinther et al., 2009; Briner et al., 2016; Lecavalier et al., 2017). Interestingly, GrIS evolution models are also challenged by reducing the size of the Holocene ice sheet on parts of Greenland enough to match geologic observations of ice volume, given the (ostensibly low) modeled amplitude of temperature change in the early Holocene (Simpson et al., 2009; Lecavalier et al., 2013; Lecavalier et al., 2014; Liu et al., 2014). Combined with the NEEM paradox, this suggests that the overall understanding of GrIS dynamics and/or of past climate change over Greenland, assessed through geologic observation and models, is incomplete. The idea has been put forth that changes to precipitation with warming might help account for some of the GrIS observation-model discrepancies during the Holocene and LIG (Young and Briner, 2015; McFarlin et al., 2018).

Changes in the hydrologic cycle, all the components of which are here referred to collectively as hydroclimate, are particularly hard to reconstruct in geologic records and are thus underrepresented in Arctic paleoclimate literature (Sundqvist et al., 2014; Linderholm et al., 2018). Modern observations and climate models both demonstrate that precipitation in the Arctic increases with warming (Collins et al., 2013; Masson-Delmotte et al., 2015; Wong et al., 2015), but observations of this trend on Greenland are inconsistent for the Holocene (Alley et al., 1993; Eisner et al., 1995; Björck et al., 2002; McGowan et al., 2003; Andresen et al., 2004; Aebly and Fritz, 2009; Frechette and de Vernal, 2009; Anderson et al., 2012; Massa et al., 2012; Perren et al., 2012; Balascio et al., 2013; Thomas et al., 2016; Thomas et al., 2018) and nonexistent for the LIG. For the Holocene, this is in part because many hydroclimate proxies are only indirectly

related to precipitation amount (e.g. minerogenic changes in lacustrine sediment cores that are interpreted as more or less runoff), and in part because some of the advances in biomarker proxies that more directly relate to hydroclimate are recent (Castañeda and Schouten, 2011; Sachse et al., 2012; van Hardenbroek et al., 2018). Much of the pioneering work in using compound-specific hydrogen isotopes to reconstruct precipitation and moisture balance on Greenland was published during my career as a graduate student (Balascio et al., 2013; Thomas et al., 2016; Thomas et al., 2018). The coverage in these records is limited to three sites on the island and the proxy is largely qualitative (i.e. interpreted as evidence for generally more or generally less precipitation). A major limitation in quantitative interpretations of compound-specific hydrogen isotopes was that, prior to this work, it was unknown if these biomarker tools behaved on Greenland in a way consistent with the low- and mid-latitude regions where the proxy was calibrated (Liu and Yang, 2008; Yang et al., 2009; Yang et al., 2011; Shanahan et al., 2013; Daniels et al., 2018).

The work presented in this dissertation was designed to address some of the gaps in the literature discussed above: to contribute additional observations of climate on Greenland during the LIG and the Holocene, and to push forward the tools available to do so on the island. Here, I present work that spans from northwest to southern Greenland (Figure 1.1). In Chapter 2, I introduce a modern calibration of the relationship between hydrogen isotopes of compound-specific biomarkers in Greenland lakes to those of local precipitation. In Chapter 3, I reconstruct temperature using an independent proxy, chironomid species assemblages, through two interglacial periods, the LIG and the Holocene, on northwest Greenland. Chapter 4 combines my temperature reconstruction with observations of compound-specific hydrogen isotopes in northwest Greenland to understand both climate and hydroclimate in the region. And, in Chapter 5, I use compound-specific hydrogen isotopes to reconstruct the isotopes of precipitation in south

Greenland through the Holocene. The results of this work can be used to understand the magnitude of warming and some of the associated change(s) in hydroclimate on parts of Greenland during the LIG and the Holocene. This information can then be combined with other geologic observations, including GrIS extent, to assess regional sensitivity to warming.

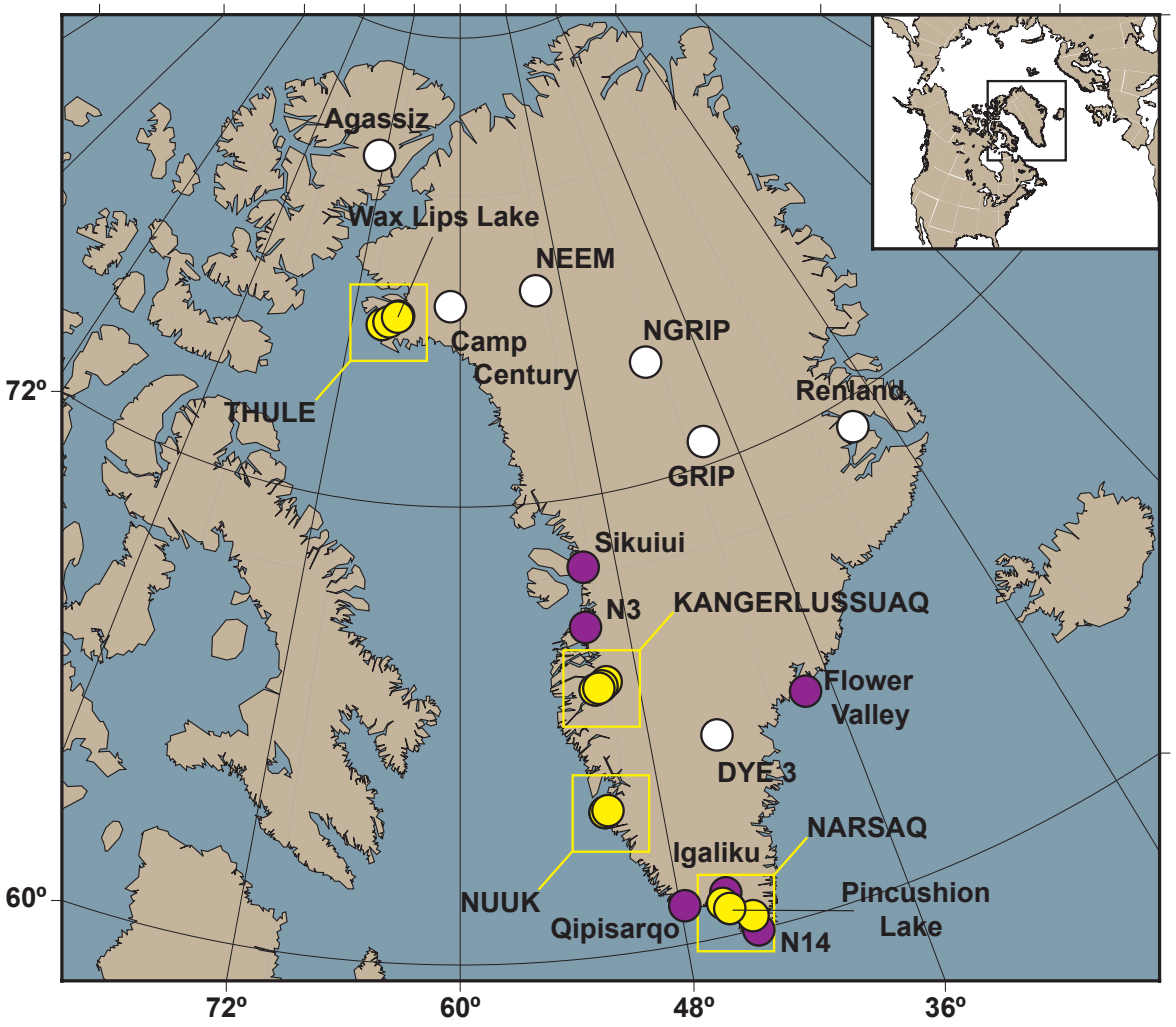

Figure 1.1 *Map of all field sites relevant to the work presented or discussed in this dissertation. Yellow squares highlight the major regions covered in this work: Thule, Kangerlussuaq, Nuuk, and Narsaq. Yellow circles within each square identify the location of the individual lakes utilized in the analyses presented here. Purple circles indicate published lake records that are discussed in this text, while white circles represent major ice core sites. Inset shows location of Greenland within a North American context.*

Chapter 2

Calibration of the modern sedimentary δ^2H wax-water relationships in Greenland lakes

2.1 Abstract

Sedimentary leaf waxes are an important paleohydrologic proxy in sedimentary records. Modern syntheses from middle and low latitudes demonstrate strong correlations between hydrogen isotopic values (δ^2H_{VSMOW}) of long-chain sedimentary waxes and those of mean annual precipitation (Sachse et al., 2012). However, these syntheses are largely missing high latitude lakes, where extreme climate and light conditions may impact both plant physiology and growth water in the surrounding watershed. This chapter presents modern sedimentary *n*-alkane and *n*-alkanoic acid data from a 22-lake transect extending from northwest to southernmost Greenland, covering a large latitudinal and climatic gradient. These data demonstrate a strong correlation (r=0.8-0.9) between δ^2H values of some sedimentary leaf waxes and those of precipitation, with *n*-alkanes more tightly correlated to precipitation than *n*-alkanoic acids. However, data here also demonstrate that δ^2H values of mid-chain sedimentary waxes, commonly ascribed to aquatic plants and mosses, correlate to those of precipitation, but do not correlate to the δ^2H values of lake water when it decouples isotopically from precipitation (i.e. in glacier-fed and evaporatively-enriched lakes). Greenland data are contextualized via an update of the global dataset of δ^2H values of sedimentary waxes and precipitation (Sachse et al., 2012) to include 100+ lakes from recently published literature, and indicate the average global offset between C_{29} *n*-alkanes and that of annual precipitation of ~120‰, first reported by Sachse et al. (2012), is remarkably consistent even including Arctic data.

2.2 Introduction

The reconstruction of past precipitation is currently limited by a lack of widely applicable, well-calibrated proxies. This is particularly problematic in the Arctic where few published studies report on past precipitation trends (Sundqvist et al., 2014; Linderholm et al., 2018), but where climate projections indicate substantial forthcoming changes in the hydrologic cycle. End-of-the-century predictions show, for example, an increase precipitation amount broadly over the Arctic driven by more winter snow (Collins et al., 2013). However, it is unclear specifically how the hydrologic cycle will change on regional scales, or how those changes may affect local landscapes and ecology.

Reconstructing the isotopic composition of local precipitation through time offers powerful insight into aspects of past hydroclimate because the partitioning of hydrogen (H) and oxygen (O) isotopes in meteoric water is a direct function of temperature, precipitation and evaporation (Dansgaard, 1964; Gat, 1996). In many middle to low latitude regions (0-60°), prior work has demonstrated that the δ^2H values of some modern sedimentary *n*-alkanes and *n*-alkanoic acids demonstrate a strong correlation with those of mean annual precipitation (Huang et al., 2004; Sachse et al., 2004; Hou et al., 2007; Polissar and Freeman, 2010; Sachse et al., 2012; Shanahan et al., 2013). This approximately linear relationship demonstrates that waxes are strongly ^2H-depleted relative to precipitation, with the average offset between the δ^2H values of C_{29} *n*-alkanes and annual precipitation ~120‰ (Sachse et al., 2012). A predictable offset allows for the reconstruction of precipitation δ^2H values using sedimentary plant wax δ^2H values from geologic archives. Because of this, the H isotopes of sedimentary leaf waxes (reported as δ^2H values relative to VSMOW), which empirically relate to δ^2H values of local precipitation have emerged as a popular proxy globally (Pagani et al., 2006; Tierney et al., 2008; Tierney et al.,

2011; Feakins et al., 2012; Thomas et al., 2012; Balascio et al., 2013; Contreras-Rosales et al., 2014; Hepp et al., 2014; Thomas et al., 2016; Thomas et al., 2018).

Terrestrial plants synthesize waxes to protect the leaf cuticle and regulate leaf water (Eglinton and Hamilton, 1967; Koch and Ensikat, 2008). The distributions of these compounds are source-specific by plant form, with long-chain odd *n*-alkanes ($>C_{25}$) and even *n*-alkanoic acids ($>C_{26}$) broadly ascribed to vascular plants, and mid-chain odd *n*-alkanes (C_{21}-C_{25}) and even *n*-alkanoic acids (C_{22}-C_{26}) primarily attributed to mosses and aquatic plant lipids (Eglinton and Hamilton, 1967; Baas et al., 2000; K. J. Ficken et al., 2000; Nott et al., 2000; Aichner et al., 2010; Bush and McInerney, 2013; Liu and Liu, 2016). Leaf wax *n*-alkanes are derived from decarboxylation of *n*-alkanoic acids during biosynthesis of waxes outside the chloroplast (Chikaraishi and Naraoka, 2007; Sachse et al., 2012) so that a given alkane is produced from an alkanoic acid with one additional carbon (nC *n*-alkane is a product of n+1C *n*-alkanoic acid, informally referred to here as "sets"). Because they are products of the same biosynthetic pathway in plants, *n*-alkanoic acids and *n*-alkanes are both used as a proxy for reconstructing paleo-water, with the assumption that they ultimately reflect the same source water (Castañeda and Schouten, 2011; Sachse et al., 2012). Sedimentary leaf waxes are geologically recalcitrant (Sessions, 2016) and globally ubiquitous in lacustrine archives, and are thus an important plant biomarker and paleohydrologic proxy.

In the Arctic, the modern relationship between δ^2H values of leaf waxes and those of precipitation is not well established, and recent work disagrees on whether the offset between the two in high latitude regions (60-90°) is consistent with the average offset observed in middle and low latitudes. Some experimental greenhouse work has suggested that a short but intense growth season with continuous sunlight has the effect of decreasing the biosynthetic isotope effect (Liu and Yang, 2008; Yang et al., 2009; Yang et al., 2011). This is supported by observational work

from Canada, Alaska, and Greenland that demonstrates δ^2H values of sedimentary, soil and modern leaf waxes from some high latitude sites exhibit smaller-than-average offsets by ~25-65‰ (Shanahan et al., 2013; Bakkelund et al., 2018; Berke et al., 2019). Proposed explanations for a reduced offset include a smaller biosynthetic fractionation effect, higher transpiration rates resulting in ^2H-enriched leaf water, and/or uptake of evaporatively ^2H-enriched soil water (Feakins and Sessions, 2010; Sachse et al., 2012; Shanahan et al., 2013; Bakkelund et al., 2018; Berke et al., 2019). In contrast, sedimentary waxes from other high latitude sites in Alaska, northern Europe, and Siberia show close agreement with (or larger offsets than) the average offset (Sachse et al., 2004; Wilkie et al., 2013; Daniels et al., 2017). And, other greenhouse work suggests that there is not a consistently-different biosynthetic fractionation effect in plants exposed to continuous light (Daniels et al., 2018). In Greenland, the calculation of paleo-precipitation isotopes from this proxy is limited because plant wax δ^2H values have not been evaluated from spatially-widespread observations on the island, and more broadly, because there is no consensus on the magnitude of the fractionation effect in Arctic regions.

Like reconstructions of past precipitation, reconstructions of lake water isotopes are also useful for insight into past hydroclimate. Lakes are integrative depending on the residence time, and therefore the isotopic composition of lake water for through-flowing lakes can mirror annual precipitation weighted towards the season(s) when most precipitation is delivered (Gibson et al., 2016). A reconstruction of the differences in leaf water and lake water from appropriate sites can yield useful insight into atmospheric moisture and precipitation, but the best approach for reconstructing the isotopic composition of Arctic lake water is also not firmly established. The δ^2H values of mid-chain waxes have been used to infer δ^2H values of past lake water (Balascio et al., 2013; Muschitiello et al., 2015; Thomas et al., 2016; Rach et al., 2017; Thomas et al., 2018).

An important caveat is that currently no large compilation of data exists that demonstrates δ^2H values of sedimentary mid-chain waxes correlate to δ^2H values of lake water where lake water deviates from precipitation. Further, very few studies report the modern offset between δ^2H values of aquatic plant waxes and those of lake water (Liu and Liu, 2016; Aichner et al., 2017) or the relationship between δ^2H values of sedimentary mid-chain waxes and those of lake water (Huang et al., 2004; Wilkie et al., 2013). Paleoclimate studies that use sedimentary mid-chain waxes to infer δ^2H values of past lake water rely on meaningful but indirect evidence: the observation that mid-chain *n*-alkanes and *n*-alkanoic acids are proportionally more abundant in non-vascular plant lipids than terrestrial leaf waxes (K. J. Ficken et al., 2000; Nott et al., 2000; Chikaraishi and Naraoka, 2003; Aichner et al., 2010; Gao et al., 2011; Rao et al., 2014; Aichner et al., 2017; Daniels et al., 2017); evidence from some regional studies which demonstrate a strong relationship between some mid-chain waxes and lake water (Huang et al., 2004; Sachse et al., 2012); that δ^2H values of mid-chain and long-chain waxes often behave differently in down-core records, and that these relative differences can be interpreted as lake water and leaf water without correction of biosynthetic isotope effects (Balascio et al., 2013; Thomas et al., 2016; Thomas et al., 2018).

As more and more terrestrial plants are tested for wax concentrations and chain-length distributions, it is increasingly evident that terrestrial plants in general synthesize 5-10x more lipids by volume than do aquatic plants (Aichner et al., 2010; Diefendorf and Freimuth, 2017; Freimuth et al., 2017), demonstrating that terrestrial plants can produce as much mid-chain wax as aquatic plants, despite that they dominantly synthesize long-chain waxes. This suggests that sedimentary mid-chain waxes are not necessarily derived from mostly non-vascular plants, so it

is important to test in modern lakes if mid-chain compounds still track lake water when the δ^2H values of lake water deviate from those of precipitation.

Here, to improve our understanding of the sedimentary δ^2H wax-water proxy in mid to high latitudes, we present a new calibration of sedimentary compound-specific isotopes from modern (surface) sediments in a transect of 22 lakes representing a large latitudinal and climate gradient across Greenland. We discuss sedimentary compound abundance, δ^2H values, and carbon isotope values ($\delta^{13}C_{VPDB}$) of mid and long-chain *n*-alkanes and *n*-alkanoic acids. We examine the relationship between δ^2H values of sedimentary waxes and those of precipitation and lake water. In light of our new Arctic dataset and data published since Sachse et al. (2012), we present an updated and expanded global synthesis of sedimentary C_{28} *n*-alkanoic acids and C_{29} *n*-alkanes. Our Greenland data, and the coherence of these data within the newly expanded global framework, reveal exciting potential for extending the application of long-chain *n*-alkanes and *n*-alkanoic acids to reconstruct the H isotope composition of precipitation in Greenland and other Arctic regions.

2.3 Methods

Site information

Sampling of 22 lakes along the west coast of Greenland (Table 2.1) (Figure 2.1) occurred during summer field seasons (July-August) from 2014-2016. Lakes were sampled for modern surface sediments by carefully collecting one sample of the undisturbed top 1-3 cm of sediment in an Ekman dredge, from the depocenter of each lake where it could be accessed (in most cases). Each sample was collected into either an ashed glass jar or a teflon bag, and stored frozen until analysis. Surface lake water was also collected from each lake at the time of sediment

collection for all lakes. Additional surface water samples were taken over multiple summers for some lakes where possible.

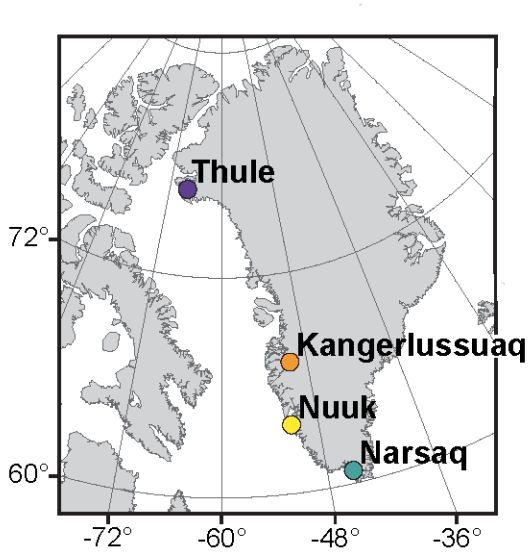

Figure 2.1 *Regions represented by lake transect across Greenland*

Lakes in the sample suite are situated along the ice-free margin of Greenland's western coast and are dominantly small (<1 km^2) and nonglacial, although six glacial lakes (lakes receiving meltwater from glaciers) are also included in the study. Sampled lakes span almost 20-degrees in latitude (76.85°N to 60.38°N) and include high-to-mid Arctic, low Arctic and sub-Arctic climate zones (Table 2.2). Mean annual precipitation across the transect ranges from ~100-900 mm/yr, mean annual air temperature ranges from -11 to 1°C, and mean July air temperature ranges from 4-11°C (Cappelen et al., 2001). This transect covers different high-latitude growth conditions including very cold and arid (Thule in the northwest), relatively warm and arid (Kangerlussuaq in the west) and relatively warm and wet (Nuuk and Narsaq in the southern west and south). The δ^2H values of mean annual precipitation span a range of ~100‰ over the sampling transect (Bowen and Revenaugh, 2003; Bowen, 2018). These regions are exposed to between 16 and 24 hours of sunlight daily in the summer months.

Laboratory and Data Processing Methods

Water isotopes (δ^2H, $\delta^{18}O_{VSMOW}$) of lake water were measured on a Picarro Water Isotope Analyzer following each field season. Water samples were measured in 8 or 9-fold replicates and

Table 2.1 Metadata for lakes included in the Greenland transect. Lake water isotopes were measured on samples collected during summer field season(s), with * indicating lakes in which water samples were collected in 2015 and 2016 and ** indicating lakes in which water samples were collected in 2014, 2015 and 2016. Error on these lakes represents the standard deviation of lake water δ^2H-values over different collection years. Precipitation isotopes are estimated using the Online Isotopes of Precipitation Calculator (Bowen et al, 2018) with summer precipitation an average of June, July and August δ^2H-values. DTB=Depth to bottom; c=closed, t-f=through-flowing, g=glacial

Lake	Region	Lat (°N)	Long (°W)	Elev (m asl)	Surface Area (km^2)	Max DTB (m)	Lake Type	δ^{18}O lake water	δ^2H lake water	δ^2H annual precip	δ^2H summer precip
STR	Thule	76.67	-67.94	224	<0.1	4.4	t-f	-22	-168	-181±1	-140
WLL	Thule	76.85	-66.96	517	<0.1	9	t-f	-18	-153	-187±2	-144
NS1	Thule	76.82	-67.05	455	<0.1	16	g, t-f	-22	-174	-186±2	-143
SEC	Thule	76.58	-68.66	248	<0.1	3.4	t-f	-18	-143	-181±1	-140
USHL	Kangerlussuaq	67.15	-50.13	340	0.1	18	g, t-f	-28	-222	-147±11	-122
SHL**	Kangerlussuaq	67.15	-50.13	335	<0.1	7	g, t-f	-29	-222±1	-146±11	-122
RTL1	Kangerlussuaq	67.15	-50.08	443	<0.1	3	C	-13	-118	-148±11	-123
RTL2*	Kangerlussuaq	67.14	-50.08	449	<0.1	1.5	C	-9	-103±4	-148 ±11	-123
RTL3*	Kangerlussuaq	67.06	-50.45	170	<0.1	1.8	C	-9	-97±3	-140±13	-118
RTL4	Kangerlussuaq	67.01	-50.67	112	<0.1	0.6	C	-11	-114	-137±13	-116
RTL5*	Kangerlussuaq	66.98	-50.92	65	<0.1	1.3	C	-7	-91±10	-135±14	-113
LSL*	Kangerlussuaq	67.05	-50.52	124	<0.1	3.4	C	-6	-89±10	-139±13	-116
LHN*	Kangerlussuaq	66.98	-50.93	122	0.4	5.2	C	-9	-93±3	-136±14	-113
T1	Nuuk	63.76	-51.36	75	<0.1	~10	t-f	-14	-97	-107±7	-93
T2	Nuuk	63.76	-51.37	57	<0.1	~15	t-f	-14	-97	-106±7	-93
T3	Nuuk	63.75	-51.35	30	1.8	≥20	g, t-f	-16	-115	-106±7	-93
PLK	Nuuk	63.80	-51.19	76	0.2	~25	g, t-f	-17	-116	-107±7	-93
PIN	Narsaq	60.70	-45.41	480	<0.1	14.8	t-f	-13	-98	-96±2	-85
SCP	Narsaq	60.70	-45.42	475	<0.1	7.4	t-f	-14	-100	-96±2	-85
NAR	Narsaq	60.87	-45.72	766	<0.1	26.2	t-f	-14	-100	-101 ±3	-88
LNR	Narsaq	60.87	-45.72	751	<0.1	9	t-f	-14	-100	-101 ±3	-88
TUP	Narsaq	60.38	-44.30	145	1.6	77	g, t-f	-17	-121	-89 ±2	-85

Table 2.2 Regional Climate Information (Cappelen et al., 2001; Jensen and Christensen, 2003)

Region	Mean July Air Temp (°C)	Mean Annual Air Temp (°C)	Mean Annual Precipitation (mm/yr)	Climate Zone	Vegetation Zone(s)	Permafrost Zone
Thule	4.5	-11.1	127	high and mid-Arctic	middle Arctic continental	continuous
Kangerlussuaq	10.7	-5.7	149	low-Arctic	low Arctic oceanic and low Arctic continental	continuous and discontinuous
Nuuk	6.5	-1.4	752	low-Arctic	low Arctic oceanic and low Arctic continental	sporadic
Narsaq	7.2	0.9	858	low and sub-Arctic	low Arctic oceanic and subarctic continental	sporadic

reported lake water isotope values are the average of the last 5 replicates in the measurement series, corrected to known standards and calibrated to the VSMOW scale. Prior to analyses, sediment samples were lyophilized and homogenized. Lipids were extracted from dried bulk sediments via a MARS Microwave Extractor™ in 9:1 DCM: MeOH. The reaction program included a 5-minute ramp to 100°C, 20-minutes at 100°C, and a 30-minute cool down period. Total lipid extracts (TLEs) were filtered using 100 μm ashed-glass filters and DCM to remove particulate matter and saponified for 12-18 hours in 0.5 M NaOH. Hydrolyzed lipids were acidified and extracted 3x with methyl tert-butyl ether (MBTE) prior to separation into fractions (alkanes, alcohols, and acids) using Discovery® amino-propyl solid phase extraction (SPE) columns. Saturated *n*-alkanes and *n*-alkanoic acids were additionally separated from unsaturated compounds using Discovery® Ag-ion solid phase extraction columns. To each separate fraction, 10 μg of palmitic acid isobutyl ester (PAIBE) was added to each fraction as an internal quantification standard. Purified *n*-alkanoic acid fractions were derivatized by esterification using BF_3/MeOH prior to quantification by gas chromatography using a Thermo Scientific Trace 1310 gas chromatograph (GC) with a ZB5 30m x 0.25 mm ID x 0.25 μm film thickness (Zebron) column coupled to Flame Ionization Detector (FID) and a Thermo ISQ LT single quadrupole mass spectrometer. The GC oven ramped from 100°C to 330°C over ~45 minutes. Compounds

were identified via diagnostic mass spectra, comparison to the NIST library, and retention times relative to laboratory standard compounds. Waxes were quantified using FID peaks, and concentrations were calculated from peak areas through comparison to that of the internal standard (PAIBE) in every sample.

Compound specific carbon ($^{13}C/^{12}C$) and hydrogen ($^{2}H/H$) isotope analyses (CSIA) were conducted via gas chromatography isotope ratio mass-spectrometry (GC-IRMS) using a Thermo Scientific Trace GC with a ZB5-5MS 30m x 0.25 mm ID x 1 μm film thickness column coupled to a Thermo Delta V Plus IRMS via a pyrolysis (P) or combustion (C) interface and controlled by a Thermo GC-C III. Reactions for GC-P-CSIA occurred in an alumina column at 1420ºC with a flow of 1.4 mL/min, and for GC-C-CSIA occurred in an oxidizing reactor consisting of Cu/Ni/Pt at 940°C. Tank calibration to the VSMOW and VPDB scales utilized a C_{16}-C_{30} *n*-alkane standard (A6, Arndt Schimmelmann, Indiana University) and a derivatized C_{14}-C_{20} fatty acid standard (F8, Alex Sessions, Caltech). Instrumental error was assessed via root mean standard error (RMSE) on standards A6 (alkanes) and F8 (acids), which were run in duplicate between every ~3 sample duplicates and averages ~3.5 (alkanes) and ~5 (acids). The H_3^+ factor was determined and applied daily and ranged from 5.20 to 5.52 ppm/nA during the analytical period. For each sample, the alkane and acid fractions were measured in duplicate for $^{2}H/H$-CSIA and for $^{13}C/^{12}C$-CSIA. Compound-specific $\delta^{2}H$ and $\delta^{13}C$ values are reported as average duplicate values on the VSMOW and VPDB scale, respectively. Additionally, sediment from the same Ekman grab was extracted twice and analyzed independently for six lakes, and for these lakes $\delta^{2}H$ and $\delta^{13}C$ values on sample replicates were averaged into the CSIA value for that lake. Total analytical error presented on $\delta^{2}H$ and $\delta^{13}C$ values includes the 1σ of measurements on each compound peak as well as the instrumental error over the course of all sample measurements,

propagated using the root sum of squares (RSS). The δ^2H and $\delta^{13}C$ values of *n*-alkanoic acids were corrected for isotopic addition from methyl groups introduced during esterification using a simple mass-balance equation, after measuring the isotope values of H and C in the MeOH via esterification of a phthalic acid of known H and C isotopic value (δ^2H_{MeOH} = -51‰ Batch 1, and = -83‰ Batch 2). Error from this correction was also propagated into the RSS for error on acids.

Precipitation δ^2H values at each sampling location in Greenland were estimated using the Online Isotopes of Precipitation Calculator (OIPC) for mean annual precipitation and summer precipitation, from averaged δ^2H values of June-August, the Arctic growth-season (Bowen and Revenaugh, 2003; Bowen et al., 2005; Bowen, 2018). We report the error associated with this estimation on annual precipitation, but not summer as the OIPC does not provide error on monthly values. Additionally, OIPC estimates were also re-calculated for every lake included here in the global synthesis (see Discussion) as the database is known to change significantly over time as it expands.

2.4 Results

Leaf wax abundance in transect sediments

Leaf wax *n*-alkanes and *n*-alkanoic acids are generally abundant compounds in sediments of nonglacial Greenlandic lakes. The average concentration of each compound ranges from 0.7-4.6 µg/g dry sediment in nonglacial lakes, while wax concentrations in glacial lakes are ~15-20% of that of nonglacial lakes owing to the larger clastic sedimentary inputs. The largest molecular-weight compounds, C_{30} *n*-alkanoic acids and C_{31} and C_{33} *n*-alkanes, occur in low concentrations in almost all lakes (<2 µg/g dry sediment); C_{31} *n*-alkanes are abundant (>2 µg/g dry sediment) only in sediments from lakes in the southern parts of the transect (Nuuk, Narsaq) and C_{33} *n*-

alkanes are abundant only in the southernmost part of the transect (Narsaq). C_{21} *n*-alkanes occur in low concentrations (<2 μg/g dry sediment) in almost all lakes as well. On average, C_{24} is the most abundant sedimentary *n*-alkanoic acid (~29% of reported compounds), and C_{25} and C_{27} are the most abundant sedimentary *n*-alkanes (19% and 19%, respectively).

Sedimentary wax hydrogen isotope data

The δ^2H values of sedimentary plant waxes span a range from -160 to -331‰. Average δ^2H values of wax compounds broadly follow the latitudinal gradient of the transect, with sedimentary plant waxes in the coldest, northern-most sites more ^2H-depleted than those in the southern-most sites. When all regions of the transect are included, *n*-alkanes are on average modestly ^2H-depleted (~4‰) with respect to their antecedent acid, although a student's t-test indicates this difference is not significant (p-value = 0.28). Further, only some sedimentary *n*-alkanes are ^2H-depleted relative to the antecedent *n*-alkanoic acid (e.g. the average value for C_{24} *n*-acid is more ^2H-depleted than the average value C_{23} *n*-alkane), despite that wax alkanes biochemically derive from acids, and so are expected to be somewhat depleted relative to the antecedent acid (Chikaraishi and Naraoka, 2007). When assessed by regional trends, the relationship between sedimentary was sets is highly variable (e.g. C_{26} *n*-acid is slightly ^2H-depleted compared to C_{25} *n*-alkane in Kangerlussuaq, whereas this is reversed in Thule, Nuuk and Narsaq).

Correlations between waters and sedimentary leaf waxes

Pearson's pairwise correlation tests on the δ^2H values of *n*-alkanes, *n*-alkanoic acids, and environmental waters indicate *n*-alkanes and *n*-alkanoic acid sets are highly correlated (r=0.8-0.9) (Figure 2.2). However, we also find that comparison of random sets (e.g., *n*-alkanes and *n*-

alkanoic acids not thought to be directly related by biosynthesis) are also highly correlated (e.g., C_{23} *n*-alkane and C_{28} *n*-alkanoic acid, r = 0.8). These high correlations between sedimentary alkane-acid sets could be due to the biosynthetic processing of *n*-alkanes directly from their *n*-alkanoic acid precursor, or just to the inherent isotopic similarity in plant biomolecules produced using the same growth water. That said, the generally high correlation between long chain *n*-alkanes and *n*-alkanoic acids does imply that their sedimentary input is derived from related biologic sources utilizing similar environmental waters.

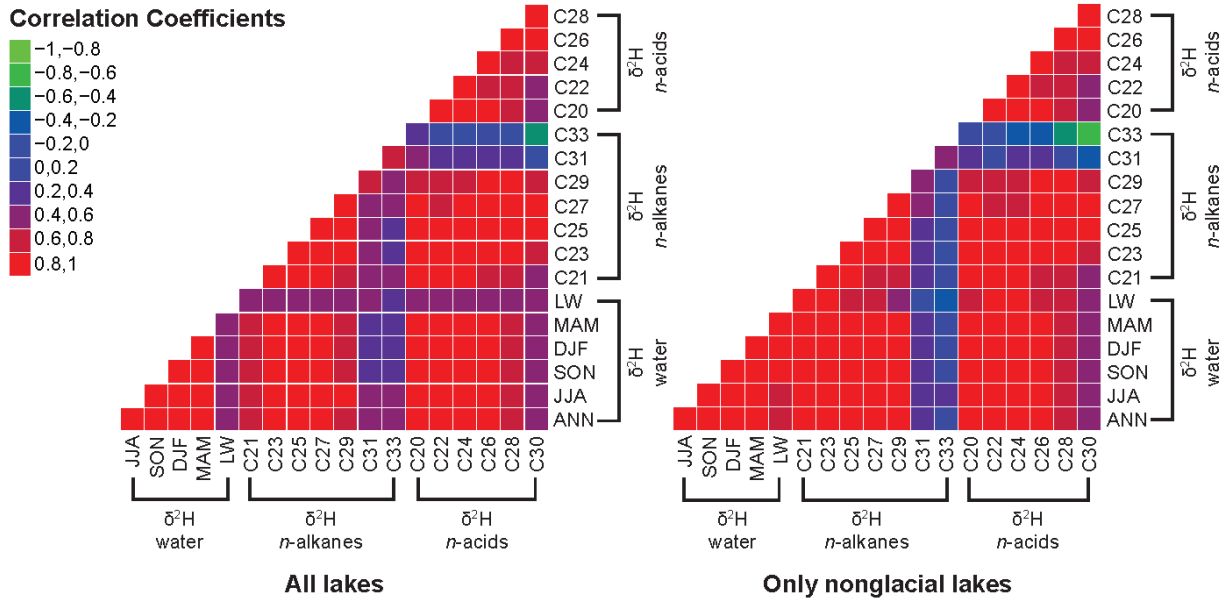

Figure 2.2 *Correlelogram reporting the relationships of δ^2H values of all sedimentary plant waxes (C_{20}-C_{30} n-alkanoic acids, C_{21}-C_{33} n-alkanes) to local waters, calculated using Pearson's pairwise correlation tests for lakes in Greenland transect. Water abbreviations are as follows: Ann=Mean Annual precipitation. Seasonal precipitation values are averages, where JJA= of June, July, August precipitation; SON=September, October, November precipitation; DJF=December, January, February precipitation, MAM=March, April, May Precipitation. LW=Lake Water.*

The δ^2H values of most waxes show a moderate to high correlation (r=0.6-1.0) to the δ^2H values of precipitation. However, when all lakes are included, there is only a moderate to poor correlation (r = 0.4 to 0.6) between the δ^2H values of all compounds and those of lake water. Here, the δ^2H values of lake water are also moderately to poorly correlated to δ^2H values of all meteoric water (r=0.4-0.6). When glacial lakes are removed from the analyses the correlation improves (r=0.7 to 0.9). Glacial lakes are fed directly by the GrIS and are more ^2H-depleted than local mean annual precipitation. Because they are isotopically decoupled from precipitation, glacial lakes provide a test of whether sedimentary mid-chain waxes isotopically reflect lake water when lake water deviates from meteoric water. In glacier-fed lakes we would expect the δ^2H values of mid-chain waxes synthesized in the lake to be more ^2H-depleted compared to those from nonglacial lakes in the same region. Our results instead show that sedimentary waxes in glacial lakes, including mid-chain compounds, isotopically behave like sedimentary waxes in nonglacial lakes from the same region (Figure 2.3).

We suggest two possible reasons for this observation: 1) the turbidity of glacial lakes hinders aquatic primary productivity, and therefore mid- and long-chain waxes are both derived almost exclusively from terrestrial plants in glacier-fed watersheds, or 2) aquatic plants on average are less productive than terrestrial plants in Greenlandic watersheds, contributing a smaller fraction of waxes to the total sedimentary hydrocarbon stock, so that leaf waxes from terrestrial plants dominate sedimentary waxes in both glacial and non-glacial Greenland settings. This latter explanation is supported in part by the proportional abundance of mid-chain compounds in glacial lakes, which are similar to those observed in nonglacial lakes (C_{23} *n*-alkanes contribute 13% to the total wax concentration in glacial lakes and 17% in nonglacial lakes) and by the observation that sedimentary mid-chain waxes in closed (evaporatively-

enriched) lakes seem to also generally relate more strongly to meteoric water than to lake water (although this is a small sample set and p>0.05). In nonglacial lakes, lake water and precipitation are themselves highly correlated so it is difficult to distinguish if the correlation between mid-chain waxes and lake water would otherwise exist in lakes where lake water and precipitation decouple.

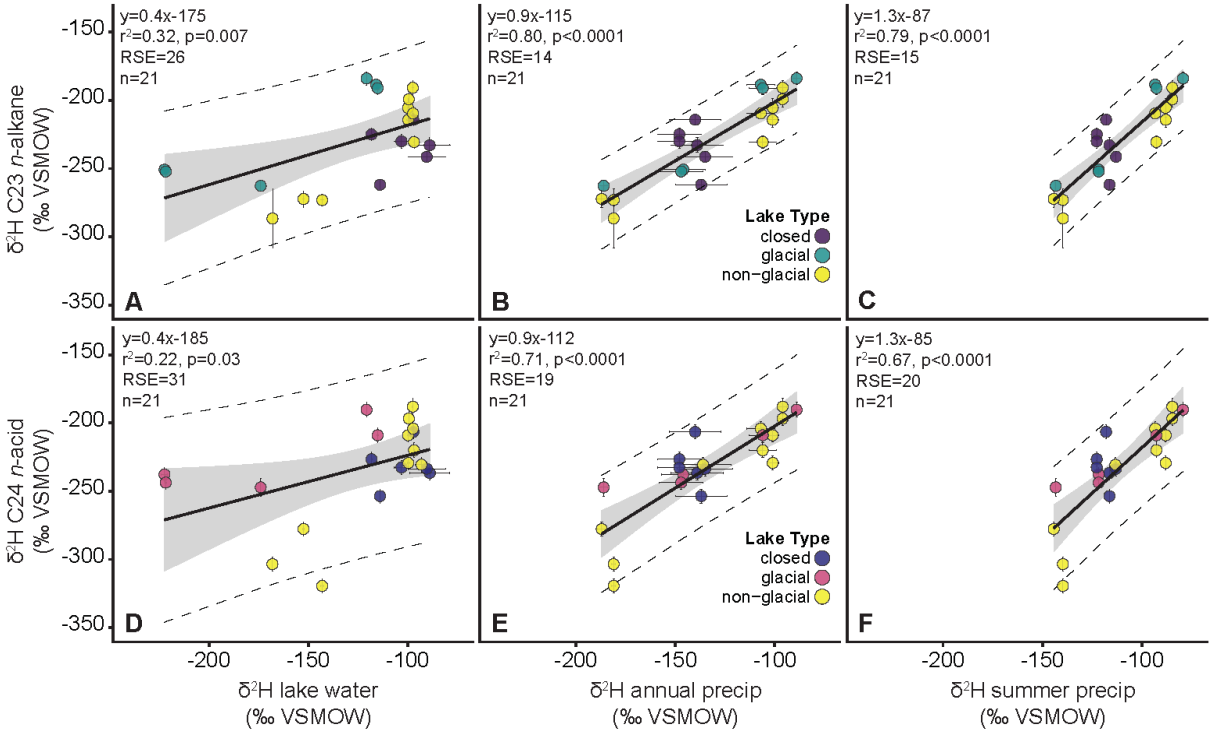

Figure 2.3 *δ^2H values of sedimentary C_{23} n-alkane and C_{24} n-alkanoic acids in Greenland transect plotted against δ^2H values of lake water, δ^2H values of annual precipitation and δ^2H values of summer precipitation. Gray shading represents the 95% confidence interval of slope and intercept of the model, while dashed lines indicate the 95% confidence interval of the prediction values.*

Succinctly, we find that no chain length in the Greenland dataset that unambiguously records hydrogen from lake water when lake water deviates from meteoric water.

An additional surprising observation in this dataset is that there is only moderate to no correlation between the longest-chain waxes (C_{30} *n*-alkanoic acids and C_{31} and C_{33} *n*-alkanes) and environmental waters (r= -0.1 to 0.5) across Greenland. Although C_{31} is a considered the optimal terrestrial plant biomarker elsewhere (Liu et al., 2015), these compounds broadly do not express a strong correlation with environmental waters on Greenland. Given this evidence, and that they are not an abundant component of sedimentary wax profiles for much of the transect, they are excluded from most further analyses and discussion here. This evidence suggests C_{31} *n*-alkanes are poor candidates for proxy-based reconstructions of hydroclimate in parts of Greenland, particularly where the low sedimentary concentrations suggest that they are not an abundant component of local plant waxes, and thus are potentially exogeneous.

Net apparent fractionation of hydrogen isotopes between sedimentary leaf waxes and source waters

Net apparent fractionation (ε_{app}) is a measure of the difference between the δ^2H values of source water (e.g. precipitation or lake water) and the δ^2H values of sedimentary plant waxes, calculated here using the equation

$$\varepsilon = 1000*(\alpha - 1)$$

where $\alpha = R_{wax}/R_{water}$ (Criss, 1999). We find that ε_{app} values in this dataset vary by compound, and are strongly dependent on the seasonality of precipitation selected for use in the calculation.

When all regions are included, the ε_{app} value for C_{29} *n*-alkanes to mean annual precipitation ($\varepsilon_{C29/ANN}$) is ~ -112‰. However, this value is strongly influenced by wax data from Thule lakes, which demonstrate a reduced $\varepsilon_{C29/MAP}$ of ~79‰. If Thule lakes are not included in the average, the $\varepsilon_{C29/MAP}$ is ~120‰, in strong agreement with the global average offset. Standard deviations around the mean ε_{app} value are generally larger for *n*-acids than *n*-alkanes. In all compounds, average ε_{app} for wax to mean annual precipitation is smaller than average ε_{app} for wax to summer precipitation.

Sedimentary wax carbon isotope data

Average $\delta^{13}C$ values of sedimentary waxes range from -30 to -35‰ across all compounds. Leaf waxes are ^{13}C-depleted relative to bulk plant material, so to loosely compare against studies that use bulk plant material, we correct for a wax-bulk plant fractionation of +7‰ (Tipple et al., 2016; Diefendorf and Freimuth, 2017): Calculated Greenland plant bulk $\delta^{13}C$ values range from ~ -23 to -28‰. This range is consistent with the bulk plant $^{13}C/^{12}C$ observed elsewhere in C3 plants (Diefendorf and Freimuth, 2017) and indicates the major supply of plant lipids into Greenland lake sediments is from C3 plants. This observation agrees with botanical observations that modern C3 plants dominate in cooler climates (Woodward et al., 2004) and aligns with observed $\delta^{13}C$ values of plants from arid regions (Kohn, 2010). However, we note no trends in the $\delta^{13}C$ values of sedimentary waxes segregated by region in Greenland, and find no consistent correlation between $\delta^{13}C$ values and air temperature or precipitation amount along the transect. Given the large climatic gradient in our transect this is surprising, but could relate to climatic variables that are poorly constrained in Greenland, including relative humidity and

potential evapotranspiration, or could be related to differences in the plant communities in each region which covers seven, albeit similar, vegetation zones (Jensen and Christensen, 2003).

2.5 Discussion

Greenland long-chain sedimentary waxes

To evaluate the hydrogen isotopic relationship between terrestrial leaf waxes and precipitation, we calculated the ε_{app} values for C_{29} *n*-alkanes and C_{28} *n*-alkanoic acids relative to mean annual (ANN) and summer precipitation. When differentiated by region, Thule, in northwest Greenland and the northern-most field site, demonstrates the smallest $\varepsilon_{C29/ANN}$ (mean = -79‰), with the other three regions of Greenland in near-agreement (mean = -120‰) (Figure 2.4). This could be used to infer anomalous ^{2}H-enrichment of C_{29} *n*-alkanes in Thule compared to the other regions of Greenland represented by this transect. However, a comparison of the $\varepsilon_{C29/summer}$ (i.e. growth-season) instead of annual precipitation at Thule reveals this calibration is in close agreement with the $\varepsilon_{C29/ANN}$ of the other regions of the transect, and with the global average offset (Thule mean $\varepsilon_{C29/summer}$ = -124‰) . The discrepancy between ε_{app} calculated with annual vs. summer precipitation is likely because Thule has both extremely cold winters and (correspondingly) the largest range in the hydrogen isotopic composition of seasonal precipitation of all transect regions, with ~100‰ difference between winter and summer precipitation, and ~40‰ difference between modelled annual and summer precipitation. Calculating ε_{app} using the seasonally-integrated signal of annual precipitation is only appropriate if some winter precipitation is used by Thule plants during synthesis of waxes.

We hypothesize that plants in Greenland, particularly at Thule, utilize strongly summer-biased precipitation as their source water. Thule receives 70% of the annual precipitation budget

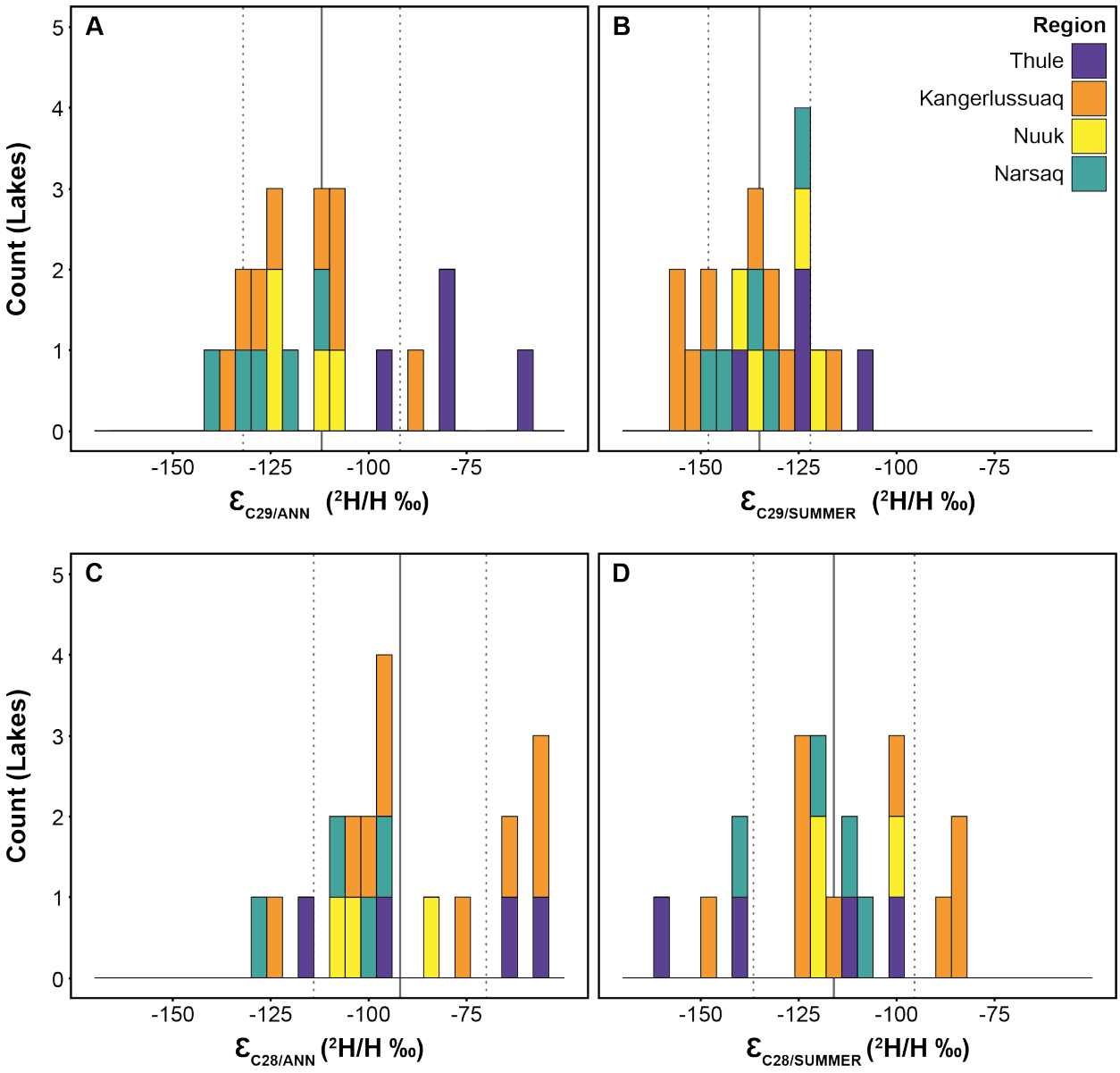

Figure 2.4 *Net apparent fractionation by region of Greenland of sedimentary long-chain C_{29}* n-*alkanes (A and B) and C_{28} n-alkanoic acids (C and D) calculated using the mean hydrogen isotopic composition of annual (left panels) and summer precipitation (right panels). Solid line represents mean ε_{app} and dashed lines demonstrate 1σ around the mean.*

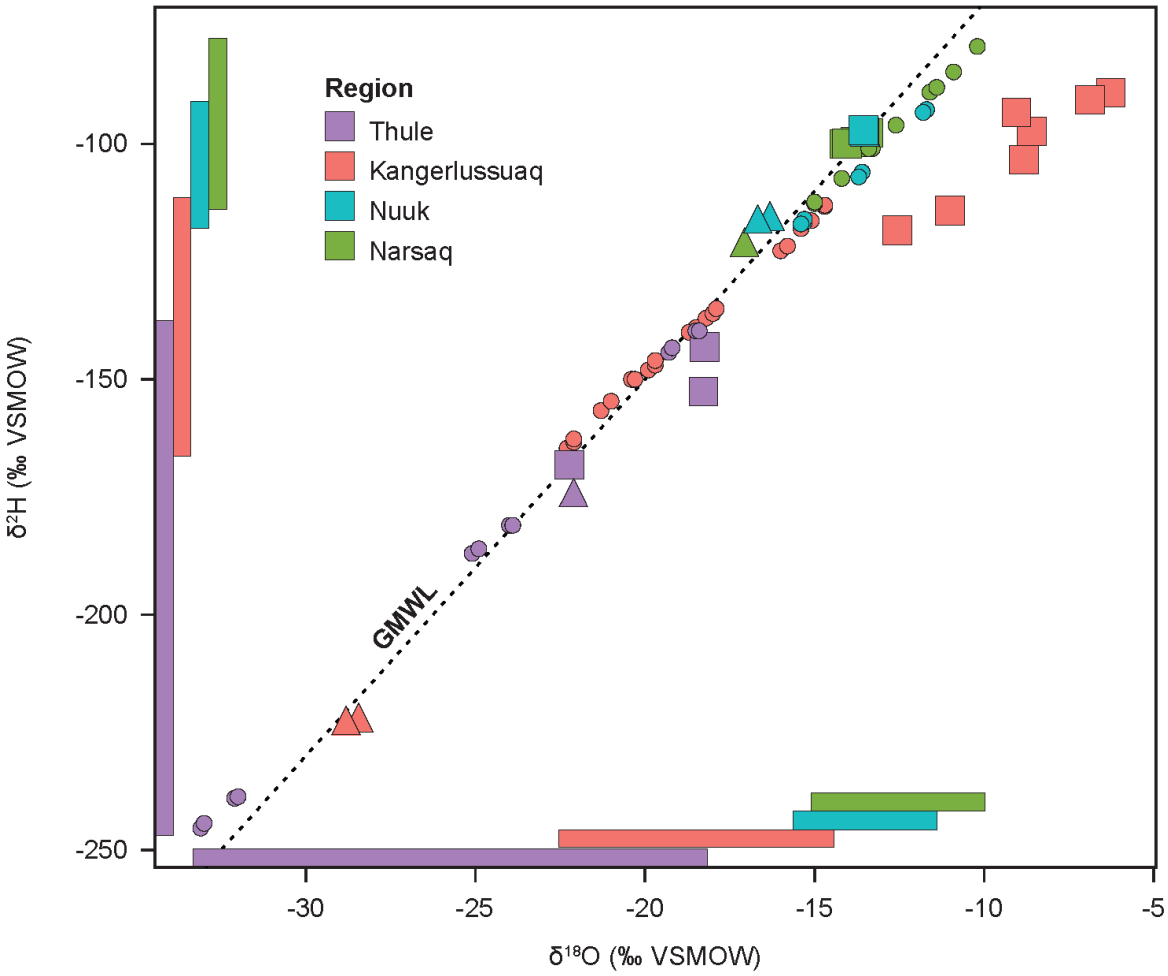

Figure 2.5 Modern water isotopes of transect lakes, including nonglacial (squares) and glacial (triangles) lakes, and of OIPC-modelled precipitation at each lake colored by region (Thule = purple, Kangerlussuaq = pink, Nuuk = blue, Narsaq = green). Colored bars parallel to the x- and y-axes represent the range of average seasonal values across the year in each region. Global meteoric water line (GMWL) defined by Gat (1996).

in the summer, and plants are subject to an extremely short summer growing season, even relative to the other regions in this transect (Cappelen et al., 2001; Jensen and Christensen, 2003). Further, the water isotopes of nonglacial lakes from the Thule region are also strongly

summer-biased, indicating little to no winter precipitation is retained on the landscape into the summer (Figure 2.5). A wax-water calibration utilizing the δ^2H values of mean annual precipitation requires inclusion of ^2H-depleted winter precipitation, which drives a smaller apparent offset by lowering the δ^2H values of source water relative to the δ^2H values of waxes biosynthesized largely with summer precipitation during the growth season.

For the rest of the regions in this transect, it is unclear from this data if terrestrial plants elsewhere strongly utilize summer-biased source water, or if soil water at the time of wax synthesis integrates precipitation from throughout the year. Although much of the precipitation budget across western Greenland is similarly summer-biased (~70% summer at Kangerlussuaq, ~60% summer at Nuuk and Narsarsuaq), the water isotopes of nonglacial, through-flowing lakes in Nuuk and Narsaq appear to agree more strongly with those of annual average precipitation. Nonglacial lakes in Kangerlussuaq presented here are all closed basin and strongly evaporative, but there is some evidence from xylem waters of terrestrial plants in Kangerlussuaq that summer source water δ^2H values are similar to those of annual average or even winter precipitation (Bush et al., 2017).

Offsets of C_{28} *n*-alkanoic acids to precipitation appear to group less by region than *n*-alkanes (Thule mean $\varepsilon_{C29/ANN}$ = -92‰, other three regions mean $\varepsilon_{C28/ANN}$ = -97‰), and variability does not improve when using summer instead of annual precipitation (1σ= 22‰ for $\varepsilon_{C28/ANN}$ and 1σ= 20‰ for $\varepsilon_{C28/summer}$ vs. 1σ= 21‰ for $\varepsilon_{C29/ANN}$ and 1σ= 13‰ for $\varepsilon_{C29/summer}$**)**. Recent work suggests that synthesis of *n*-alkanes in terrestrial leaf waxes occurs predominantly within a few weeks of leaf maturity during the early growth season, whereas *n*-alkanoic acids continue to be produced throughout the growth season (Tipple et al., 2013; Freimuth et al., 2017), although this has not been demonstrated universally. It is possible that a shorter synthesis period for *n*-alkanes

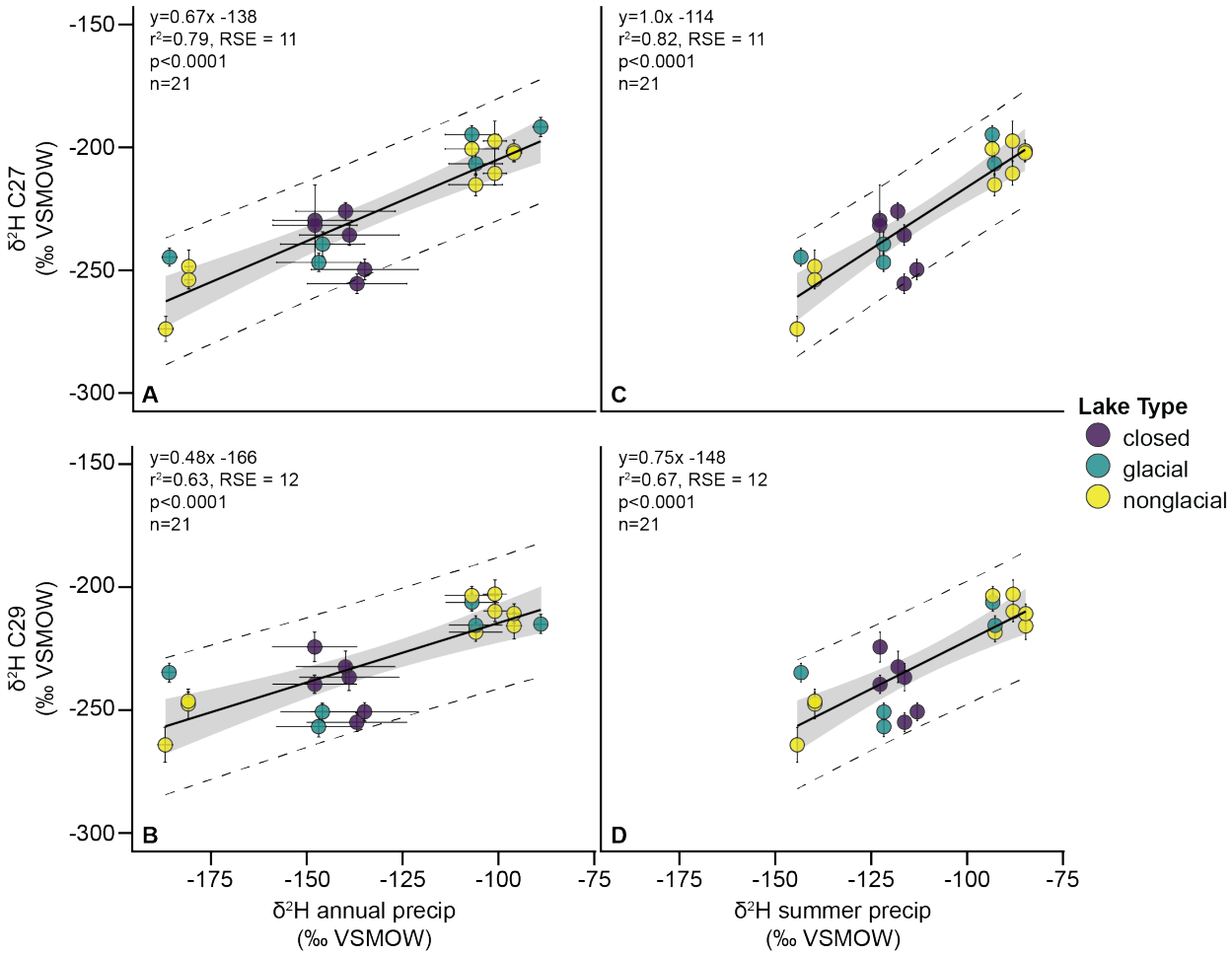

Figure 2.6 *Regression models of δ^2H values of n-alkanes in Greenland lake sediments compared against δ^2H values of annual precipitation for A) C_{27} and B) C_{29} n-alkanes and against δ^2H values of summer precipitation for C) C_{27} and D) C_{29} n-alkanes. Gray shading represents 95% confidence interval of slope and intercept of the model, while dashed lines indicate the 95% confidence interval of the prediction values.*

leads to less variability in ε_{app} because source water and leaf water are more stable over a short period. Additionally, C_{28} *n*-alkanoic acids have also been observed in the tropics to be produced by phytoplankton in the water column (van Bree et al., 2018; Ladd et al., 2018) so some of the

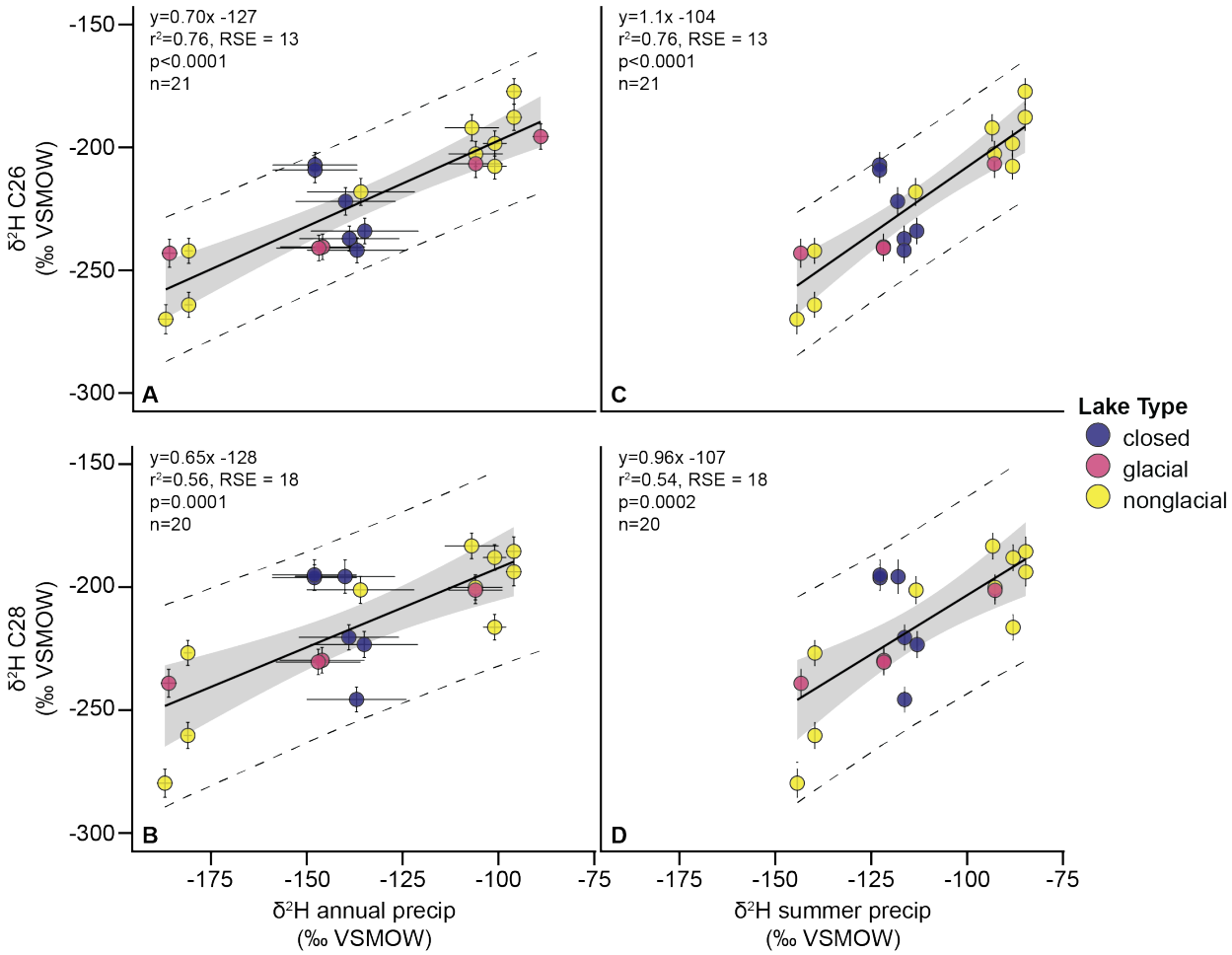

Figure 2.7 *Regression models of δ²H values of n-alkanoic acids in Greenland lake sediments compared against δ²H values of annual precipitation for A) C_{26} and B) C_{28} n-alkanoic acids and against δ²H values of summer precipitation for C) C_{26} and D) C_{28} n-alkanoic acids. Gray shading represents 95% confidence interval of slope and intercept of the model, while dashed lines indicate the 95% confidence interval of the prediction values.*

spread observed in net apparent fractionation values in these compounds could potentially be related to production of C_{28} *n*-alkanoic acids in the water column by phytoplankton, although we have not tested this hypothesis. Additionally, unlike for $\varepsilon_{C29/ANN,}$ there is no existing consensus on global average $\varepsilon_{C28/ANN}$ for us to compare to Greenland data.

The δ^2H values of C_{27} and C_{29} *n*-alkanes demonstrate a strong relationship to δ^2H values of local summer and mean annual precipitation (Figure 2.6). The δ^2H values of C_{28} *n*-alkanoic acids demonstrate a poorer relationship to those of local precipitation (r^2 =0.56 for annual and r^2=0.54 for summer) compared to any relationship between δ^2H values C_{26} *n*-alkanoic acids and C_{27} and C_{29} *n*-alkanes (r^2 =0.63-0.82) (Figure 2.7).

Like $\varepsilon_{C28/precip}$, this could be related to a broader temporal synthesis window for *n*-alkanoic acids than for *n*-alkanes in plants (Freimuth et al., 2017), and/or water-column production and/or degradation of these compounds (van Bree et al., 2018; Ladd et al., 2018). We find that the correlation of δ^2H values of C_{28} *n*-alkanoic acids is strongest to the average δ^2H value of winter precipitation (r=0.77, p <0.0001; December, January, February vs. for summer precipitation, r =0.74, p=0.0002), which is not the case for C_{26} *n*-alkanoic acids, C_{27} *n*-alkanes, or C_{29} *n*-alkanes, which all show the strongest correlation is to summer and/or annual precipitation. Given that seasonal precipitation values are themselves highly correlated, correlation coefficients here provide little insight into the seasonality of precipitation used during wax synthesis. However, it is worth noting that the relationship between the long-chain waxes discussed above (those in Figures 2.6 and 2.7) and summer precipitation demonstrate nearly a 1:1 relationship, and yield much shallower slopes when compared to annual precipitation, suggesting a better fit to summer precipitation.

Glacial lake sediments have low organic content and are fed directly by melt from the Greenland Ice Sheet, and as such are ostensibly poor candidates for sedimentary wax proxy reconstructions of δ^2H values of precipitation. However, we find that δ^2H values of *n*-alkanes and *n*-alkanoic acids in glacial lakes in this dataset match those of neighboring nonglacial lakes in each region of Greenland, and similarly reflect the δ^2H values of local precipitation. This

finding supports that glacial lakes can also be appropriate settings for utilizing wax biomarker proxies to reconstruct precipitation isotopes, providing opportunity for reconstruction of δ^2H values of precipitation in Arctic regions where there are few or no nonglacial lakes available.

Greenland mid-chain sedimentary waxes

Lake water δ^2H values reported here are from measurement of water collected at each location during the summer season, often only once. These values represent a snapshot in summer lake water, and thus may be a poor representation of the annually-integrated value of lake water in lakes with short residence periods (<1 year); however, these values provide an approximation of lake water during the summer ice-free period when aquatic plant growth occurs, and the isotopic composition of nonglacial lakes in this transect are correlated to meteoric water. While some aquatic plants have been observed to live perennially in cold climates (Aichner et al., 2017), in this Arctic environment with little to no daylight during the coldest months, growth of aquatic plants, and therefore lipid production, is likely stimulated by light availability and warmer temperatures during the ice-free summer season (Sand-Jensen et al., 1999; Hawes et al., 2002). Because of this, lipids in aquatic plants from Greenland should isotopically relate to lake water during the summer. However, as our correlation tests demonstrate, there is no unambiguous relationship between the δ^2H values of any plant wax and those of lake water. Linear models further demonstrate that the δ^2H values of mid-chain waxes have a significant relationship to those of annual and summer precipitation, but not to lake water.

The current precedent for source-attribution by chain-length is largely derived from observations of chain-length relative abundances in aquatic vs. terrestrial plants (K.J. Ficken et al., 2000; Gao et al., 2011; Duan and Xu, 2012; Garcin et al., 2012).While aquatic plants produce more mid-chain than long-chain waxes in proportional abundance (and broadly vice versa for

terrestrial plants), the overall lipid production by aquatic plants is often dwarfed by that of terrestrial vegetation (Diefendorf and Freimuth, 2017). In sediments, mid-chain waxes are therefore likely from a mix of both aquatic plant lipids and terrestrial leaf waxes and probably often weights toward terrestrial plants. The use of sedimentary mid-chain waxes to represent aquatic plants, and thus lake water, in downcore reconstructions requires that the absolute input of mid-chain wax to sediments is dominantly from aquatic plants. The weighting of aquatic-terrestrial plant input to mid-chain *n*-alkanes in sediments will differ by watershed depending on the relative abundances of aquatic vs. terrestrial plants; mid-chain wax in lake sediments will reliably record lake water only in watersheds with minimal terrestrial input of waxes and abundant aquatic plants. To deal with this problem in downcore reconstruction, a broad determination of the main source of waxes can be made using sedimentary concentration, as previously advocated elsewhere (K.J. Ficken et al., 2000; Nichols et al., 2006; Zhang et al., 2017). Here, we suggest for Greenland the utilization of C_{23}:C_{29} ratios for *n*-alkanes as an indicator of aquatic plant contribution, given that C_{31} appears in only low concentrations across much of Greenland, and C_{25} and C_{27} are produced abundantly by terrestrial plants in Greenland (Berke et al., 2019).

Overall, these findings challenge the use of δ^2H values of mid-chain waxes for the reconstruction of δ^2H values of lake water in some lakes. This is also a point of concern for interpreting long-chain waxes in sediments as universally-derived from terrestrial leaf waxes. For example, in sediments where absolute quantities of C_{23}>>C_{29}, it is possible that the long-chain *n*-alkanes could also be derived dominantly from aquatic plants. We therefore again advocate quantification of leaf waxes in tandem with isotope measurements to assess the proportion of mid- to long-chain waxes (i.e. C_{23}:C_{29} ratios) in sedimentary archives as a qualitative measure of wax source. This is necessary even in watersheds in which the modern relative input is known

because plant communities shift with changing climate (particularly in the Arctic) changing the balance between terrestrial and aquatic plant contributions of mid-chain waxes to sediments over time.

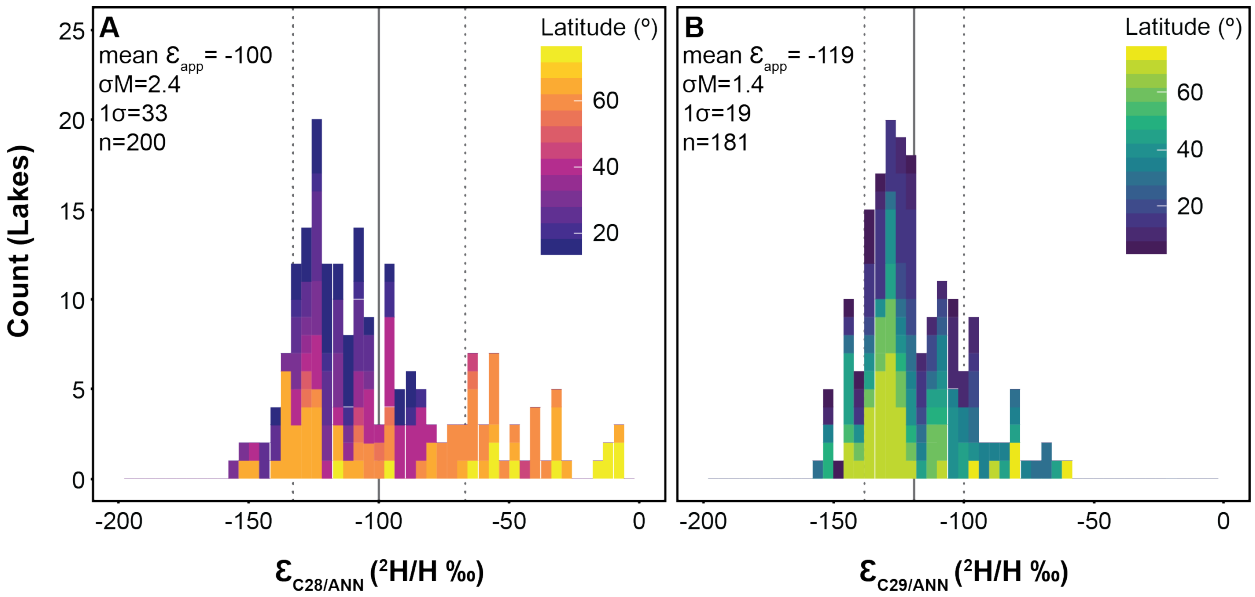

Figure 2.8 *Net apparent fraction values (ε_{app}) of compiled global data, including the Greenlandic dataset presented here, for A) C_{28} n-alkanoic acids and B) C_{29} n-alkanes calculated using δ^2H values of annual precipitation. Color corresponds with latitude. Standard error of the mean (σM) =1$\sigma/\sqrt{(n)}$, 1σ =standard deviation around the mean, and n =sample size*

Greenland and other high latitude data in a global context

Despite the complexity of factors that impact plants and precipitation across the globe, an existing synthesis of sedimentary C_{29} *n*-alkanes from mid- and low-latitudes demonstrates a strong relationship between the δ^2H values of sedimentary C_{29} *n*-alkanes and those of annual precipitation (Sachse et al., 2012), with the prevailing global average $\varepsilon_{C29/ANN}$ value of -121‰

(1σ ±17.5‰, n=59; Sachse et al., 2012). This value is identical to the observed value of $\varepsilon_{C29/ANN}$ of -121‰ (1σ ± 30‰, n=316) in the same study's compilation of C_{29} *n*-alkanes from leaf samples of living plants (Sachse et al., 2012). In an effort to evaluate the wax-water relationship in Greenland relative to middle and low latitudes, we updated the global framework first compiled by Sachse et al. (2012) to include all lacustrine sedimentary leaf wax H isotope data published to date. C_{29} *n*-alkanes and C_{28} *n*-alkanoic acids are the most consistently-reported sedimentary waxes in the published literature so we focus our discussion on these compounds.

Our updated synthesis of *n*-alkanes adds 122 new sites (21 from our Greenland study) to the original set of 59 sites, and includes lakes spanning a 74° latitudinal range (Sachse et al., 2004; Mügler et al., 2008; Xia et al., 2008; Polissar et al., 2009; Aichner et al., 2010; Duan et al., 2011; Douglas et al., 2012; Garcin et al., 2012; Guenther et al., 2013; Leider et al., 2013; Daniels et al., 2017; Nelson et al., 2018). In this compilation, we find a global average $\varepsilon_{C29/ANN}$ value of -119‰ (1σ ±19.0‰, n=181) (Figure 2.8). This value, remarkably, is statistically indistinguishable from the global average offset previously observed by Sachse et al. (2012) of -121‰ (1σ ±17.5‰, n=59) despite our addition of data from lakes in high-latitude and high-elevation locations. This demonstrates that the average net apparent offset in δ^2H values of sedimentary C_{29} *n*-alkanes from annual precipitation is robust globally, across diverse climates, and that high latitude sites are consistent with the original relationship assessed from middle and low latitude sites (Figure 2.9).

For sedimentary C_{28} *n*-alkanoic acids, we compile data from 200 lakes spanning 63° of latitude, including this study (Huang et al., 2004; Sachse et al., 2004; Hou et al., 2007; Douglas et al., 2012; Shanahan et al., 2013; Daniels et al., 2017; Ladd et al., 2018). We find a global mean $\varepsilon_{C28/ann}$ value of -100‰ (1σ ± 33.0‰, n=200). The linear model for δ^2H values of C_{28} *n*-

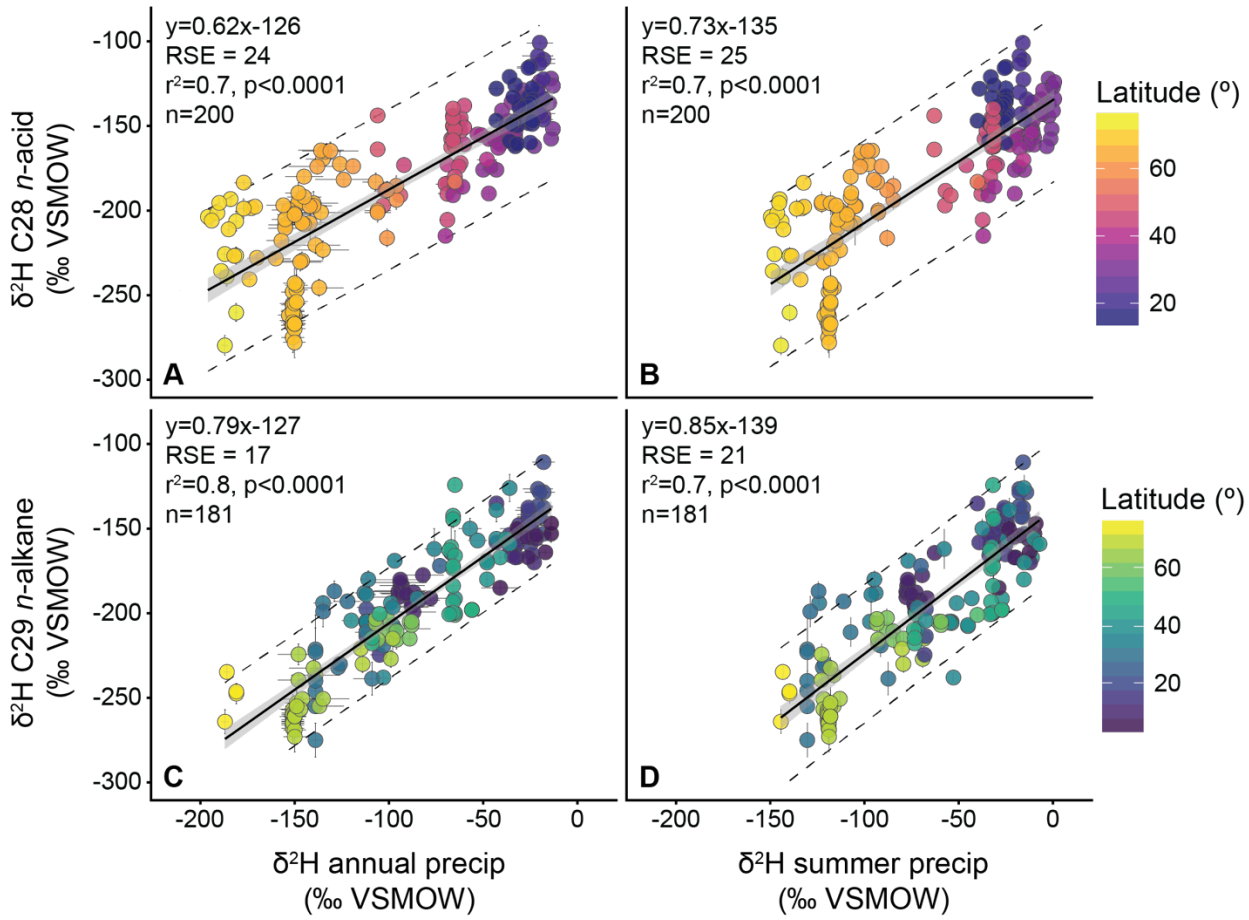

Figure 2.9 *Regression models of global sedimentary δ^2H-values for sedimentary C_{28} n-alkanoic acids and C_{29} n-alkanes data compared against δ^2H-values of annual and summer precipitation estimated via the OIPC (Bowen et al, 2018. Latitude is an absolute value, although nearly all data points in the synthesis are derived from sites in the northern hemisphere (n=178 for n-alkanes, n=200 for n-alkanoic acids). Color corresponds with latitude of lake for each data point. RSE= residual standard error, n =sample size.*

alkanoic acids compared against annual precipitation shows greater residual standard error than does the linear model for δ^2H values of C_{29} *n*-alkanes compared against annual precipitation (RSE_{C28} =24‰ vs. RSE_{C29} =17‰), as well as a lower r^2 value (r^2_{C28}=0.7 vs. r^2_{C29}=0.8). This

demonstrates that on a global scale, δ^2H values of modern sedimentary C_{29} *n*-alkanes more closely track those of precipitation than do the δ^2H values of C_{28} *n*-alkanoic acids, albeit both compounds demonstrate a robust relationship to precipitation.

Much less work has been done to demonstrate the relationship between the δ^2H values of aquatic plant lipids and those of lake waters on broad spatial scales. Widespread testing of how δ^2H values of sedimentary mid-chain waxes relates to δ^2H values of lake water (or precipitation) is largely lacking, and our data indicate a poor relationship between waxes and lake water at least in Greenland. To further explore this relationship, we also evaluate these compounds in our updated compilation: We find that mid-chain waxes are equally related to both precipitation and lake water (Figure 2.10), which are themselves highly correlated.

These data therefore preclude unambiguous assessment of the utility of these compounds as proxies for the hydrogen isotopic composition of lake water. However, the sample size in these assessments is much lower than that of C_{28} *n*-alkanoic acids and C_{29} *n*-alkanes due to an overall reporting bias towards longer chain-lengths in the literature. Additionally, lake water isotope values are often not reported so there are significantly fewer data points in the global comparison of δ^2H values of wax-lake water than the comparison of δ^2H values of wax-precipitation for all chain-lengths.

Proxy Approach: Net apparent offset correction vs. the global regression line

We demonstrate here that there is a strong linear relationship between the δ^2H values of precipitation and those of sedimentary plant waxes globally, including in the high latitudes. This provides two approaches to reconstruct δ^2H values of precipitation from the δ^2H values of sedimentary wax: 1) using one of the linear regressions defined by either local or global modern

calibrations, and 2) applying a correction for apparent fractionation. The advantage to using a regression is that the slope of the line will inherently account for some of the variability in the biosynthetic fractionation effect created by changing vegetation and/or environmental conditions

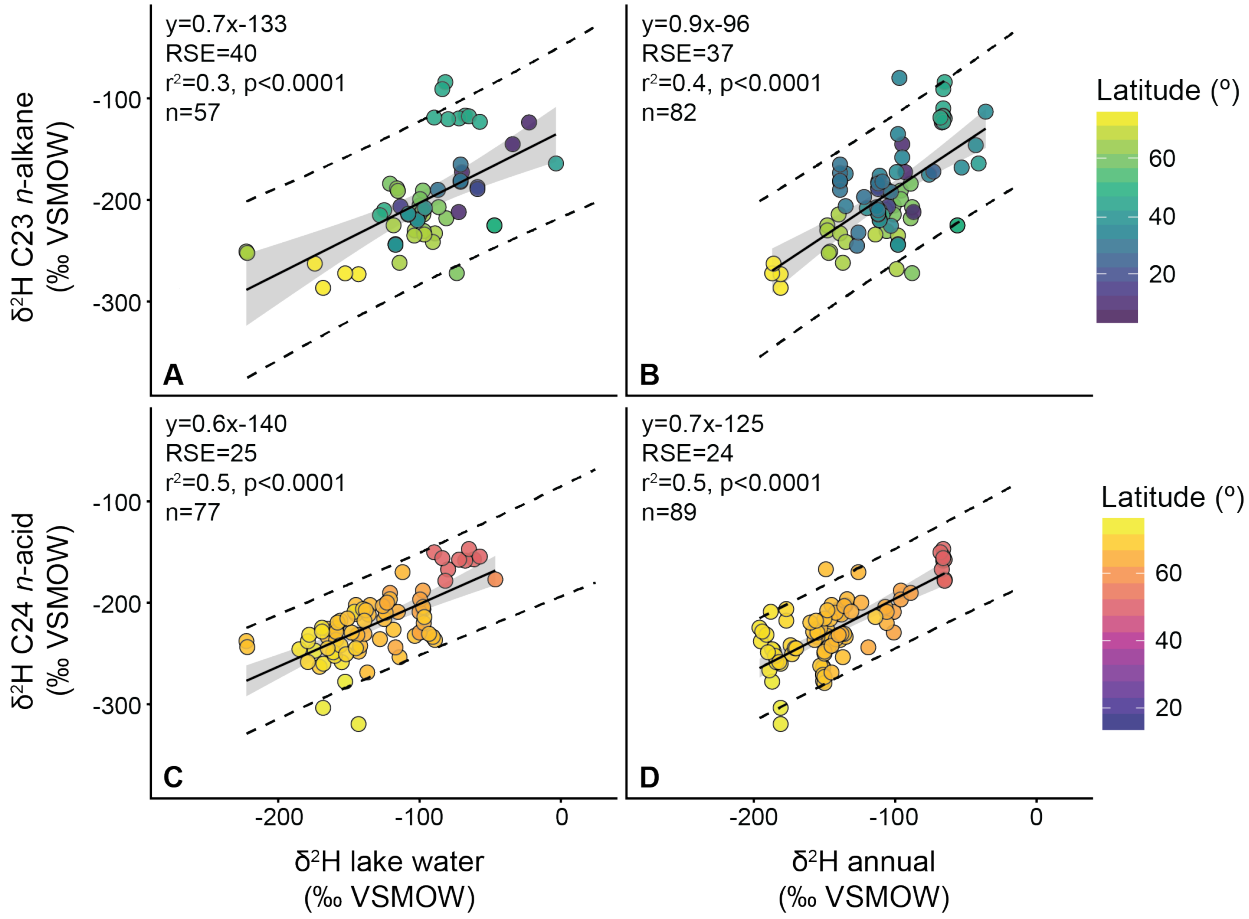

Figure 2.10 *Regression models of global sedimentary δ^2H-values for sedimentary C_{24} n-alkanoic acids and C_{23} n-alkanes data compared against δ^2H-values of lake water and annual precipitation estimated via the OIPC (Bowen et al, 2018). RSE= residual standard error, n =sample size.*

(e.g. aridity) along natural gradients. However, to use a regression requires assuming the underlying source water as either mean annual or seasonal precipitation. On the other hand, using

the global apparent fractionation value to correct for biosynthetic fractionation is a more direct way to account for the process of fractionating leaf water and organic H during the biosynthesis of wax, but ignores important differences in the fractionation factor with vegetation and/or environment type by averaging all regions together.

2.6 Conclusions

We find that the δ^2H values of sedimentary *n*-alkanes and *n*-alkanoic acids across Greenland demonstrate a strong correlation to δ^2H values of local precipitation. Data from Thule, the northern-most region of our transect, reveal that the seasonality of the δ^2H values of water used in this proxy calibration is a particularly important consideration where the growing season for plants is restricted to the summer months. Some past observations of lesser fractionation in Arctic plants could possibly be explained by calibration of net apparent fractionation to annual precipitation instead of summer precipitation. Sedimentary C_{27} and C_{29} *n*-alkanes provide the best proxy for local precipitation isotopes in Greenland, with C_{26} and C_{28} *n*-alkanoic acids a viable but noisier alternative. In our dataset, no chain length has a strong correlation with lake water independent of precipitation (i.e. in lakes where lake water is demonstrably different from precipitation), possibly due to substantial input of mid-chain waxes to sediments from terrestrial plants. Therefore, interpretation of the δ^2H values of mid-chain sedimentary compounds as those of paleo lake water should only be attempted if there is evidence to support substantial input of waxes from aquatic plants. The largest compounds we observed in Greenland sediments, C_{31} and C_{33} *n*-alkanes and C_{30} *n*-alkanoic acids, are in low concentration across much of the transect, and their δ^2H values are poorly correlated to those of local precipitation. This makes them poor candidates for reconstructions of precipitation isotopes in much of Greenland, and potentially

other high-latitude regions. Our updated global syntheses of C_{29} sedimentary *n*-alkane and C_{28} *n*-alkanoic acid δ^2H values demonstrate that these compounds are a robust paleohydrologic proxy, and that data from Greenland is consistent with global data. Finally, compound-specific carbon isotopes do not show strong correlations to water availability and temperature in Greenlandic data, although overall, Greenland carbon isotope data maps well with other similarly arid regions. More extensive environmental data (i.e. relative humidity, potential evapotranspiration) is needed to further investigate controls on carbon isotopes in Greenland. In sum, we find that the δ^2H values of sedimentary C_{29} *n*-alkanes are the best proxy for δ^2H values of precipitation globally, where understanding how precipitation changes in response to large climate shifts is important for confidently predicting future change.

2.7 Acknowledgements

Collaborators on this work include Yarrow Axford, Magdalena Osburn, and Andy Masterson. Additional recognition for assistance is given to Hannah Dion-Kirschner, Jordan Todes, Sohyun Lee, and Grace Schellinger for assistance in the laboratory; Andrew Jacobsen, Grace Andrews, Johnny Ryan, Aaron Hartz, Gaylen Sinclair, Saedis Olafsdottir, Everett Lasher, and Alex Taylor for assistance with fieldwork; Polar Field Services, Inc., Air Greenland, the US Air Force and the US Air National Guard for logistical support. This work was supported by the NSF Polar Programs Award #1454734 and 1108306 to YA, NSF GRF to JM, NSF Geography and Spatial Sciences DDRI Award #1634118 to YA, JM, MO; National Geographic Society to YA; ISEN to YA, MO; and a Geological Society of America graduate student research grant to JM. Yongsong Huang, Timothy Shanahan, William Daniels, Dirk Sachse and Nemiah Ladd provided direct access to lipid and environmental waters hydrogen isotope datasets from

previously published works. The map of Greenland was generated using GMT. Two anonymous reviewers provided thoughtful comments on this manuscript.

Chapter 3

Pronounced summer warming in northwest Greenland during the Holocene and Last Interglacial

This chapter has been published. Please cite:

McFarlin, J.M., Axford, Y., Osburn, M.R., Kelly, M.A., Osterberg, E.C., Farnsworth, L.B. (2018) Pronounced summer warming in northwest Greenland during the Holocene and Last Interglacial. ***Proc. Natl. Acad. Sci.*** **115**, 6357-6362.

3.1 Abstract

Projections of future rates of mass loss from the Greenland Ice Sheet are highly uncertain because its sensitivity to warming is unclear. Geologic reconstructions of Quaternary interglacials can illustrate how the ice sheet responded during past warm periods, providing insights into ice sheet behavior and important tests for data-model comparisons. However, paleoclimate records from Greenland are limited: Early Holocene peak warmth has been quantified at only a few sites, and terrestrial sedimentary records of prior interglacials are exceptionally rare due to glacial erosion during the last glacial period. In this chapter, I discuss findings from the first reported lacustrine archive that records both the Holocene and the Last Interglacial (LIG) from Greenland, allowing for direct comparison between two interglacials. Sedimentary chironomid assemblages indicate peak July temperatures 4.0-7.0°C warmer than modern during the early Holocene maximum in summer insolation. *Chaoborus* and chironomids in LIG sediments indicate July temperatures at least 5.5-8.5°C warmer than modern. These estimates indicate pronounced warming in northwest Greenland during both interglacials. This helps explain dramatic ice sheet thinning at Camp Century in northwest Greenland during the

early Holocene, and for the LIG aligns with controversial estimates of Eemian warming from ice core data retrieved in northern Greenland. Converging geologic evidence for strong LIG warming is challenging to reconcile with inferred Greenland Ice Sheet extent during the LIG, and the two appear incompatible in many models of ice sheet evolution. An increase in LIG snowfall could help resolve this problem, pointing to the need for hydroclimate reconstructions from the region.

3.2 Introduction

Mean global surface temperature is projected to warm 1-4°C by 2100, with amplification of surface temperatures in the Arctic 2-4 times that of the global mean (Miller et al., 2010; Collins et al., 2013). In response, mass loss from the Greenland Ice Sheet (GrIS) is expected to increase, contributing up to ~0.2 m of global sea level rise by the end of this century (Collins et al., 2013). Estimates of sea level rise come largely from computational models. These models are tested with paleoclimate data-model comparisons, which depend upon reliable constraints on past climatic conditions. The insolation-driven warming of the Arctic in the early Holocene (~11-8 ka) and the Last Interglacial Period (LIG; 129-116 ka) are key targets for data-model comparisons, providing important checks of the models used to project long-term warming and future ice sheet evolution (Marcott et al., 2013). Notably, many model studies for these periods find that simulations invoking temperatures comparable to those implied by the few existing paleotemperature reconstructions from Greenland drive GrIS behavior that conflicts with inferred ice sheet extent (Simpson et al., 2009; Stone et al., 2013; Lecavalier et al., 2014; Goelzer et al., 2016). This highlights a need for additional paleoclimate records from Greenland that better resolve regional and seasonal conditions to provide stronger tests of climate and ice sheet models.

In Greenland, there are few quantitative air temperature reconstructions near the ice sheet margin for the early Holocene and the LIG (Table 3.1; including records from nearby Baffin and Ellesmere Islands). A lack of constraint on these conditions is a significant limitation in understanding past ice sheet behavior because summer temperatures along the ice sheet margins drive surface melt and thus exert a major control on mass balance of the dominantly land-based interglacial ice sheet (Goelzer et al., 2016; Buizert et al., 2018). Lakes on Greenland's ice-free margin provide opportunities to reconstruct paleoclimate via sedimentary climate proxies. While there are several Holocene climate reconstructions from Greenland lake sediments for the middle to late Holocene (Briner et al., 2016), to date only one published lacustrine archive quantifying summer air temperature extends well into the early Holocene (Axford et al., 2017) to overlap with maximum summer insolation and peak overall regional Holocene warmth inferred from ice cores (Vinther et al., 2009; Lecavalier et al., 2017). The conventional picture of Greenland's climate during the Holocene Thermal Maximum (HTM) is of ~3°C of roughly homogenous warming (Vinther et al., 2009), and this typifies the maximum forcing applied (+2-4°C vs. modern) across Greenland in simulations of Holocene ice sheet evolution (Simpson et al., 2009; Lecavalier et al., 2014). However, a recent reinterpretation of ice $\delta^{18}O$ data from Agassiz Ice Cap, the original results of which were influential in shaping perceptions of HTM climate over Greenland, revises peak Holocene precipitation-weighted temperatures at Agassiz upwards from the original reconstruction by ~3°C (Lecavalier et al., 2017). New evidence corroborating this surprising result would indicate large spatial variations in the magnitude of HTM warmth, including along the margins of the GrIS. As proposed by LeCavalier et al. (2017), warmer regional temperatures during the HTM could help explain otherwise puzzling ice sheet thinning at Camp Century in northwest Greenland (Vinther et al., 2009; Lecavalier et al., 2017). Updated estimates of stronger warming over the northern GrIS, extrapolated from Agassiz, increased the

Table 3.1 Greenland/Baffin Bay region continental air temperature estimates

Site	Map	Proxy	Baseline	Season	Anomaly (°C)	Ref.
(a) early Holocene						
Wax Lips Lake	**WLL**	**midges**	**1952-2012 AD**	**July**	**+5.5±1.5**	**This study**
Agassiz Ice Cap	A	melt	1750 AD	summer	+5, min. of	Lecavalier et al., 2017
		ice $\delta^{18}O$	1750 AD	P-W	+6.1±2.2	Lecavalier et al., 2017
Last Chance Lake	1	midges	last millennium	July	+3-4±1.5	Axford et al., 2017
Renland Ice Cap	R	ice $\delta^{18}O$	2000 AD	P-W	+2-3	Vinther et al., 2009
Lake CF8	2	midges	1961-1990 AD	July	+4-5±2.2	Axford et al., 2011
Lake CF3	3	midges	1951-1980 AD	July	+4-6±2.2	(Briner et al., 2006)
(b) Last Interglacial						
Wax Lips Lake	**WLL**	**midges**	**1952-2012 AD**	**July**	**+7.0±1.5**	**This study**
Thule*	T	insects, plants	1990s AD	summer	+4	Bennike and Böcher, 1992
NEEM Ice Cores	Nm	ice $\delta^{18}O$	last millennium	P-W	+8±4	Dahl-Jensen et al., 2013
		air $\delta^{15}N$	preindustrial	MAAT	+7-11	Landais et al., 2016
Jamesonland*	J	insects, plants	1990s AD	summer	+5	Bennike and Böcher, 1994
GISP2 Ice Cores	G	ice $\delta^{18}O$	last millennium	P-W	+4-8	Yau et al., 2016
Lake CF8	2	midges	1961-1990 AD	July	+4-5±2.2	Axford et al., 2011
Fog Lake	4	pollen	1971-2000 AD	July	+4-5±1.2	(Fréchette et al., 2006)
		midges	1971-2000 AD	July	+3-4±1.5	Francis et al., 2006
Bro. Fog Lake	5	pollen	1971-2000 AD	July	+3-4±1.2	Fréchette et al., 2006
		midges	1971-2000 AD	July	+8-9±1.5	Francis et al., 2006
Amorak Lake	6	pollen	1971-2000 AD	July	+4-5±1.2	Fréchette et al., 2006

*Estimates derived from individual published sites for (a) Average maximum air temperature anomaly for the early Holocene from 11-8 ka or any recorded portion of that period. Archives that begin after 8 ka or are not securely dated to within this time are excluded. (b) Maximum air temperatures recorded in archives of the Last Interglacial. Note that: estimates vary in timing within the LIG, in most cases precise timing within the LIG is unknown, and for most archives it is uncertain if maximum local LIG temperatures are recorded. *nearshore marine sediments, P-W=precipitation-weighted annual air temperature, MAAT=mean annual air temperature.*

GrIS modeled contribution to sea level rise during the last deglaciation by 1.4 m sea-level equivalent (Lecavalier et al., 2017). These findings demonstrate that uncertainties in the magnitude of HTM warming significantly influence the simulations of ice sheet evolution for this period, and underscore how sensitive the GrIS is to temperature.

Lake sediments were extensively eroded by expanded ice sheets during the last glacial period, so most LIG records from Greenland come from the GrIS itself and do not constrain the ice-marginal summer temperatures important to surface melt. There are two locations along Greenland's margin for which estimates of summer air temperature anomalies during some part of the LIG are available (+4-5°C vs. present) (Bennike and Böcher, 1992; Bennike and Böcher, 1994). Furthermore, only the North Greenland Eemian Ice Drilling (NEEM) record definitively captures maximum LIG warmth. The peak precipitation-weighted temperature anomaly from ice $\delta^{18}O$ reconstructed at NEEM for the LIG is +8±4°C relative to the last millennium (Dahl-Jensen et al., 1998). This strong inferred LIG warming has generally been perceived as a controversial outlier because syntheses of terrestrial climate reconstructions have reported average LIG warming across the Arctic and Greenland of ≤5°C (CAPE-Last Interglacial Project Members, 2006; Turney and Jones, 2010), and most climate models simulate a temperature anomaly in north Greenland that is ≤5°C (Lunt et al., 2013; Bakker et al., 2014; Capron et al., 2014). Ice $\delta^{18}O$-temperature relationships vary geographically and change through time (Sime et al., 2013), and are impacted by changes in elevation and ice sheet topography (Merz et al., 2014; Sjolte et al., 2014). In modern ice at the NEEM site, an ice $\delta^{18}O$-temperature relationship of 1.1‰ $°C^{-1}$ was observed during recent warming (Masson-Delmotte et al., 2015); however, temperature anomalies for the LIG in the NEEM ice cores were calculated using a relationship from central Greenland of 0.5 ‰ $°C^{-1}$ (Vinther et al., 2009; Dahl-Jensen et al., 2013), perhaps resulting in an overestimation of LIG temperature at NEEM (Sime et al., 2013; Sjolte et al., 2014). However, a

subsequent LIG temperature reconstruction based on nitrogen isotopes ($\delta^{15}N$) measured in trapped air in NEEM ice cores, which estimates warming of 7-11°C vs. preindustrial, supports the estimate from ice $\delta^{18}O$ (Landais et al., 2016). A recent reanalysis of LIG ice at the Greenland Ice Sheet Project 2 (GISP2) site shows 4-8°C of warming vs. the last millennium, further supporting warmer conditions during the LIG than previously inferred (Yau et al., 2016).

In contrast to ice core evidence for a LIG peak warming anomaly of 4-12°C over the GrIS, geologic evidence indicates that GrIS area and thickness were only somewhat reduced relative to today. Total air content in NEEM and GISP2 ice suggests LIG elevation of the GrIS at both localities was within several hundred meters of modern (Dahl-Jensen et al., 2013; Yau et al., 2016). LIG-aged ice has been identified from deep core sites across Greenland (NEEM, NGRIP, GRIP, GISP2, DYE3 and Camp Century; Figure 3.1B) (NGRIP Project Members, 2004; Masson-Delmotte et al., 2013). Along with sedimentologic evidence from the Eirik Drift for some enduring southern ice throughout the LIG (Colville et al., 2011), the ice core evidence indicates that much of the GrIS persisted through the LIG despite possible large losses of ice from some regions (Masson-Delmotte et al., 2013). This geologic picture of ice loss contributes to converging model estimates that the GrIS supplied 1-3 m of the 6-9 m of observed LIG sea-level rise, and implies high sensitivity of the West Antarctic ice sheet to LIG warming (Dutton et al., 2015). However, a major limitation to this conclusion is that LIG temperature estimates from Greenland are sparse and highly uncertain, and therefore have been open to a wide range of interpretations. This is particularly the case for summer temperatures around ice margins and the seasonality of precipitation-weighted warming estimated from $\delta^{18}O$. For ice sheet models to sustain the requisite volume of ice on Greenland during the LIG they must be forced by temperature anomalies <5°C or even <2°C, much cooler than temperatures inferred at NEEM and recently at GISP2 (Capron et al., 2014; Goelzer et al., 2016; Yau et al., 2016). Thus, the ice

sheet models call the geologic data for temperature and GrIS extent into question, and vice versa. Resolving these issues for both the Holocene and the LIG requires more confident reconstructions across Greenland of air temperatures, precipitation amounts, and ice extent. Here we report estimates of Holocene and LIG July air temperatures near the ice sheet margin in northwest Greenland, derived from the novel discovery of Holocene and LIG lake sediments preserved *in situ* in the extant lake we informally designate Wax Lips Lake (76.85°N, 66.96°W).

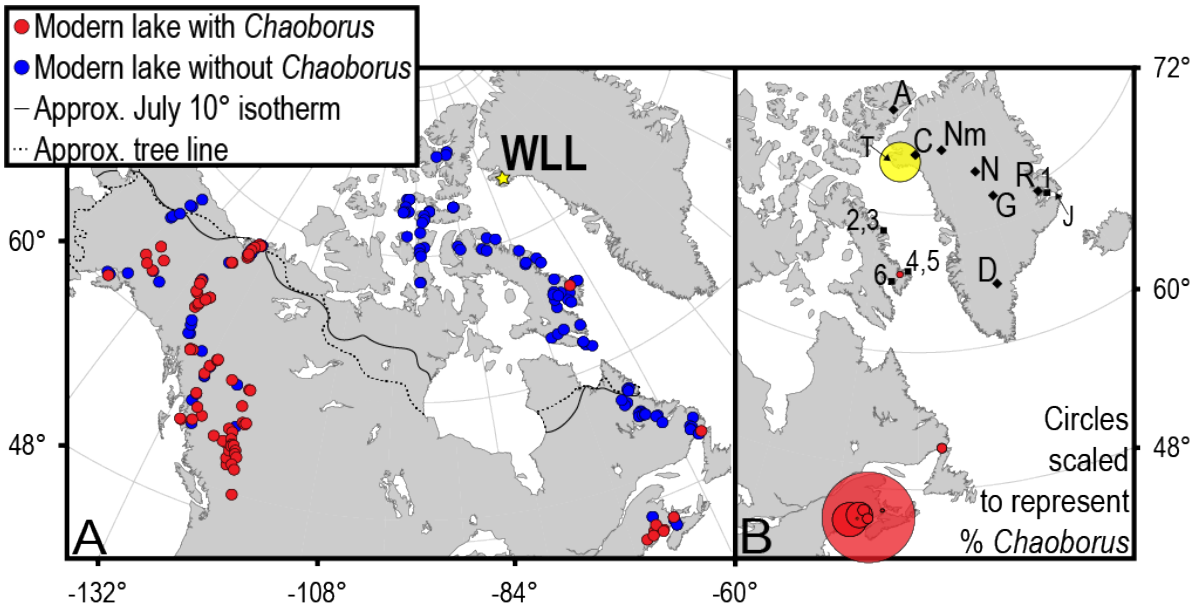

Figure 3.1 *(a) Location of WLL (yellow star) relative to modern July 10°C isotherm (solid black line) and boreal tree line (dashed black line)(D'Odorico et al., 2013). Lakes in two North American midge training sets (Barley et al., 2006; Francis et al., 2006) with (red circles) and without (blue circles) Chaoborus in modern sediments. (b) Percentages of Chaoborus in modern sediments (red circles) vs. WLL LIG assemblages (yellow circle). Circles scaled to represent percent of midge assemblage in each lake, with northernmost red circle <1%, largest red circle 13.6%, and yellow circle 6% Chaoborus. Locations of ice core archives (black diamonds) and lacustrine archives (black squares) discussed in text (see Table 3.1; additionally, N=NGRIP, C=Camp Century, D=DYE3)*

3.3 Results

WLL is a small (9 m deep, <100 m^2) non-glacial lake situated 517 m above sea level in the highlands of northwest Greenland, 60 km east of Thule Air Base and 400 km west of the NEEM site (77.45°N, 51.06°W) (Figure 3.1). WLL is 2 km from the current margin of the GrIS but topographically isolated from meltwater drainage. Several replicate sediment cores were obtained from WLL in 2012 and 2014 (Figure 3.2). All are predominately composed of gyttja with abundant bryophyte material. Horizontal laminae are visible in x-radiographs throughout most of the record including the basal sediments, illustrating intact stratigraphy. A major stratigraphic boundary is correlative across cores

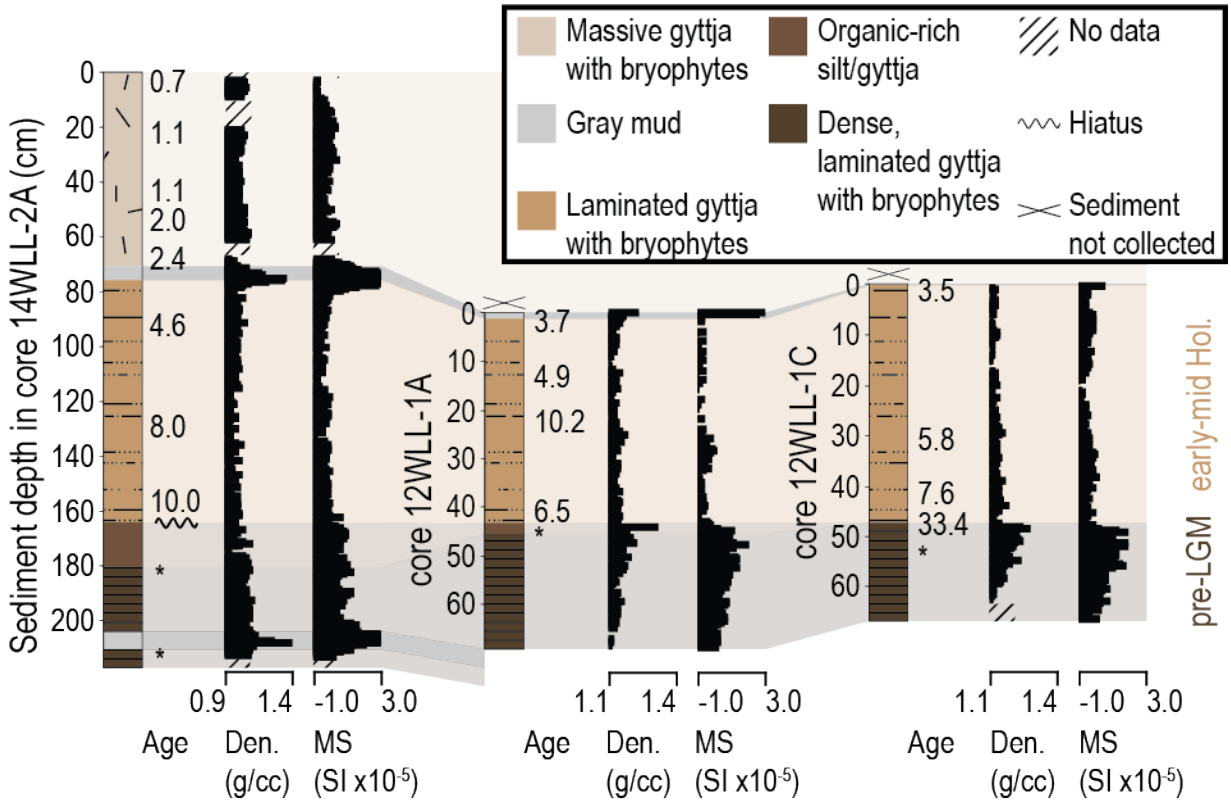

Figure 3.2 *Stratigraphy of three WLL cores, with calibrated ^{14}C ages (cal yr BP), density (Den.), and magnetic susceptibility (MS). * indicates locations of non-finite ^{14}C samples.*

manifesting as a color change from darker basal sediments to lighter brown gyttja above, and a corresponding step decrease in both magnetic susceptibility and density. Aquatic mosses preserved in the gyttja below this boundary yield AMS ^{14}C ages that predate the last glacial maximum (LGM) (4 out of 5 are non-finite), whereas aquatic mosses above this boundary yield exclusively Holocene ^{14}C ages and record lacustrine deposition throughout the Holocene. Given age uncertainties that result from multiple ^{14}C age reversals within the Holocene sediments, we interpret the Holocene biostratigraphy at coarse temporal resolution. Living aquatic moss collected from WLL yielded a post-bomb ^{14}C age. The occurrence of non-finite ^{14}C ages immediately underlying Holocene ages indicates that the major stratigraphic boundary in the cores is an unconformity separating pre-LGM from Holocene sediments.

Similar *in situ* pre-LGM lake sediments have been documented in other Arctic regions with relict landscapes formerly overridden by cold-based, i.e. frozen-bedded and thus minimally erosive, ice (Briner et al., 2007; Axford et al., 2011). Features on the landscape surrounding WLL are analogous to landscapes around lakes on Baffin Island that preserve LIG sediments despite having been overridden by a frozen-bedded portion of the Laurentide Ice Sheet (Briner et al., 2007), supporting a similar history at WLL. The GrIS expanded over WLL to reach its documented extent on the continental shelf during the LGM (Funder et al., 2011). Despite this, and like glaciated relict landscapes on Baffin Island, WLL is surrounded by a weathered highland landscape of tors and angular boulder fields, patterned ground and minimal fine-grained sediments. Bedrock and glacially transported boulders on these highlands contain cosmogenic nuclide inheritance from prior periods of exposure (Farnsworth et al., 2018) providing local evidence for minimally erosive ice cover during the LGM. The compacted nature of the pre-LGM sediments in WLL, reflected in higher magnetic susceptibility and density, is consistent with dewatering during compression by overriding non-erosive ice. Combined, the geomorphic

and stratigraphic evidence indicates cold-based ice advanced over WLL during the LGM, and compacted and preserved pre-LGM lake sediments. The unconformity between pre-LGM and Holocene sediments in WLL represents a hiatus in deposition during glacial conditions, and could also reflect some erosion of pre-LGM sediments that nonetheless left the underlying sedimentary structure intact.

We estimate mean July air temperatures based upon subfossil midge (Diptera: Chironomidae and Chaoboridae) assemblages, employing the climatically and biogeographically relevant training set of Francis et al. (2006), which compiles calibration data from 68 northeast North American lakes spanning from the Canadian Arctic islands to Maine and a July air temperature range from 6 to 18°C (Francis et al., 2006). The Francis et al. (2006) dataset incorporates both Chironomidae and Chaoboridae, the latter of which is not enumerated in many other training sets. This training set has been used in east and west Greenland (Axford et al., 2013; Axford et al., 2017) and in a comparable climate on Baffin Island ~700 km from WLL (Francis et al., 2006; Axford et al., 2011). No midge-temperature calibration dataset is available from mid to high arctic Greenland. Squared-chord distances (SCD) quantifying dissimilarity between subfossil assemblages and the training set demonstrate that almost all WLL samples have a very close modern analog (defined as SCD lower than – i.e., more similar than – the 5th percentile of SCDs in the training set), with just a few late Holocene assemblages above this threshold (Overpeck et al., 1985; Simpson, 2007).

Holocene temperature. Midge assemblages during the early Holocene were characterized by the relatively thermophilous Tanypodinae and *Psectrocladius,* and absence of cold stenotherms that are abundant in the late Holocene sediments of WLL and common in lakes in the high Arctic today (Francis et al., 2006; Fortin et al., 2015; Axford et al., 2017). We estimate that July air temperatures were up to 4.0-7.0°C warmer than modern (reference period

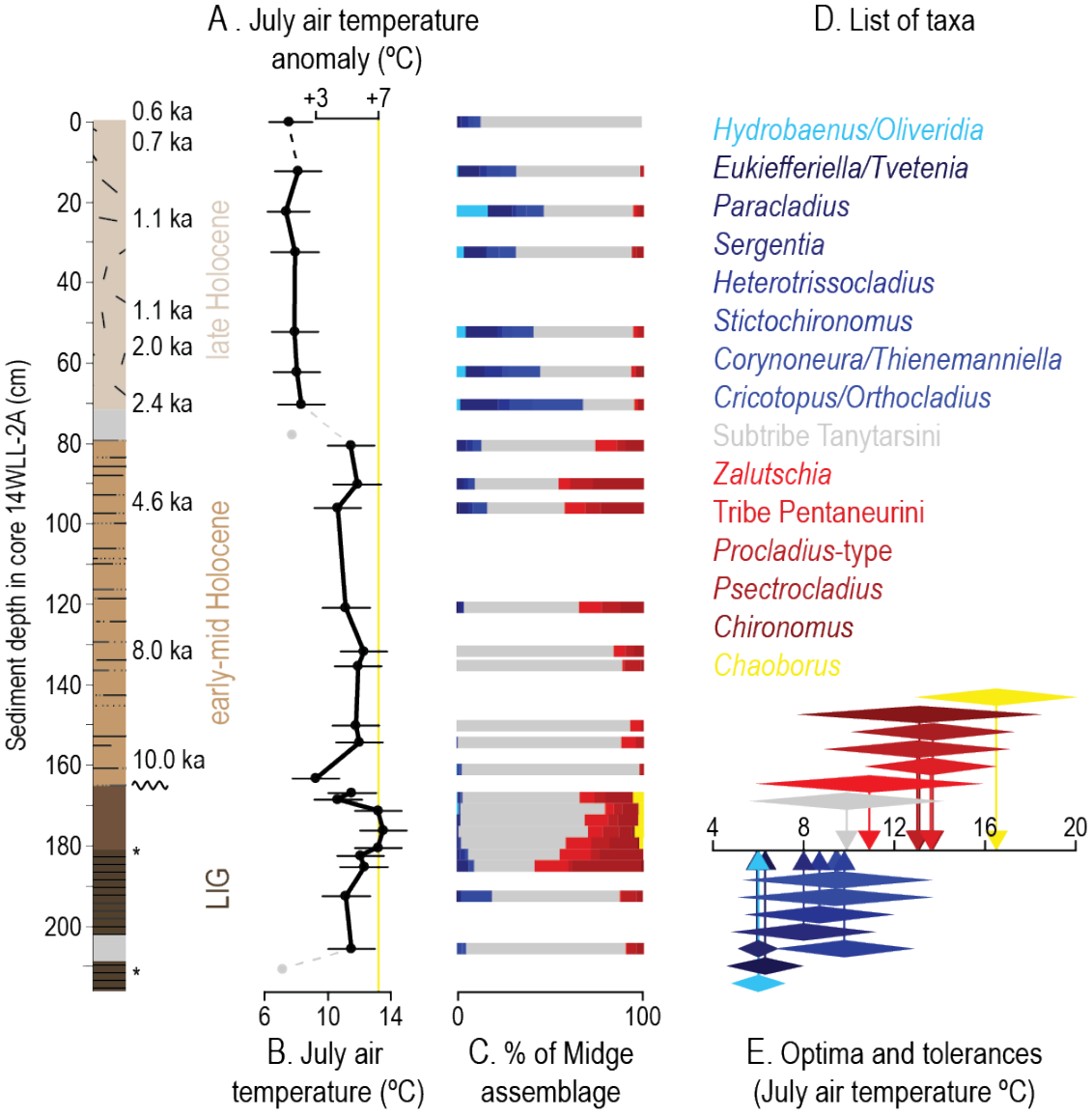

Figure 3.3 *Midge-inferred July air temperature at WLL as (a) anomalies relative to modern and (b) absolute temperatures. Yellow line marks anomaly of +7.0°C. Gray points indicate samples from discrete glaciolacustrine units where midge assemblages may not accurately reflect air temperatures (see Appendix B). Error bars are model RMSEP ±1.5°C. (c) Percent of each midge type in subfossil assemblage, with colors corresponding to taxon names in (d) and modern optima and tolerances of taxa in Francis et al. (2006) training set, as shown in (e). Apex of each diamond in (e) indicates optimum while length of diamond indicates tolerance.*

AD 1952-2012) during the warmest millennia of the Holocene at WLL 10-8 ka (Figure 3.3). We consider this an upper bound on warming because adjusting for postglacial isostatic rebound would reduce this estimate, although likely by a fraction of a degree (Lecavalier et al., 2014). A 7700-year record of lake water $\delta^{18}O$ in Secret Lake (SL), 35 km southwest of WLL (Lasher et al., 2017), is too young to record peak temperatures of the early Holocene but indicates summer-biased warming of 2.5-4.0 ± ~2°C vs. modern from 7.7-6.5 ka, providing a validation (agreement within model errors) of our estimates for this time and an independent loose lower bound on Holocene warming in the region.

Evidence for cooling in the late Holocene at WLL – a decline in warm-dwelling taxa and an increase in cold-dwelling taxa – mirrors isotope-based temperature estimates from SL (Lasher et al., 2017). The coldest stenotherms, *Hydrobaenus*/*Oliveridia* (Figure 3.3C), are most abundant at WLL during the coldest period at SL, suggesting these nearby lakes cooled in unison through the late Holocene. However, we note that WLL temperatures inferred from midges plateau throughout the coldest part of the Holocene 2.5-0.5 ka (Lasher et al., 2017). This reflects a known limitation of our method: the training set includes few calibration sites colder than our study site, limiting its utility for reconstructing very cold past climates (Francis et al., 2006; Axford et al., 2011; Axford et al., 2013; Axford et al., 2017). This does not affect temperature estimates for periods warmer-than-present at WLL because the reconstructed warmer temperatures are well within the range of the calibration data (6-18°C), and these downcore assemblages all have close modern analogs in the training set.

Pre-LGM temperatures and assignment of the pre-LGM unit to the Last Interglacial. The pre-LGM sediments at WLL record peak July air temperatures 5.5-8.5°C warmer than modern, with this warmth supported by the presence of up to 6% of the currently extralimital "phantom midge" *Chaoborus* (Figure 3.3C). In North American training sets

Chaoborus are mostly found at latitudes south of the 10°C July isotherm (Barley et al., 2006; Francis et al., 2006) (Figure 3.1A) and they are abundant (>1.5%) only at the lowest latitudes of our calibration dataset (Francis et al., 2006) (e.g., in Labrador; Figure 3.1B). To our knowledge, neither extant nor subfossil *Chaoborus* have previously been reported from Greenland (Borkent, 1993; Jensen and Christensen, 2003), and *Chaoborus* are absent from the Holocene sediments of WLL. Other relatively warm-dwelling taxa including *Chironomus* and Tanypodinae achieve peak abundance in the pre-LGM sediments.

Although there are no absolute dates for the pre-LGM unit of WLL, we confidently assign it to the LIG because: (1) Non-finite ^{14}C ages indicate that this unit is >45,000 years old. (2) Thermophilous midge assemblages constrain it to a period of sustained full interglacial warmth, exceeding the maximum temperatures of the Holocene. The LIG/Eemian is the most recent known period of sustained temperatures warmer than the early Holocene in the Arctic. And (3) glacial geologic evidence including ^{10}Be dates support cold-based conditions at the site during the most recent glacial period. Thus, the geologic setting permitted preservation of LIG sediments, whereas the probability of preserving sediments from an even older warm period, but not from the LIG, is very low.

The long glacial period between the LIG and Holocene is represented by a hiatus in deposition. Although *Hydrobaenus/Oliveridia* at the top of the pre-LGM unit suggests declining temperature after the LIG maximum, we cannot rule out some erosion of LIG sediments. Therefore, we cannot be certain that we capture the entire LIG, and the maximum temperature anomaly reconstructed at WLL should be viewed as a *minimum* constraint on peak LIG warmth.

3.4 Discussion

At WLL, peak July air temperatures of the early Holocene 10-8 ka are estimated at up to 4.0-7.0°C warmer than modern and overlap in time with the Northern Hemisphere maximum in summer insolation (Buizert et al., 2018). The onset of sediment accumulation in WLL ~10 ka indicates a rapid deglaciation of the nearby GrIS margin, having receded to at least near its present-day position by that time. Reconstructed LIG temperatures are *at least* 5.5-8.5°C warmer than modern at WLL. Unlike the HTM, LIG warming was associated with the migration of the presently extralimital taxon *Chaoborus* to WLL (Jensen and Christensen, 2003), suggestive of a significant northward migration of boreal climate conditions during the LIG (Taylor et al., 2015). This inference is also supported by low and sub-arctic terrestrial and marine fauna preserved in fluvial and raised shallow marine sediments near Thule and Jamesonland in east Greenland (Funder, 1990; Bennike and Böcher, 1992; Bennike and Böcher, 1994; Kelly et al., 1999). Results at WLL are consistent with prior studies showing that peak Arctic warmth during the LIG exceeded that of the HTM, consistent with the larger insolation anomaly and earlier penultimate deglaciation in the LIG (CAPE-Last Interglacial Project Members, 2006). The magnitude of warming during both periods over northwest Greenland suggests that strong positive feedbacks may enhance warming in this region, which could portend stronger-than-predicted warming there in the future. Importantly, WLL temperature estimates reflect summer conditions near the GrIS margin– i.e. the season and setting that control ice sheet surface melt (Goelzer et al., 2016; Buizert et al., 2018).

The amplitude of our HTM summer temperature anomaly agrees with the minimum bound on early Holocene summer warming of 3-4°C vs. modern inferred from melt on Agassiz ice cap ~500 km to the northwest of WLL (Lecavalier et al., 2017). WLL estimates of summer HTM climate for northwest Greenland are ~2°C warmer than both the previous estimates of

precipitation-weighted (annually integrated) warming over Greenland (Vinther et al., 2009; reinterpreted in LeCavalier et al., 2017) and recent simulations of early Holocene summer temperatures in the Thule/Camp Century region (Buizert et al., 2018). Evidence for strong warming in the early Holocene contradicts some Holocene climate models that suggest delayed and attenuated HTM warming here due to effects from the waning Laurentide Ice Sheet (Zhang et al., 2016).

In simulations of the Holocene evolution of the GrIS, imposed HTM warming is typically extrapolated from central Greenland and assumed to be relatively homogenous across broad regions of the ice sheet (Simpson et al., 2009; Lecavalier et al., 2014). The use of more resolved temperature forcings is limited by a lack of paleotemperature estimates for the HTM from Greenland's margin. Thus, extrapolated and/or scaled temperature forcings are currently a large source of unavoidable uncertainty in such simulations (Simpson et al., 2009; Lecavalier et al., 2014). Many models fail to capture the 0.5-1 km of thinning registered at Camp Century in the early Holocene (Lecavalier et al., 2013; Lecavalier et al., 2014) without applying a larger temperature anomaly at Camp Century (Lecavalier et al., 2017). WLL is situated ~150 km from Camp Century and provides an independent estimate of local summer temperature. The +4.0-7.0°C temperature anomaly from 10-8 ka at WLL matches well with a modeled temperature time series for Camp Century based on the revised Agassiz reconstruction (LeCavalier et al., 2017). Together, these studies help explain dramatic thinning observed at Camp Century and quantify the regional summer air temperatures associated with Holocene elevation change.

The reconstructed strong LIG warming at WLL of *at least* 5.5-8.5°C vs. modern is consistent with the controversial estimate of 8±4°C precipitation-weighted warming vs. the last millennium at NEEM (Dahl-Jensen et al., 2013). This estimate from WLL is warmer than prior estimates of +4-5°C vs. modern from biotic remains preserved in discontinuous terrestrial

deposits near the Thule Air Base (Bennike and Böcher, 1992). However, given likely incomplete preservation, these prior results provide a minimum bound on local LIG warmth. Agreement between the anomalies at WLL and NEEM suggests that ice $\delta^{18}O$ precipitation-weighted temperature was strongly summer-biased at NEEM during the LIG, or else there was also significant isotopic enrichment of non-summer precipitation, possibly from a longer period of sea ice-free conditions in Baffin Bay (Steen-Larsen et al., 2011; Masson-Delmotte et al., 2015), and/or similarly large average annual warming due to changes in atmospheric circulation (Cohen et al., 2014). Together, the WLL, Agassiz Ice Cap and NEEM records provide evidence from multiple sites and proxies for strong HTM and LIG summer warming over northern Greenland and Ellesmere Island – Earth's largest land masses at such northerly latitude. Only a subset of climate models of the HTM and LIG simulate the warmest continental temperature anomalies at these very highest Arctic latitudes (Lunt et al., 2013; Bakker et al., 2014; Buizert et al., 2018). Paleoclimate data here and elsewhere (CAPE-Last Interglacial Project Members, 2006; Turney and Jones, 2010) support this subset of models.

For the LIG, evidence for intense summer warming over northern Greenland exacerbates the paradox embodied at NEEM (Goelzer et al., 2016), where data indicate both strong LIG warming and, in contrast, only a relatively modest reduction in ice sheet thickness (-130 ± 300 m relative to present) (Dahl-Jensen et al., 2013; Yau et al., 2016). Ice sheet models thus far cannot simultaneously accommodate observations of large warming over the GrIS and geologic evidence for a widespread GrIS throughout the LIG (Otto-Bliesner et al., 2006; Goelzer et al., 2016; Yau et al., 2016). This paradox could be resolved if LIG summer warming was localized to the central ice sheet, or LIG warming was relatively weak in summer, limiting surface melt (Goelzer et al., 2016). However, WLL temperature estimates reflect pronounced summer warming at the margin of the GrIS, and thus argue against both explanations. Nor is it likely that

the northern GrIS is somehow inherently insensitive to warming: to the contrary, some models have suggested the arid northern GrIS may be especially sensitive to warming (Born and Nisancioglu, 2012; Stone et al., 2013), and dramatic GrIS thinning at Camp Century during the HTM also challenges this notion (Lecavalier et al., 2017). Furthermore, intense warming was not necessarily unique to the northernmost part of the ice sheet: GISP2 (Summit) does not definitively capture peak warmth during the early LIG, but now provides a *minimum* constraint on peak LIG anomalies of +4-8°C over central Greenland Yau et al., 2016). Collectively and based upon multiple independent proxies, the WLL, NEEM, and GISP2 records point to larger LIG warming across Greenland than the +4-5°C hitherto often estimated (CAPE-Last Interglacial Project Members, 2006; Turney and Jones, 2010).

Greater snow accumulation over north Greenland during the LIG might help resolve the LIG paradox in this region (Helsen et al., 2013). There is some evidence for increased snowfall in west Greenland during the HTM (Thomas et al., 2016), although it was apparently not enough to counteract ice sheet thinning at Camp Century (Vinther et al., 2009). Current paleoclimate data poorly constrain LIG snowfall over Greenland, and models suggest relatively modest LIG increases in snowfall (Born and Nisancioglu, 2012), but the hypothesis of greater accumulation during the LIG is supported by recent observations for a strong relationship between accumulation and temperature at the NEEM site (Masson-Delmotte et al., 2015) and evidence for greater accumulation during the LIG than the Holocene at Summit (Yau et al., 2016). Additional reconstructions of LIG precipitation, temperatures and ice sheet configuration are urgently needed to formulate stronger paleoclimate model-data comparisons and ultimately to further improve models of Greenland's climate and ice sheet behavior.

3.5 Conclusions

July air temperature estimates at WLL indicate pronounced warming during both the HTM and the LIG. The data presented here from a rare lake record of two interglacials agree with previous disparate reconstructions of exceptional warming over Ellesmere Island for the HTM and northern Greenland during the LIG, illustrating consistently strong regional warming during interglacials. Strong summer warming over northern Greenland, demonstrated by temperature anomalies at WLL of up to +4.0-7.0°C for the HTM and at least +5.5-8.5°C for the LIG, should be accommodated in future paleoclimate simulations and models of ice sheet evolution. In addition, if this large magnitude of HTM and LIG warming resulted from cryospheric or other feedbacks, such strong warming at WLL may portend even larger changes over this region than predicted in the coming century, as the Arctic warms to levels unprecedented since the LIG (Axford et al., 2011; Collins et al., 2013).

3.6 Materials and Methods

For ^{10}Be dating, we sampled flat-lying upper surfaces of quartz-rich, stable perched boulders and bedrock, and avoided surfaces that experienced past water cover as evidenced by traces of former lake levels. ^{10}Be samples were processed at Dartmouth College and ^{10}Be/^{9}Be was measured at the Center for Accelerator Mass Spectrometry at Lawrence Livermore National Laboratory, following standard procedures. Ages were calculated using the Cosmic-Ray Produced Nuclide Systematics -Earth online calculator (Balco et al., 2008) with the Baffin Bay/Arctic production rate (Young et al., 2013).

Cores were collected from the depocenter of WLL using a modified-Bolivia percussion coring system in 2012 and a Nesje percussion coring system in 2014. Some cores intentionally bypassed surface sediments to maximize recovery of older sediments. Measurements of magnetic

susceptibility and gamma density followed standard procedures, as described in the SI Appendix. ^{14}C AMS ages were obtained on aquatic plant macrofossils picked from intact laminations and analyzed at Woods Hole Oceanographic Institution-National Ocean Sciences Accelerator Mass Spectrometry facility. Calibration to cal yrs BP followed standard practices described in Appendix B.

Preparation and classification of midge subfossils followed standard methods as described in Appendix B. July air temperatures were modeled using the Francis et al. (2006) training set (44 taxa; r^2jack=0.88; Root Mean Standard Error of Prediction=1.53°C) (Francis et al., 2006). We use bootstrapping but otherwise follow protocol of Francis et al. (2006) for the model parameters yielding best model performance: Assemblage data were square-root transformed and temperature estimates were derived from a WA model using inverse deshrinking and tolerance down-weighting with bootstrapping. Modern (AD 1952-2012) mean July air temperature at the coastal Thule (Pituffik) weather station is 5.2°C (Wong et al., 2015). We observed with air temperature loggers deployed at our field sites in 2012-2014 that July air temperature at WLL is 1°C warmer than at Thule, and estimated modern July air temperature for the reference period (AD 1952-2012) at WLL as 6.2°C. Modern analog technique (MAT) was used to calculate dissimilarity between WLL subfossil samples and the training set, as squared-chord distances on untransformed assemblage data (Overpeck et al., 1985; Simpson, 2007)(37,38).

3.7 Acknowledgements

Collaborators on this work include Yarrow Axford, Magdalena Osburn, Meredith Kelly, Erich Osterberg, and Lauren Farnsworth. Additional recognition for assistance is given to the people and Government of Greenland for site access (sample export permit #028/2014). This

work was funded by the National Science Foundation (NSF) Division of Polar Programs (awards 1108306 and 1107411), a NSF Graduate Research Fellowship, the Geological Society of America, and the Institute for Sustainability and Energy at Northwestern. M. Bigl, G. Bromley, M. Jackson, G.E. Lasher, E. Roy and A. Taylor assisted with field work, and the Thule Air Base, Air Greenland, the United States Air Force, J. Hurley, K. Cosper, and Polar Field Services provided logistical support. C. Carrio, G. Schellinger and T. Stilson helped in the lab at Northwestern. LacCore, the Woods Hole Oceanographic Institution National Ocean Sciences Accelerator Mass Spectrometry facility, the Center for Accelerator Mass Spectrometry at Lawrence Livermore National Laboratory, and J.P. Brown and the Field Museum provided additional analytical support. Maps were created using The Generic Mapping Tools. J. Townsend, C. Kuzawa and two anonymous reviewers provided thoughtful comments on the manuscript.

Chapter 4

Greenland Ice Sheet mass loss during two interglacials despite paleohydrologic evidence for increased atmospheric moisture

4.1 Abstract

Air temperature and precipitation over the Greenland Ice Sheet (GrIS) are both expected to increase in the coming century. How these changes in local climate impact the long-term surface mass balance remains an open question, relevant to predicting future rates of global sea level rise. Here, we show that atmospheric moisture increased by ~ 30% in northwest Greenland with Holocene and LIG warming, relative to the cool late Holocene. Using a comparison between isotopes of lake water, isotopes of leaf water, and published records of GrIS evolution, we show that GrIS growth occurred only during the coldest and regionally most arid period of the Holocene. In contrast, the GrIS strongly retracted during the warm and regionally wet conditions of the middle Holocene and LIG. This indicates that an increase in precipitable moisture did not strongly influence Holocene and LIG GrIS mass budget in northwest Greenland, and suggests future GrIS loss in this region may be partially mitigated but not cancelled by increased accumulation.

4.2 Introduction

By the end of this century, global mean surface air temperatures are projected to surpass the +2-4°C threshold at which models indicate sustained warmth will lead to total loss of the Greenland Ice Sheet (GrIS) (Robinson et al., 2012; Collins et al., 2013; Clark et al., 2016). Projected rates of 21st Century mass loss from Earth's ice sheets are poorly constrained, with Antarctica being especially uncertain, but with Greenland also contributing to the large envelope

around IPCC predictions of sea level rise by 2100 AD (Church et al., 2013). More uncertain is when total loss of the GrIS will occur in the longer term under sustained warmth, and thus the timing of its 7 m contribution to global sea level (Robinson et al., 2012).

Surface mass balance (SMB) of the GrIS is a function of gain from accumulation and loss from ablation across the ice sheet (Helsen et al., 2013; Vernon et al., 2013). Although warmer temperatures will increase melt, particularly in low-elevation ablation zones at the ice sheet margins, they will also contribute to greater atmospheric moisture and thus increased precipitation (Collins et al., 2013; Vernon et al., 2013; Plach et al., 2018). Modern observations in northwest Greenland show strong increases in precipitation at coastal sites, up to 4 times that of other regions in Greenland (Wong et al., 2015), and future accumulation may increase over the northern GrIS by up to ~11% for every 1 degree C increase in global mean air temperature (Masson-Delmotte et al., 2015). Despite evidence for a negative total mass budget (SMB and ice discharge) of both polar ice sheets in recent decades, modest increases in precipitation have already mitigated surface melt by up to ~100 % in Greenland (Fettweis et al., 2008; van den Broeke et al., 2009) and offset ice discharge by ~35% in Antarctica (Medley and Thomas, 2019).

For Greenland, ice sheet models have difficulty matching the size of the GrIS inferred from geologic data for the Holocene and the LIG (Simpson et al., 2009; Lecavalier et al., 2014; Goelzer et al., 2016; Lecavalier et al., 2017; McFarlin et al., 2018). For example, it remains a perplexing question how the GrIS maintained as much mass as is apparent in geologic records throughout the LIG, despite strong warming over much of the ice sheet (i.e. the “NEEM paradox”) (Dahl-Jensen et al., 2013; Goelzer et al., 2016; Yau et al., 2016; McFarlin et al., 2018), in contrast to the surprising extent of thinning observed in some regions with Holocene warming (Vinther et al., 2009; Lecavalier et al., 2013; Lecavalier et al., 2014). Greater precipitation over Greenland has been hypothesized to explain some data-model discrepancies

(Young and Briner, 2015; McFarlin et al., 2018), although at present there is little empirical evidence to validate this hypothesis. Further, climate models do not demonstrate extensive increases in precipitation during these periods, and therefore GrIS models for the Holocene and the LIG do not indicate a significant influence on mass balance from accumulation (Born and Nisancioglu, 2012). Instead, many models indicate SMB was dominated by summer melt at the margins (Goelzer et al., 2016; Buizert et al., 2018), which probably drove rapid retreat (Otto-Bliesner et al., 2006). Because geologic evidence for hydroclimate across Greenland during these periods is extremely scarce (Sundqvist et al., 2014; Briner et al., 2016; Linderholm et al., 2018) ice sheet models lack robust geologic validation of these trends (Robinson et al., 2012; Plach et al., 2018). Further, ice sheet models demonstrate that SMB for the LIG is very sensitive to how temperature, melt and precipitation are estimated (Plach et al., 2018). It remains important to test if precipitation increased more than is currently modelled through these periods, especially across different regions of the island and at the margins of the ice sheet.

Records of past atmospheric moisture that can be integrated with climate and ice sheet reconstruction models are rare in the Arctic because there are few quantitative proxies for precipitation amount, relative humidity, or evaporation (Sundqvist et al., 2014; Briner et al., 2016; Linderholm et al., 2018). That past warming is accompanied by greater precipitation over some of Greenland is supported by up to a 500% increase in accumulation (from 0.05 to 0.25 mm/yr) over the north and central GrIS between the Last Glacial Maximum and the Holocene (Rasmussen et al., 2013), and moderately increased ice accumulation in the early Holocene and LIG (Cuffey and Clow, 1997; Yau et al., 2016). At present, the qualitative data on Holocene hydroclimate at the margins of the GrIS strongly disagree on the direction of moisture balance with warming (Table 4.1)(McGowan et al., 2003; Anderson and Leng, 2004; Andresen et al., 2004; Anderson et al., 2012; Perren et al., 2012; Balascio et al., 2013; Thomas et al., 2016),

Table 4.1 Summary of published data showing trends in moisture on the margins of the GrIS through the Holocene (rounded to nearest ky). Orange shading represents "Dry conditions" i.e. inferred negative P-E or aridity, while blue shading represents "wet conditions" i.e. inferred positive P-E or humidity. Gray shading is neutral or no data. Sites correspond to Figure 1.1

Site	Proxy	Age (ka) 9 8 7 6 5 4 3 2 1 0	Source
Flower Valley	δ^2H-values of *n*-alkanes (C_{25}+C_{27} vs. C_{29}+C_{31})		(Balascio et al., 2013)
Narsaq	Sed. composition		(Andresen et al., 2004)
Narsaq	Sed. composition, pollen, diatoms		(Massa et al., 2012)
Kangerlussuaq	Mineral flux		(Anderson et al., 2012)
Kangerlussuaq	Paleo shorelines		(Aebly and Fritz, 2009)
Kangerlussuaq	diatoms		(Perren et al., 2012)
Kangerlussuaq	diatoms		(McGowan et al., 2003)
Kangerlussuaq	δ^{18}O-values of authigenic calcite		(Anderson and Leng, 2004)
Kangerlussuaq	pollen		(Eisner et al., 1995)
N3	δ^2H-values of *n*-acids (C_{24})		(Thomas et al., 2016)
Sikuiui	δ^2H-values of *n*-alkanes (C_{23} vs. C_{29})		(Thomas et al., 2018)
Wax Lips Lake	δ^{18}O-values of chironomid, δ^2H-values of *n*-alkanes (C_{29})		This study

perhaps suggesting strong spatial heterogeneity or that the moisture proxies used were affected by other environmental gradients. For example, Thomas et al. (2016) argue for a major increase

in winter precipitation in west Greenland during the middle Holocene, whereas McGowan et al. (2003) and Anderson and Leng (2004) argue for a period of strong aridity in the early and middle Holocene also in west Greenland. Balascio et al. (2013) argue for a drier early-middle Holocene and a more humid late Holocene in southeast Greenland, while Andresen et al. (2004) argue for the opposite in south Greenland. No clear consensus exists from paleoclimate records on just how much moisture balance changed through the Holocene for any region of Greenland. Apart from work presented here, virtually no geologic records of past precipitation on the GrIS margin exist from the LIG. Thus, there are few clues from the geologic record indicating how important warming-associated changes in precipitation on the GrIS margin are to SMB. Stronger evidence for the behavior of precipitation through past interglacials, particularly on the margins of the GrIS, is necessary for a robust understanding of the relationship between atmospheric moisture and GrIS extent with warming. In short, we seek evidence to test the hypothesis that increased precipitation at ice margins offset melt enough to explain some of the data-model discrepancies for the Holocene and/or the LIG.

To analyze how atmospheric moisture changed on northwest Greenland throughout the Holocene and part of the LIG, we utilize the hydrogen isotopic composition of sedimentary C_{29} *n*-alkanes as a proxy for plant growth water (see Chapter 2), alongside the oxygen isotopic composition of subfossil chironomid larvae as a proxy for lake water (van Hardenbroek et al., 2018). Both proxies were recently validated on Greenland (for leaf wax validation, see Chapter 2), lending new confidence that they reliably record isotopes of plant growth water and lake water, respectively (Lasher et al., 2017; van Hardenbroek et al., 2018; Lasher and Axford, 2019). Comparing these proxies illuminates the extent to which evapotranspiration modifies terrestrial leaf water relative to meteoric water (Farquhar et al., 2007), the latter being represented by lake water at hydrologically appropriate sites. We analyze these proxies at Wax Lips Lake (WLL;

77.45°N, 51.06°W), a small nonglacial lake in northwest Greenland (see Figures 1.1 and 3.1), where an unusual package of *in situ* LIG and Holocene lake sediments is preserved, and compare these hydroclimate proxies to published summer air temperatures from the same sedimentary record (see McFarlin et al., 2018 for site and sediment core descriptions and chronology). As a novel methodological contribution, we utilize oxygen isotopes as a lake water proxy instead of wax compounds commonly ascribed to aquatic plants. Work in Chapter 2 demonstrates that modern sedimentary mid-chain plant waxes (e.g. C_{23} *n*-alkanes), often employed as a proxy to reconstruct the isotopes of lake water (Nichols et al., 2006; Aichner et al., 2010; Aichner et al., 2017; Zhang et al., 2017; Thomas et al., 2018), show a poor correlation to modern lake water across a broad range of latitudes in Greenland.

At present, this high Arctic site is very cold (mean July air temperature is 6.2°C, 1952-2014; McFarlin et al., 2018); nearby mean annual air temperature at Thule averages ~ -11°C, 1958-1999) and extremely arid (<150 mm precipitation/year), with most precipitation delivered in the summer and fall (~70%) (Cappelen et al., 2001). The modern vegetation zone is middle Arctic continental, dominated by perennial herbs and dwarf willow (Jensen and Christensen, 2003). The hydrogen isotopic range (δ^2H values relative to VSMOW) of precipitation in this region spans from ~ -280‰ in the winter to -150‰ in the summer, with seasonally-weighted mean annual precipitation ~ -180 ‰ (Bowen and Revenaugh, 2003; IAEA/WMO, 2017; Bowen, 2018). WLL is nonglacial (excepting two discrete and readily-identifiable periods of glaciolacustrine sedimentation not included in analyses here, described in McFarlin et al., 2018) and within the continuous permafrost zone, and therefore lake water is dominantly derived from precipitation. It was observed during fieldwork in 2014 that the lake is currently through-flowing in the summer. Modern late summer (August) lake water at WLL is isotopically identical to summer precipitation at ~ -150 ‰ (see Table 2.1) and corresponds with the local precipitation

line (IAEA/WMO, 2017), indicating weak cumulative influence on lake water from summer evaporation and winter sublimation. Further, aerial photography from 1985 demonstrates consistent surface area with 2012 (Google Earth) and 2014 (field photos), supporting that WLL is not a fully closed (evaporating) basin.

4.3 Proxy Interpretation Rationales

Sedimentary Leaf Waxes

Both aquatic (nonvascular) and terrestrial (vascular) plants produce both mid- and long-chain *n*-alkanes, but there are differences in the relative distributions of these compounds predictable by plant form. Non-vascular/aquatic plants dominantly produce mid-chain *n*-alkanes (C_{23}-C_{25}) and vascular/terrestrial plants dominantly produce long-chain *n*-alkanes (C_{27}-C_{31}) (Eglinton and Hamilton, 1967; K.J. Ficken et al., 2000; Nott et al., 2000; Aichner et al., 2010; Nichols et al., 2010; Liu et al., 2015). C_{23} and C_{27} were observed as the dominant mode in modern Greenland aquatic and terrestrial plants respectively from one region of Greenland (Dion-Kirschner et al., 2017; Berke et al., 2019). We apply these observations to qualitatively differentiate changing vegetation sources of *n*-alkanes throughout the WLL record: Where the concentration of $C_{23} >> C_{27}$ and C_{29}, there must be significantly higher input of *n*-alkanes from aquatic plants relative to terrestrial plants, which would otherwise supply more C_{27} and/or C_{29} than C_{23} to the sedimentary record. Conversely, sediment samples that demonstrate ratios where $C_{23} < C_{27}$ (C_{23}:$C_{27} \leq 1$) and C_{29} (C_{23}:$C_{29} \leq 2$) can be interpreted as having significant C_{23} input from terrestrial plants (such that C_{23} is not a reliable aquatic proxy), and that long-chain compounds (C_{29}) in these sediments are dominantly sourced from terrestrial plant waxes. A high sedimentary C_{23}:C_{29} ratio (C_{23}:$C_{27} \geq 1$ and C_{23}:$C_{29} \geq 2$) indicates input from both aquatic and terrestrial sources, and therefore the isotopic composition of these waxes cannot be attribute to

lake water or leaf water exclusively (Nichols et al., 2006; Dion-Kirschner et al., 2017; Zhang et al., 2017). Because there is such ambiguity in the source of compounds where $C_{23} > C_{27}$ and C_{29}, we opt not to interpret the δ^2H values of any *n*-alkanes with high C_{23}:C_{29} ratios. Where $C_{23} < C_{27}$ and C_{29}, we interpret the δ^2H values of C_{29} *n*-alkanes as a proxy for the δ^2H values of summer-biased growth water of terrestrial C3 plants.

Oxygen isotopes of chironomid remains

Larval chironomid are obligately aquatic and utilize lake water for biosynthesis. A strong global correlation (r^2=0.9) between the O isotopic composition of chironomid head capsules and lake water has been demonstrated, including sites from Greenland (Lasher et al., 2017; van Hardenbroek et al., 2018; Lasher and Axford, 2019). In northwest Greenland, the isotopic composition of lake water in the nearby through-flowing Secret Lake, ~50 km west southwest of WLL, was demonstrated to broadly track summer precipitation and thus summer temperature over a 7.7-kyr Holocene record (Lasher et al, 2017). WLL is hydrologically similar to Secret Lake (small, thru-flowing), and Thule receives >70% of annual precipitation during the summer and early fall (Cappelen et al., 2001) and the weighted-annual average is strongly summer-biased (Bowen and Revenaugh, 2003; IAEA/WMO, 2017; Bowen, 2018). We therefore interpret the $\delta^{18}O$ values of sedimentary chironomid head capsules in Wax Lips Lake as a proxy for the $\delta^{18}O$ values of lake water, which is derived from summer-biased precipitation.

Inferring Water: Calibration and modelling approaches

To directly and quantitatively compare changes in leaf water with changes in lake water (and thus precipitation) isotopes through time, we utilize the calibration data for Greenland sedimentary plant waxes from Chapter 2, and recent calibration data for chironomids (van

Hardenbroek et al., 2018) to infer water H and O isotopes from the proxy values. Here, $\delta^{18}O$ values of lake water are calculated from $\delta^{18}O$ of chironomid head capsules using the regression between the two reported in van Hardenbroek et al. (2018). $\delta^{2}H$ values of summer precipitation were calculated from lake water oxygen isotope values using both the global meteoric water line ($\delta^{2}H= 8\delta^{18}O+10$) as a lower estimate and a local evaporation line generated from lake water in Thule (values of lake water reported in Table 2.1) ($\delta^{2}H= 5.5\delta^{18}O-45$) as an upper estimate. Terrestrial plant leaf water is calculated from the $\delta^{2}H$ values of sedimentary C_{29} *n*-alkanes using the Greenland-specific linear relationship between $\delta^{2}H$ values of modern sedimentary C_{29} *n*-alkanes and those of modern summer precipitation. After this calculation, we interpret $\delta^{2}H$ values of C_{29} *n*-alkanes as those of average leaf water of terrestrial plants, which is derived from growth-season precipitation but modified in the leaf by transpiration (Farquhar et al., 2007; Freimuth et al., 2017).

4.4 Results and Discussion

At WLL, C_{23}:C_{29} ratios are high in the earliest Holocene, from ~10 to 8 ka, in the period of landscape development immediately following regional deglaciation (Corbett et al., 2015; Farnsworth et al., 2018; McFarlin et al., 2018) likely reflecting minimal terrestrial vegetation on the landscape but abundant aquatic vegetation in WLL. Pollen data indicates colonizing terrestrial plants established in this region ~9-8 ka, followed by migration of dwarf shrubs and sedges by ~6.7 ka (Fredskild, 1985; Fredskild, 1991). The Holocene C_{23}:C_{29} ratio stabilizes at WLL ~7.5-6.5 ka, concurrent with regional arrival of pollen from higher vegetation (Fredskild, 1985; Fredskild, 1991), suggesting at this point terrestrial plants become the dominant source of sedimentary waxes to WLL. Therefore, the high C_{23}:C_{29} ratio through the early Holocene records

the delay in terrestrial plant colonization following deglaciation, followed by establishment of higher vegetation in the early-middle Holocene, as demonstrated by lower C_{23}:C_{29} ratios. C_{23}:C_{29} is also quite high during peak temperatures of the LIG (McFarlin et al., 2018) when there is evidence for abundant terrestrial vegetation in the Thule area (Bennike and Böcher, 1992), so it is unlikely the high ratio here represents the same vegetation balance as the earliest Holocene (i.e., a lack of terrestrial plants). Rather, it is more likely that production of C_{23} rose substantially during this period, perhaps due to warm lake temperatures resulting in high productivity within the lake, or expansion of boggy habitat ideal for terrestrial mosses.

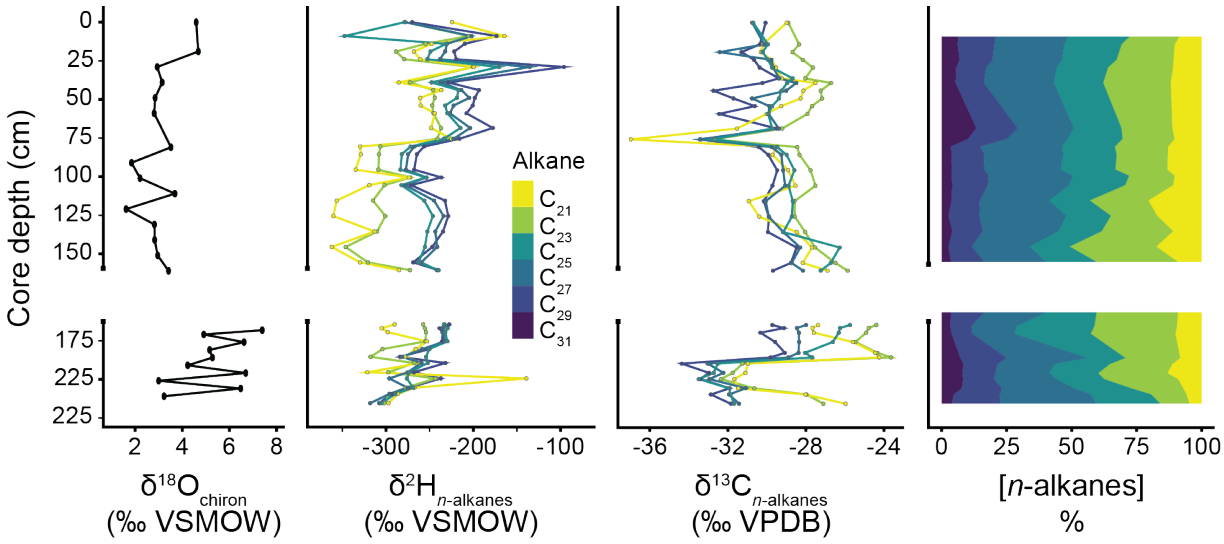

Figure 4.1 *Isotopic composition of chironomid head capsules, and odd-chained n-alkanes; relative concentration (%) of odd -chained n-alkanes in core 14WLL-2A (see Ch. 3)*

The carbon isotopic composition, reported as $\delta^{13}C$ values relative to VPDB, of all sedimentary *n*-alkanes (C_{21}-C_{29}) from WLL ranges from -37 to -23‰, while the $\delta^{13}C$ values of C_{29} *n*-alkanes range from -34 to -28‰ (Figure 4.1). In general, the values of C_{29} agree with observations of $\delta^{13}C$ values of waxes from modern C3 plants (see Chapter 2), supporting the

major source of these compounds in WLL sediments as C3 vegetation, and some input from mosses and aquatic plants (Dion-Kirschner et al., 2017). Overall, the C isotopic composition of all *n*-alkanes follow broadly similar trends, with moderate to high correlation coefficients (≥0.5) between all compounds. In Holocene sediments, $\delta^{13}C$ values of C_{29} *n*-alkanes gently shifts by ~1‰ towards more ^{13}C-depleted values in the late Holocene. The most notable feature of the C isotope record is a ~3-10‰ shift towards more ^{13}C-enriched values midway through the LIG unit, expressed most strongly in C_{21} and C_{23}. This shift is concurrent with the appearance of *Chaoborus* mandibles in the sedimentary record, a large increase in the concentration of C_{23} *n*-alkanes, and a marked increase in summer air temperature inferred via midge assemblages (McFarlin et al., 2018).

Past Hydroclimate in northwest Greenland At WLL, $\delta^{2}H$ values of lake water change relatively little throughout the Holocene, and are consistently within ~10‰ of the mean value. Overall, the isotopic composition of water of WLL is largely stable through both the Holocene, with some indication of increasing evaporative enrichment of lake water in the most recent millennia when regional summer air temperatures are at a Holocene minimum (Lasher et al., 2017; McFarlin et al., 2018).

In contrast, the $\delta^{2}H$ values of leaf water, inferred from C_{29} n-alkanes, are more enriched than lake water for much of the Holocene, by up to ~60‰ (Figure 4.2). The most enriched leaf

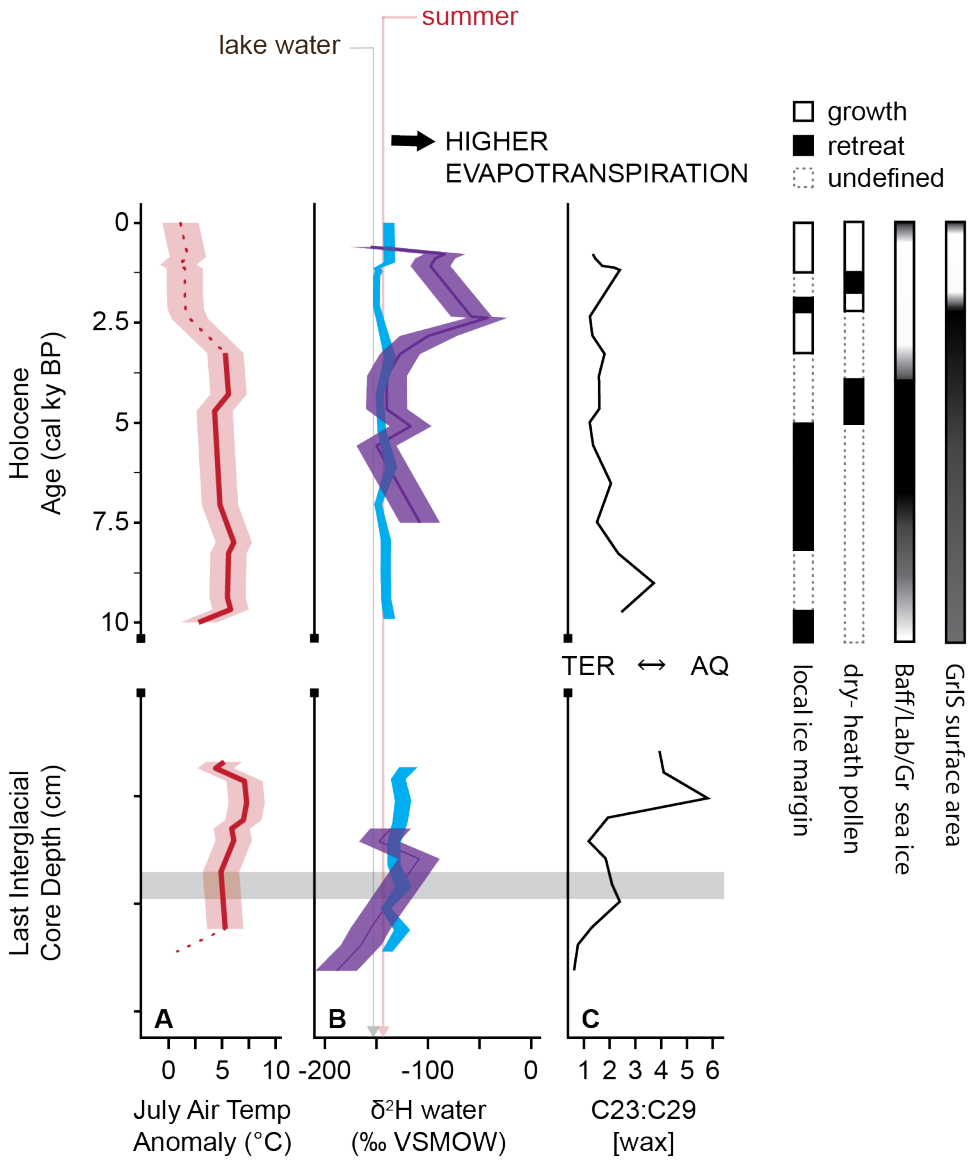

Figure 4.2 *Interpretation of data with panel A) temperature, B) Lake and leaf water from chironomid (blue), C_{29} (purple), gaps in data occur in the LIG and early Holocene because data is not used where C23 >> C29 assessed by C) sedimentary C_{23}:C_{29}. Bars demonstrate timing of regional landscape changes, including shifts in vegetation type of growth/retreat of ice.*

water occurs in the late Holocene, concurrent with modest ^{2}H-enrichment in lake water, inferred from $\delta^{18}O_{chiron}$ in WLL, and the coldest regional summer air temperatures (Lasher et al., 2017;

McFarlin et al., 2018). Leaf water that is strongly enriched relative to WLL lake water, and thus summer precipitation, is a function of strong transpiration enriching leaf water during the early growth season, driven by low relative humidity (Roden and Ehleringer, 1999; Helliker and Ehleringer, 2002; Farquhar et al., 2007).

Using the difference between leaf water and lake water as a metric for transpiration, and assuming a quasi-equilibrium between precipitation (lake water) and atmospheric vapor (Farquhar et al., 2007), we estimate relative humidity in the summer dropped up to ~30-40% in the late Holocene (Table 4.2). Relative humidity during this period was as low as ~60-70%, similar to that observed in the Kangerlussuaq area of Greenland today (Cappelen et al., 2001)(see section 4.6 Materials and Methods). Leaf water δ^2H values that agree with (i.e. are within error of) precipitation δ^2H values indicate that higher atmospheric moisture slowed the rate of transpiration, so that leaf water and precipitation appear in unity. Indeed, using the same leaf-water model as above, we find relative humidity was likely >80-90% for the early growth-season during the middle Holocene, with this estimate a product of the nearly-identical hydrogen isotope values for precipitation and leaf water. Overall, the wettest atmospheric conditions of the last ~8 ky appear in the middle Holocene. These findings are supported by regional pollen data, which demonstrates a shift from vegetation dominated by dwarf shrubs and sedges towards arid-adapted dry-heath and grasses in northwest Greenland ~2 ka (Fredskild, 1985).

For the LIG, δ^2H values of lake water again change relatively little throughout the period preserved in WLL sediments, but are also more ^2H-enriched than δ^2H values of lake water during the Holocene, consistent with warmer summer air temperatures during the LIG than the HTM inferred from chironomid species assemblages (McFarlin et al., 2018). Relative humidity during the LIG prior to peak warmth is estimated at >90%, similar to that of the middle Holocene. We

do not estimate relative humidity during peak LIG warmth because C_{23}:C_{29} ratios indicate the dominant supply of sedimentary waxes was not necessarily from terrestrial plants during this time. However, what is important to note is that leaf water values, where they can be assessed in the LIG, are never more enriched than those of lake water. Further, ^{13}C-enrichment in *n*-alkanes suggests a change in the source of plant waxes, perhaps to more input from aquatic plants and mosses. This suggests there is no period of aridity during the LIG in this record, albeit there is also no period of sustained cool temperatures during the LIG in this record.

Table 4.2 Calculations of relative humidity (rH) using Farquhar et al .(2007) Equation 6 and Temperature from McFarlin et al. (2018), and using 0.01, 0.03 and 0.3 for ε_k to test sensitivity of the model to kinetic fraction factors (Cappa et al., 2003), for Holocene (3.5-0 ka), middle Holocene (7-3.5 ka) and early Holocene (10-7 ka).

Interval	**T (°C)**	**α***	**ε***	**ε_k**	**R_{leaf}**	**R_{precip} (LEL)**	**R_{precip} (GMWL)**	**Δe (LEL)**	**Δe (GMWL)**	rH (LEL)	rH (GMWL)
Late Hol.	6	1.1026	0.1026	0.01	0.894	0.852	0.860	0.050	0.040	**0.554**	**0.641**
Mid Hol.	11.3	1.0951	0.0951	0.01	0.846	0.847	0.852	0.000	-0.007	**1.004**	**1.068**
Early Hol.	11.3	1.0951	0.0951	0.01	0.858	0.847	0.853	0.013	0.006	**0.877**	**0.946**
LIG	11.75	1.0946	0.0946	0.01	0.842	0.859	0.871	-0.020	-0.033	**1.188**	**1.311**
Late Hol.	6	1.1026	0.1026	0.03	0.894	0.852	0.860	0.050	0.040	**0.621**	**0.695**
Mid Hol.	11.3	1.0951	0.0951	0.03	0.846	0.847	0.852	0.000	-0.007	**1.003**	**1.057**
Early Hol.	11.3	1.0951	0.0951	0.03	0.858	0.847	0.853	0.013	0.006	**0.897**	**0.954**
LIG	11.75	1.0946	0.0946	0.03	0.842	0.859	0.871	-0.020	-0.033	**1.158**	**1.261**
Late Hol.	6	1.1026	0.1026	0.30	0.894	0.852	0.860	0.050	0.040	**0.875**	**0.900**
Mid Hol.	11.3	1.0951	0.0951	0.30	0.846	0.847	0.852	0.000	-0.007	**1.001**	**1.018**
Early Hol.	11.3	1.0951	0.0951	0.30	0.858	0.847	0.853	0.013	0.006	**0.967**	**0.986**
LIG	11.75	1.0946	0.0946	0.30	0.842	0.859	0.871	-0.020	-0.033	**1.050**	**1.082**

4.5 Implications for Greenland Ice Sheet Mass Balance

Regional geologic data constraining extent of the GrIS during the Holocene indicates much of the presently ice-free land in northwest Greenland deglaciated by ~10 ka (Funder et al., 2011; Corbett et al., 2015; Farnsworth et al., 2018; McFarlin et al., 2018), and the local margin of the GrIS continued to retract throughout the early and middle Holocene until at least ~4-3 ka (Corbett et al., 2015; Farnsworth et al., 2018). Oxygen isotopes in ice cores indicate that elevation of the GrIS at Camp Century dropped substantially during the early and middle Holocene despite higher accumulation rates over the GrIS (Vinther et al., 2009; Rasmussen et al., 2013), but stabilized ~3 ka (Vinther et al., 2009). Additional evidence from north and northeast Greenland also demonstrate local retraction until ~4 ka (Bennike and Weidick, 2001; Reusche et al., 2018), followed by expansion in the late Holocene (Reusche et al., 2018). GrIS growth and retreat on this sector of Greenland thus appears to strongly track summer temperature: Retraction occurs throughout the early Holocene when local summer air temperature is at least 4°C warmer than present, and continued growth occurs during only the late Holocene after summer temperatures have cooled by 4-7°C (Lasher et al., 2017; McFarlin et al., 2018).

Our reconstruction of leaf water shows that, regionally, the driest millennia occurred in the late Holocene, coincident with cold temperatures and GrIS growth, while the wettest millennia occurred in the early and middle Holocene while the GrIS retreated. In the Arctic hydrologic system, atmospheric moisture and precipitation are coupled, so that when atmospheric moisture increases, total precipitation amounts increase as well, and vice versa (Francis et al., 2009). In northern Greenland, the survival of local ice caps through the Holocene is attributed to increased precipitation during the early-middle Holocene, and our results of increased atmospheric moisture are consistent with this interpretation (Larsen et al., 2019). However, unlike ice caps, local GrIS SMB appears to have been relatively insensitive to even

these major shifts between humid and arid states. This is consistent with modeling by Buizert et al (2018), which demonstrates summer air temperature is the dominant control on GrIS SMB.

More broadly across Greenland, a model of overall surface area of the entire GrIS shows a pattern of decrease through the early and middle Holocene until an inflection ~4-3 ka when surface area begins to increase and continues to do so until the pre-industrial modern (Larsen et al., 2015; Briner et al., 2016). Ice accumulation records indicate higher precipitation over the GrIS concurrent with warmer temperatures during the early Holocene (Cuffey and Clow, 1997; Yau et al., 2016), but marginal paleohydrologic records across Greenland are largely in conflict (see Table 4.1). Accumulation records and our data indicate that broad GrIS shrinkage occurred during the wettest millennia of the Holocene in some parts of Greenland. Some ice loss was likely mitigated by this increase in precipitation, which could help explain some data-model mismatches in the middle Holocene (Lecavalier et al., 2014), but overall GrIS mass budget did not become positive until temperatures cooled in the late Holocene, even though atmospheric moisture and thus precipitation deceased substantially in some regions, including northwest Greenland.

For the LIG, we infer that atmospheric moisture prior to peak warmth was very similar to that of the early and middle Holocene, as evidenced by leaf water and lake water in near isotopic agreement. We note that there are significant environmental changes that occur at WLL during peak warmth: the presently-extralimital thermophilous-insect *Chaoborus* migrates to northwest Greenland (McFarlin et al., 2018), sedimentary $C_{23} >> C_{27}$ and C_{29}, and a major shift occurs in the C isotopic composition of *n*-alkanes, especially C_{21} and C_{23}. The totality of biomarker evidence suggests a significant increase in aquatic production within the lake and/or expansion of boggy conditions with increased terrestrial mosses and other nonvascular plants in the surrounding watershed (Nott et al., 2000; Nichols et al., 2010). Summer temperature in north

Greenland during this time is warmer than the warmest millennia of the Holocene (McFarlin et al., 2018; Dahl-Jensen et al., 2013). Although we cannot quantitatively reconstruct relative humidity during peak LIG warmth because the source of sedimentary waxes are likely from a mix of aquatic and terrestrial vegetation, we infer that summer environmental conditions at WLL through this period were likely very wet because of the expansion of aquatic indicators in our core material. This is in contradiction to some ice sheet models that demonstrate substantial retreat in northern Greenland in the LIG, in part due to aridity (Born and Nisancioglu, 2012; Stone et al., 2013).

These findings should be considered in discussions on how to model both the climate and GrIS of the LIG, particular in northwest Greenland. However, if results from WLL through the Holocene provide a lesson, it is that increasing atmospheric moisture in northwest Greenland is unlikely to majorly offset retraction of the GrIS margin driven by high summer temperatures. These results provide geologic validation of GrIS models that demonstrate a warming Arctic will ultimately drive mass loss of the GrIS. Although atmospheric moisture increased in the Arctic with warmer temperatures, results here indicate that the major lever on GrIS mass balance in northern Greenland in the past was summer melt. This has major implications for the GrIS under ongoing Arctic warming: while increased atmospheric moisture is likely, and some GrIS loss may be mitigated, it is unlikely that increased precipitation will strongly counter summer melt.

4.6 Materials and Methods

Age-Depth Model

The age-depth model for WLL Holocene-aged sediment was created using R Cran package rBacon (Blaauw and Christen, 2011) with default parameters, using 8 ^{14}C ages reported in McFarlin et al. (2018).

Sedimentary Waxes Concentration, and Hydrogen and Carbon Isotopic Composition

Sediment cores were refrigerated at 4°C for ~1 year prior to subsampling for biomarker analyses. Lipids were extracted from 0.5-3 g of lyophilized sediment using a MARS Microwave Extractor™ in 9:1 DCM: MeOH. The extraction program included a 5-minute ramp to 100°C, 20-minutes at 100°C, and a minimum of 30-minute cool down period. Total lipid extracts (TLE) were filtered and saponified in 0.5 NaOH for 8-12 hours, then acidified and separated from aqueous materials using Methyl-Tert-Butyl ether (MTBE) 3x using 10 ml MTBE each time. Total lipid extracts were then separated into fractions (alkanes, alcohols, acids) using Discovery amino-propyl solid phase extraction (SPE) columns and 6 ml Hexane, 7 ml 9:1 DCM: Acetone, 8 ml 2.5% formate in DCM respectively. Saturated alkanes were separated from unsaturated alkanes using Ag-ion SPE columns and 6 ml Hexane.

Alkanes were quantified by via gas chromatography using a Thermo Scientific Trace 1310 gas chromatograph (GC) with a ZB5 30m x 0.25 mm ID x 0.25 μm film thickness (Zebron) column coupled to Flame Ionization Detector (FID) and a Thermo DSQ single quadrupole mass spectrometer. The GC program used for quantification ramped oven temperatures from 100°C to 330°C over ~45 minutes. Alkanes were identified via diagnostic mass spectra, comparison to the NIST library, and retention times relative to laboratory standard compounds. Concentrations were calculated from peak areas through comparison to that of a 10 μg palmitic acid isobutyl ester (PAIBE) internal standard in every sample.

Compound specific carbon ($^{13}C/^{12}C$) and hydrogen ($^{2}H/H$) isotope analyses were conducted via GC isotope ratio mass-spectrometry (GC-IRMS) using a Thermo Scientific Trace GC with a ZB5-5MS 30m x 0.25 mm ID x 1 μm film thickness column coupled to a Thermo

Delta V Plus IRMS via a pyrolysis (P) or combustion (C) interface and controlled by a Thermo GC-C III and Isodat. Reactions for GC-P-CSIA occurred in an alumina column at 1420°C with a flow of 1.4 mL/min. Reactions for GC-C-CSIA occurred in an oxidizing reactor consisting of Cu/Ni/Pt at 940°C. Tank calibration to the VSMOW and VPDB scales utilized a C_{16}-C_{30} *n*-alkane standard (A6, Arndt Schimmelmann, Indiana University) and a derivatized C_{14}-C_{20} fatty acid standard (F8, Alex Sessions, Caltech). Instrumental error was assessed via root mean standard error (RMSE) on F8, which was run in duplicate between every ~4 sample duplicates and averages < 5‰ (alkanes). The H_3^+ factor was determined and applied regularly and ranged from 3.7 to 5.8 ppm/nA during the analytical period. For each sample, the alkane fractions were measured in duplicate for ^{2}H/H-isotope analyses and for ^{13}C/^{12}C-isotope analyses. Compound-specific δ^2H and δ^{13}C values are reported as average duplicate values on the VSMOW and VPDB scale respectively. Total analytical error presented on δ^2H and δ^{13}C values includes the 1σ of measurements on each compound peak as well as the instrumental error over the course of all sample measurements, propagated using the root sum of squares (RSS).

Correction of O and H raw isotope values to water values

The δ^2H-values of C_{29} *n*-alkanes are converted to leaf water values using the regression between C_{29} and summer precipitation on Greenland demonstrated in Chapter 2, with 1σ error on this estimate ~12‰.

The δ^{18}O-values of chironomid head capsules are converted to lake water values using the regression from van Hardenbroek et al. (2018), with 1σ error on this estimate of ~2.3‰. Lake water hydrogen is calculated from oxygen using both the GMWL and a local evaporation

line, which is estimated from lake water values from the Thule region, as upper and lower bounds.

$$\delta^2H = (8*\delta^{18}O)+10$$

$$\delta^2H = (5.5*\delta^{18}O)-45$$

Modern meteoric water values for this region are estimated using the Online Isotopes of Precipitation Calculator (Bowen and Revenaugh, 2003; Bowen, 2018) and compared to observed isotopes of precipitation in Thule (IAEA/WMO, 2017).

Leaf Wax Transpiration Model to estimate changes in relative humidity

We assume that the isotopic composition of lake water is representative of summer precipitation, and that average precipitation for each time slice is in equilibrium with vapor, so that the difference between vapor and precipitation is equal to the fractionation factor under equilibrium conditions. We use Farquhar et al. (2007) Equation 6 to model transpirative enrichment of leaf water:

$$\Delta_e = (\varepsilon^* + \varepsilon_k)(1-h)$$

$$R = (\delta^2H_{VSMOW}/1000)+1$$

where Δ_e is transpirative enrichment at the site of evaporation, calculated here from R_{lake} and R_{leaf}, ε^* is the temperature-dependent equilibrium fractionation factor between liquid and vapor calculated using Horita and Wesolowski (1994) and using chironomid-inferred summer air temperatures at WLL (Horita and Wesolowski, 1994; McFarlin et al., 2018), ε_k is the kinetic fractionation factor between liquid and vapor estimated by Cappa et al. (2003) as 0.03 and

modelled here using a range from 0.01 to 0.3 (Cappa et al., 2003), and h is relative humidity. Estimates used to calculate each time slice use the average values for all proxy samples within each time slice that meet quality control (i.e. C_{29} values are only used where the concentration of $C_{23} < C_{27}$ and C_{29}).

4.7 Acknowledgements

Collaborators on this work include Yarrow Axford, Magdalena Osburn, Andy Masterson, and Everett Lasher. Additional recognition for assistance is given to Hannah Dion-Kirschner, Jordan Todes, and Sohyun Lee for assistance in the laboratory; Alex Taylor, Lauren Farnsworth, Maggie Jackson, and Gordon Bromley for assistance with fieldwork; Polar Field Services, Inc., Air Greenland, the US Air Force and the US Air National Guard for logistical support. This work was supported by the NSF Polar Programs Award #1454734 and 1108306 to YA, NSF GRF to JM, NSF Geography and Spatial Sciences DDRI Award #1634118 to YA, JM, MO; ISEN to YA, MO; and a Geological Society of America graduate student research grant to JM.

Chapter 5

H and O Isotopic evidence for a consistently wet Holocene at Pincushion Lake, south Greenland

5.1 Abstract

Geologic evidence indicates that south Greenland was one of the first regions to deglaciate on the island following the Last Glacial Maximum, with ice-free regions as early as 14 cal kyr BP before the onset of Holocene warming (Björck et al., 2002; Funder et al., 2011). The climatic conditions that drove GrIS retraction in south Greenland are unclear, and there is contradicting evidence for both delayed and attenuated warmth in the Holocene relative to other regions of Greenland (Kaufman et al., 2004; Gajewski, 2015) and for strong, early Holocene warmth (Andresen et al., 2004; Wooller et al., 2004; Vinther et al., 2009; Massa et al., 2012; Briner et al., 2016). There are similar contradictions in the literature on hydroclimate of south Greenland, with evidence for a dry early Holocene and wet late Holocene, and competing evidence for a wet early Holocene and a dry late Holocene from the same region. Here, we present evidence from paired observations of the H isotopic composition of sedimentary leaf waxes and the O isotopic composition of chironomid head capsules for maximum warmth in the early Holocene followed by a cooling trend into the late Holocene, with the magnitude of change in the isotopic composition of water similar to that seen in O isotopes of ice cores from the central sector of the GrIS. We observe a consistently wet climate throughout the Holocene in south Greenland, with no major periods of aridity observed.

5.2 Introduction

Observations of modern and past ice volume indicate that the southern sector of the Greenland Ice Sheet (sGrIS) is highly responsive to changes in climate (Weidick et al., 2004; Kjeldsen et al., 2015; Larsen et al., 2016). Today, the sGrIS is definitively losing mass, particularly from the land-terminating Qassimiut Lobe and from southeastern marine terminating glaciers (Kjeldsen et al., 2015). Geologic evidence indicates that southern Greenland was the first region of the island to deglaciate following the Last Glacial Maximum (LGM)(Bennike and Björck, 2002; Andresen et al., 2004; Funder et al., 2011), and the sGrIS at the DYE 3 core site underwent greater thinning in the early and middle Holocene than the central and north-central sectors (Vinther et al., 2009; Larsen et al., 2017).

However, despite evidence for a strong sGrIS response to broad Arctic warming in the Holocene, little is known about the magnitude of past climate change that drove the retreat of ice there: very few records of past temperature or past precipitation that span the Holocene exist from this region, and among those that exist there is no consensus on the magnitude or the timing of change. Some paleoclimate records, for example, express attenuated and/or delayed Holocene warmth in this region, with a long-term warming trend and maximum temperatures achieved as late as ~4 cal kyr BP, perhaps due to downstream effects of the residual Laurentide Ice Sheet (Kaufman et al., 2004; Gajewski, 2015). Other records indicate an early Holocene Thermal Maximum (HTM), with peak temperatures as early as ~9 cal kyr BP and warmth persisting for 2-3 kyr, followed by a long-term cooling trend (Wooller et al., 2004; Frechette and de Vernal, 2009; Briner et al., 2016). Studies that assess changes in precipitation in southern and southeastern Greenland have also presented contrasting evidence, with interpretations for both drier and wetter conditions in the region at the same time (Andresen et al., 2004; Massa et al., 2012; Balascio et al., 2013). This ambiguity inhibits assessment of the sensitivity of the sGrIS to

climate change, thereby limiting the ability of the scientific community to predict the rate at which future ice loss, and the resultant global sea level rise, will occur.

Ice surface mass balance (SMB) of land-terminating glaciers is broadly controlled by summer air temperature and annual snowfall totals, which drive ice melt and accumulation respectively (Helsen et al., 2013; Vernon et al., 2013; Kjeldsen et al., 2015). Outlining if (and how) features of the hydrologic system (collectively referred to here as "hydroclimate") changed in this region through the Holocene will inform models of SMB on parts of the sGrIS, including the dynamic Qassimiut Lobe. This chapter aims to assess changes in relative humidity in southern Greenland over the Holocene by comparing the H isotopes of leaf waxes, a proxy for the isotopes of leaf water (precipitation modified by evapotranspiration) (Sachse et al, 2012), to O isotopes of chironomid, a proxy for the isotopes of lake water (van Hardenbroek et al, 2018) in the same lacustrine archive. It is currently unclear if changes in hydroclimate mitigated or exacerbated ice loss of the sGrIS during the Holocene. Our approach provides a method for identifying periods of low relative humidity, and thus aridity, via isotopically enriched leaf water relative to lake water that indicates high evapotranspiration.

We use the hydrogen isotope ratios (δ^2H values relative to VSMOW) of sedimentary long-chain *n*-alkanes ($>C_{25}$) to estimate the isotopic composition of past leaf water. These compounds are components of the waxy coating on the surface of terrestrial plant leaves (Eglinton and Hamilton, 1967). The hydrogen isotopic composition of plant wax is a function of the isotopic composition of the leaf water and the organic H incorporated into the wax during biosynthesis. The fractionation effect of wax biosynthesis is relatively predictable, particularly for C_{29} *n*-alkanes (Sachse et al., 2012). These compounds are stable over geologic timescales (Sessions, 2016), so the isotopic composition of leaf water can be estimated from the isotopic composition of sedimentary C_{29} *n*-alkanes by correcting for biosynthetic fractionation. Numerous

modern lake transects across multiple continents have demonstrated a strong relationship between the H isotopic composition of leaf waxes and precipitation (Huang et al., 2004; Sachse et al., 2004; Hou et al., 2007; Polissar and Freeman, 2010; Garcin et al., 2012; Sachse et al., 2012; Berke et al., 2019), particularly in non-arid regions (Feakins and Sessions, 2010; Shanahan et al., 2013), indicating that soil water largely tracks precipitation, and leaf water at the time of wax synthesis in the early growth season (Tipple et al, 2013) undergoes little modification by transpiration in non-arid regions. In arid regions plants undergo higher rates of evapotranspiration than non-arid regions, which isotopically enriches leaf water, and resultant waxes, relative to soil water and precipitation (Farquhar et al., 2007).

To date there are very few published hydroclimate reconstructions on Greenland (Alley et al., 1993; Björck et al., 2002; Anderson and Leng, 2004; Andresen et al., 2004; Aebly and Fritz, 2009; Massa et al., 2012; Balascio et al., 2013; Sundqvist et al., 2014; Briner et al., 2016; Thomas et al., 2016; Thomas et al., 2018), and prior to this dissertation, there were just three records of δ^2H values of sedimentary plant waxes from Greenland in the literature, (Balascio et al., 2013; Thomas et al., 2016; Thomas et al., 2018). These three records rely on the comparison between δ^2H values of mid-chain compounds to those of long-chain compounds to assess changes in moisture balance. Although we report δ^2H values of all wax compounds, including those of mid-chains, we do not attempt to interpret them in this chapter due to uncertainty in biological source and, therefore, water source. Our prior work has shown that although mid-chain wax compounds are commonly ascribed to aquatic plants (K.J. Ficken et al., 2000; Liu and Liu, 2016), the isotopic composition of mid-chain waxes does not strongly correlate to lake water on Greenland; this is particularly true when the concentration of long-chain compounds strongly outweighs mid-chain compounds in sediments (see Chapter 2)(Dion-Kirschner et al., 2017; J. McFarlin et al., 2018). To reconstruct past lake water isotopes, we therefore instead use the

oxygen isotopes of chironomids from Pincushion Lake, a proxy shown to accurately reflect the O isotopic composition of lake water (Chipman et al, 2018).

5.3 Site Description and Methods

Site Description

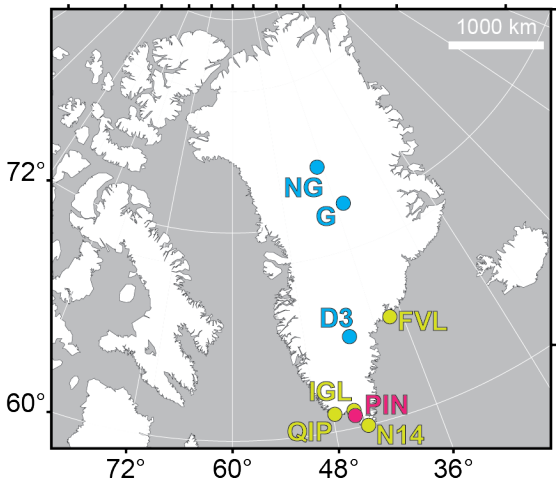

Figure 5.1 Map of Greenland showing location of field site, and important other field sites discussed in text. PIN = Pincushion Lake, IGL = Igaliku Lake, QIP = Qipisarqo Lake, N14 = Lake N14, FVL = Flower Valley Lake, D3= Dye-3,, G = GRIP, NG = NGRIP

Pincushion Lake (60.7°N, 45.41°W) is a small (<15 m deep, <0.1 km^2) nonglacial lake located in the Narsaq region of south Greenland (Figure 5.1). The lake sits ~450 m above sea level, well above the marine limit (Woodroffe et al., 2014), and is ~35 km inland from the Labrador Sea and <2 km from the nearest fjord. The lake is currently through-flowing in the late summer, although there is no surface inlet feeding the lake so lake levels are maintained by precipitation and possibly groundwater. This coastal site receives ample precipitation year round, with the annual average precipitation total ~860 mm/year, delivered relatively evenly throughout the year (60% of precipitation falls in the summer and fall, while 40% falls in the winter and spring) (Cappelen et al., 2001). In this region, the modeled modern isotopic composition of precipitation ranges from ~ -85‰ in the summer to -115‰ in the winter, with amount-weighted mean annual values ~ -94‰

(Bowen and Revenaugh, 2003; Bowen, 2018). Modern lake water at Pincushion is isotopically near-identical to modeled mean annual precipitation, with δ^2H values ~ -98‰.

This region of Greenland is classified as having a low to sub-Arctic climate, and sits within the sporadic permafrost zone (Jensen and Christensen, 2003). Average air temperatures range from ~9°C in the summer to ~ -6°C in the winter, with annual average air temperature ~1°C (Cappelen et al., 2001). Vegetation of the region is classified as low Arctic oceanic, dominated by heath and scrub, characteristic of southern coastal regions with heavy winter snow cover (Jensen and Christensen, 2003)

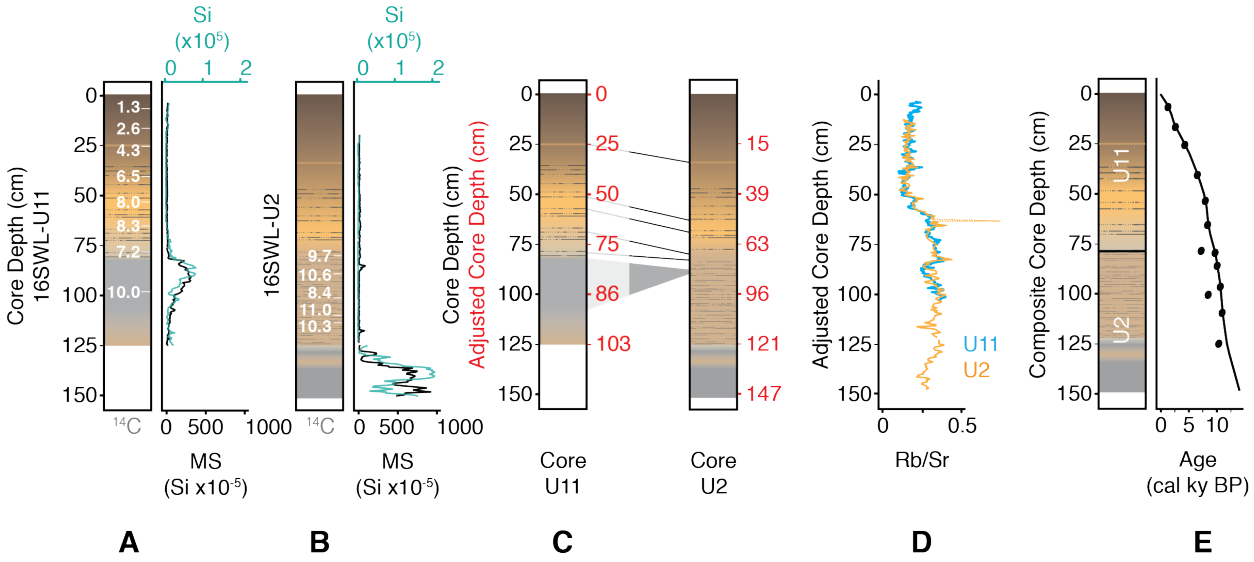

Figure 5.2 *Stratigraphy of cores 16SWL-U11 and 16SWL-U2 from Pincushion Lake. A) Core U11 and B) Core U2, with radiocarbon ages overlying sediment, Magnetic Susceptibility (black line) and Si-content (blue line), C) Diagram showing correlation points between core U11 and core U2 used to create an adjusted core depth, D) Rb/Sr ratios of U11 (blue line) and U2 (orange line) demonstrating agreement between these two measurements when mapped using the adjusted core depth, and E) and age-model using radiocarbon ages and adjusted core depth for the resultant composite core*

Multiple sediment cores were obtained using an open-bore percussion coring system (Universal Corer) from Pincushion Lake in 2016. Two cores, 16SWL-U11 and 16SWL-U2, 125 and 150 cm long respectively, are used in this study. Cores are composed of organic-poor fine-grained sediment followed by laminated organic-rich gyttja containing macrophytes (Figure 5.2). Split cores were scanned using a non-destructive GeoTek Multi-Sensor Core Logger (MSCL-S), with a Bartington MS3 meter and MS2E sensor using a 10-second pulse for Magnetic Susceptibility (MS), and an Olympus Delta Pro Innov-X handheld X-ray fluorescence (XRF) spectrometer using a 20-second pulse for elemental composition. MS and XRF measurements were made every 0.5 cm over the length of each core.

Geochronology

Aquatic mosses, terrestrial plant material, and miscellaneous organic material (e.g. insect chitin) picked from bulk sediments were used for radiocarbon dating throughout both cores. These samples were collected into ashed-glass vials, dried at low-temperature (~55°C), and sent to the Woods Hole Oceanographic Institute-National Ocean Sciences Accelerator Mass Spectrometry facility for radiocarbon analysis. ^{14}C-ages were calibrated to calendar years before present (cal yr BP) using CALIB html version 7.1 (Stuiver et al., 2017) and the IntCal13 calibration curve (Reimer et al., 2013). Median ages are used to represent a single age for each sampling location. A living aquatic plant was also sampled for radiocarbon analysis, and yielded a post-bomb ("modern") age. To create a single composite core using both U11 and U2, 7 stratigraphic markers were used to correlate cores.

Compound-Specific Geochemical Analyses

Plant Waxes Lipids were extracted from 0.5-3g lyophilized sediment aliquots sampled every ~5 cm along the length of the composite core using a MARS microwave Extractor™ in 9:1 DCM: MeOH. The extraction program was as follows: 5-minute ramp to 100°C, 20-minute hold at 100°C, and a 30-minute cool-down to room temperature. Total lipid extracts (TLEs) were filtered from sediments using 100 μm ashed-glass filters under slight vacuum with DCM. TLEs were dried-down and saponified in 0.5 M NaOH for 8-12 hours, then acidified in 1 M HCl. Lipids were extracted out of hydrolysates using 10 ml of Methyl-Tert-Butyl ether (MTBE) in triplicate. TLEs were then separated into fractions using Discovery™ amino-propyl solid-phase extraction (SPE) columns and 6 ml Hexane for alkanes, 7 ml 9:1 DCM and Acetone for alcohols, and 8 ml 2.5% formic acid in DCM for acids. Unsaturated alkanes were removed from the alkane fraction using Ag-ion SPE columns and 6 ml Hexane.

The alkane fraction was analyzed using a Thermo Scientific Trace 1310 gas chromatograph (GC) with a Zebron ZB5 column (30m x 0.25 mm ID x 0.25 μm film thickness) linked to a flame-ionizing detector (FID) for quantification and a Thermo ISQ single quadrupole mass spectrometer (MS) for compound identification. All compound peaks were identified via mass spectra, retention times relative to alkane standards, and comparison against the NIST Library. The concentration of each compound peak was calculated from peak area relative to an internal standard of 10 μg of palmitic acid isobutyl ester (PAIBE), added just prior to quantification.

Compound-specific hydrogen isotope analyses (CSIA) were completed on a Thermo Trace GC with a Zebron ZB5-5MS column (30m x 0.25 mm ID x 1 μm film thickness) coupled to a Delta V PLUS isotope ratio mass spectrometer (IRMS) via a pyrolysis (P) interface at 1400 °C with a carrier flow of 1.4 mL/min. Tank calibration to the VSMOW scale utilized a C_{16}-C_{30} *n*-

alkane standard (A6, Arndt Schimmelmann, Indiana University) and a derivatized C_{14}-C_{20} fatty acid standard (F8, Alex Sessions, Caltech). Instrumental error was assessed via root mean standard error (RMSE) on A6, which was run in duplicate between every ~3 sample duplicates and averages ~5‰. The H_3^+ factor was determined and applied daily and ranged from 3.36 to 4.16 ppm/nA during the analytical period. For each downcore sample, the alkane fractions were measured for CSIA in duplicate. Hydrogen isotope values are reported in permil as average duplicate values on the VSMOW scale respectively. Total analytical error presented on δ^2H values includes the 1σ of measurements on each compound peak as well as the instrumental error over the course of all sample measurements, propagated using the root sum of squares (RSS).

The δ^2H values of leaf water were calculated from δ^2H_{C29} using five different relationships: four linear models using mean annual and summer precipitation (two using Greenland-only data, and two using global data), and via correction with the average global apparent fraction value (ε_{app}) of -119‰ (see Chapter 2).

Chironomids Chironomid analyses were performed by Chipman et al (2018): head capsules were isolated manually from sediments and treated for isotope analysis following standard protocols reported in van Hardenbroek et al (2018). The isotopic composition of lake water is calculated from $\delta^{18}O_{chironomid}$, reported in ‰ relative to VSMOW, using the regression $\delta^{18}O_{chironomid} = 0.89*\delta^{18}O_{lake\ water} + 22.5$ reported by van Hardenbroek et al (2018). Although using just the intercept of the regression (i.e. a correction of 22.5‰) from compiled modern data to infer $\delta^{18}O$-values of lake water from those of chironomid is more common in the literature (Lasher et al., 2017; Lasher and Axford, 2019), we use the values of lake water calculated from the van Hardenbroek et al. (2018) linear model to interpret the water isotope trends in lake water

in comparison to the water isotope trends of leaf waxes. We opt for the linear model to be consistent with our utilization of a regression to calculate δ^2H values of leaf water from δ^2H values of sedimentary C_{29} waxes, and because using the linear model takes into account the slope and position of the line, given that for this regression the slope is <1 and the line does not pass through the origin (van Hardenbroek et al., 2018). The error on calculated $\delta^{18}O_{lake\ water}$ reported here is the root-square mean error on the regression ($\delta^{18}O_{error} \pm 2.3‰$) calculated from van Hardenbroek et al (2018) data. To allow direct comparison with leaf waxes, corresponding δ^2H values for lake water were calculated from reconstructed $\delta^{18}O_{lake\ water}$ using the global meteoric water line (GMWL, $\delta^2H_{precipitation} = 8*\delta^{18}O_{precipitation} +10$)(Gat, 1996). Error on these calculated lake water δ^2H values is estimated by multiplying $\delta^{18}O_{error}$ by 8.

Samples for leaf waxes were taken from the same sampling depth in the composite core as a subset of samples for oxygen isotopes (which were sampled at higher resolution than leaf waxes). Both methods integrate ~1 cm of core depth for each sample, representing ~100-200 years/sample.

5.4 Results

Stratigraphy and Geochronology

The sedimentologic structure of the core yielded insight into shifting inputs through time at Pincushion Lake. Elemental composition, MS data, and radiocarbon ages for Pincushion Lake were first analyzed and reported by Chipman et al (2018). Here we restate relevant sections of that work: MS and Si-content are highest in the lower unit of each core, with an abrupt shift to near zero values throughout the uppermost ~75 cm (U11) to ~125 cm (U2) of the record. The abrupt decrease in MS and Si-content is attributed to a decrease in clastic material relative to

organic content, which can be visualized as a transition from mostly gray fine-grained sediment in the base of the cores to brown organic-rich gyttja. Core U11 differs from core U2 in that the basal-most sediments are organic-rich and transition into a package of fine-grained sediment with relatively high MS and Si-content values ~100 cm, followed by an abrupt shift to organic-rich gyttja at ~75 cm. Core U2 lacks the basal-most organic-rich material, and basal material is instead a fine-grained package of sediments, which is followed by an abrupt shift to organic-rich sediment ~125 cm. The location of the transition from fine-grained sediment to gyttja is thus inconsistent across the two cores, with the boundary in core U11 ~50 cm higher in core depth than the boundary in core U2. Radiocarbon-ages support non-synchronous timing of this transition, with the transition in core U11 bracketed by radiocarbon ages between ~7 cal kyr BP and ~10 cal kyr BP, whereas the transition in core U2 is >10 cal kyr BP. We note a small, abrupt rise in MS and Si-content in core U2 that aligns with the fine-grained sediment package in U11, suggesting that this same package is recorded in core U2 but in a much-reduced manner. This indicates that the fine-grained package in core U11 is likely the result of a slump in that region of the basin, with ~25 cm of core material deposited in that slump, as opposed to continuous input during deglaciation of the region.

Radiocarbon ages of sedimentary material in Pincushion Lake range from ~1.2 to ~11 cal kyr BP. The “modern” radiocarbon age of the (then-living) plant collected in 2016 provides evidence that there is little influence from the hardwater effect on the age of C in this watershed, and therefore radiocarbon ages of aquatic materials provide a valid foundation for an age-depth model. To create an age model for a composite core, combining core U11 and core U2, seven sediment markers were used to correlate the two cores, including visually distinct laminations and the MS and Si-content measurements attributed to the above-discussed slump. On the resulting composite core, the R Cran package rBacon (Blaauw and Christen, 2011), with default

parameters and 14 of the 15 ^{14}C-ages, was used to create an age-depth model. Only 14 age points (from 15 ^{14}C-ages) are utilized because a single age value was derived from averaging two points sampled at the same depth that yielded almost identical ^{14}C-ages. The resultant model suggests that the basal sediments of Pincushion Lake extend to ~14 cal kyr BP, albeit there is no age control before 10.9 cal kyr BP, and the age model assumes near-steady sedimentation rates below that age. Thus, this is interpreted as a bracketing age, with the age of basal sediments at least ~11 cal kyr BP and probably at most 14 cal kyr BP.

The fine-grained package at the bottom of core U2 is likely derived from an influx of clastic material delivered via ice melt. This material, and radiocarbon ages that indicate these sediments are >11 cal kyr BP, support that the recovered record extends through the entire Holocene, with the basal unit likely deposited during deglaciation around the onset of the Holocene. Radiocarbon ages place the onset of sedimentation (and thus deglaciation) in this watershed >11 cal kyr BP, at the end of the Younger Dryas cold period. This timing is further supported by ^{10}Be-ages from glacial erratics and exposed bedrock collected in the Pincushion watershed which date to ~12 cal kyr BP (Pers. Comm. G. Sinclair). These ages are early compared to most other regions of Greenland (e.g. Funder et al, 2011), but generally consistent with prior observations that indicate the earliest region on the island to deglaciate post-LGM was southern Greenland, with some ice-free land as early as ~14 cal kyr BP (Bennike et al., 2002; Andresen et al., 2004; Funder et al., 2011).

Compound-specific geochemical analyses

Plant Wax Concentration Long-chain sedimentary *n*-alkanes are used here as representative of plant lipids, with C_{21}-C_{33} identified in Pincushion Lake sediments. Of these compounds, C_{29} and C_{31} are the most abundant sedimentary waxes, except in the basal fine-

grained package where C_{23} and C_{25} dominate. The absolute concentration of individual compounds ranges from <1 to ~100 μg/g dry sediment. However, absolute concentration data demonstrates concerning differences between extraction batches, with one round of samples (representing ~50% of this record) yielding 4-5x the concentration of lipids relative to the other batch, unrelated to core depth. Although we cannot pinpoint the exact cause of the difference between extraction batches, we caution against interpretation of absolute values of concentration data in this record. Instead, we discuss relative concentration data, because the proportion of compounds in a given sample, relative to the other compounds in that sample, should be maintained regardless of the overall efficacy of the extraction.

The distribution of *n*-alkanes in Pincushion Lake is initially dominated by mid-chain compounds at the base of the core ~12 to 11 cal kyr BP, but quickly shifts toward long-chain compounds ~11 cal kyr BP. From ~10 to 0 cal kyr BP, the distribution of compounds is dominated by C_{29} and C_{31} waxes, with a stable ratio of C_{23}:C_{29} ~0.4. A low ratio of C_{23}:C_{29} indicates that the source of sedimentary waxes is predominantly terrestrial plants (Eglinton and Hamilton, 1967; K. J. Ficken et al., 2000; Liu and Liu, 2016; Berke et al., 2019). At ~10 cal kyr BP, where the ratio of C_{23}:C_{29} drops to values <1, we interpret this as a change in the dominant source of sedimentary waxes from aquatic and nonvascular plants (and an absence of higher vegetation on the landscape) to vascular land plants. We hypothesize that terrestrial vegetation colonized the region ~10 cal kyr BP, which drove the change in C_{23}:C_{29} ratios, and sedimentary waxes are largely derived from terrestrial plants for the remainder of the Holocene until present day.

Hydrogen Isotopes The hydrogen isotopic composition of sedimentary plant waxes is notably stable through this record. The range of δ^2H values from Pincushion Lake waxes is relatively small in comparison to other records from Greenland discussed in this dissertation,

averaging ~ -200 ± 25‰. The largest variations in δ^2H values occur in the [lower most] fine-grained sediments, synchronous with ratios of C_{23}:C_{29} >1. Of all the compounds, C_{29} and C_{31}

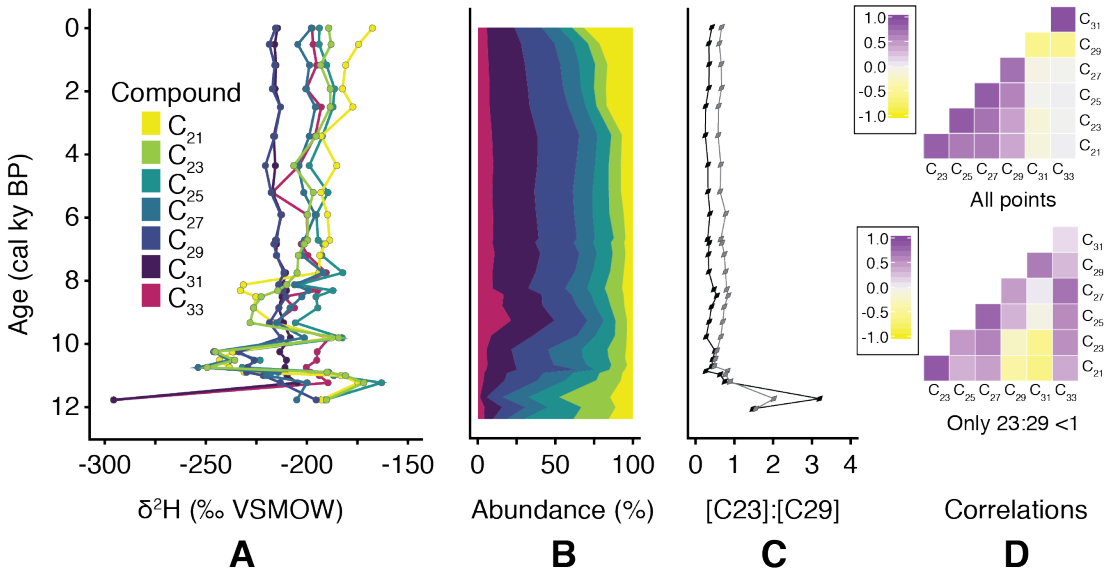

Figure 5.3 *Geochemical profile of the composite core plotted by age with A) δ^2H-values of sedimentary plant wax compounds (odd-chain C_{21}-C_{33} n-alkanes), B) the relative abundance of sedimentary plant wax compounds along the length of the core, C) the ratio of C_{23}:C_{29} n-alkanes (black line) and C_{23}:C_{27} n-alkanes (gray line), and D) correlation matrices comparing the δ^2H-values of sedimentary plant wax compounds when all points are included (upper row) and when only points with C_{23}:C_{29} ratios <1 (lower row)*

have the most stable δ^2H values over the Holocene, particularly from ~10-0 cal kyr BP, whereas all other sedimentary plant waxes show mild ^2H-enrichment through the same time period. The δ^2H values of C_{31} and C_{33} are strongly correlated to each other but uncorrelated to C_{21}-C_{29}, which are themselves strongly correlated. However, there are large isotopic trends in the basal fine-grained package, particularly in C_{31} and C_{33}, when the source vegetation is likely distinct from the rest of the Holocene thereby influencing which compounds appear to be highly correlated in

the record. When points from the basal unit are removed, so that correlation is assessed only where C_{23}:C_{29} ratios are <1, (i.e., only for the period after we infer high abundance of vascular land plants), different trends emerge: C_{29} and C_{31} are strongly correlated, but have weaker relationships to other compounds.

We use C_{29} *n*-alkanes to calculate δ^2H values of terrestrial leaf water from those of sedimentary waxes for the Holocene, because well-calibrated wax-water relationships have been established for C_{29} *n*-alkanes both in Greenland (see Chapter 2) and globally (Sachse et al., 2012), and because they are isotopically correlated in this record with the definitively terrestrial compound C_{31} (Liu et al., 2015). We model terrestrial leaf water using four different linear models (two are Greenland-specific, two use global observations), as well as by applying a constant ε_{app}, to test the sensitivity of the estimate to the chosen model. We find that values derived from both Greenland and global linear models of δ^2H_{C29} against the δ^2H values of average annual precipitation (δ^2H_{ANN}) are within error of each other, and agree with the modeled isotopic composition of modern annual precipitation in the region (Bowen, 2018). We find that values derived from both the Greenland and the global linear model of δ^2H_{C29} against the average δ^2H values of June, July and August (summer) precipitation (δ^2H_{JJA}) are within error of each other, and consistent with the modeled isotopic composition of modern summer precipitation in the region (Bowen, 2018). δ^2H values of leaf water calculated from δ^2H_{C29} using ε_{app} (which assumes a constant biosynthetic fractionation factor and does not assume the season of underlying source water) are within error of δ^2H values of leaf water calculated using δ^2H_{C29}-δ^2H_{ANN} linear models. Given this agreement with values calculated using ε_{app}, and because the delivery of precipitation is roughly even throughout the year, for this record we employ the estimates for leaf water calculated from δ^2H_{C29} using the Greenland-specific regression for mean

annual precipitation. From 10-0 cal kyr BP, δ^2H values of leaf water trends towards more depleted values (based on end-member averages), although the scale of this change (~10‰) is smaller than the variability expressed between samples.

Oxygen Isotopes The $\delta^{18}O$ values of sedimentary chironomid head capsules demonstrate greater variability between samples than sedimentary leaf waxes, with shifts of up to ~3‰ between adjacent samples. Like δ^2H values of leaf water, $\delta^{18}O$ values of chironomid show a slight trend towards more depleted values through the Holocene, although the magnitude of this trend is again smaller than the variability expressed between samples. The most ^{18}O-enriched average values occur ~10-8 cal kyr BP, while the most ^{18}O-depleted average values occur ~2 cal kyr BP, with the average difference between these periods ~1‰.

To estimate the $\delta^{18}O$ values of lake water from those of chironomid, we employed three different modern $\delta^{18}O_{chironomid}$-$\delta^{18}O_{lakewater}$ relationships (see Methods). The difference in modelled $\delta^{18}O$ values of lake water is up to ~2‰; this error is nontrivial, but all estimates do agree within error. We find that the average calculated δ^2H values of past lake water is ~100 ± 25‰, and thus is in close agreement with (i.e. within error of) the isotopic composition of modern lake water and average mean annual precipitation in the region for much of the record.

5.5 Discussion

There is close agreement between the isotopic composition of leaf water and that of lake water throughout this record. We find that the δ^2H values of leaf water and those of lake water are statistically indistinguishable (i.e. within error) from 10 to 0 cal kyr BP. Prior to ~10 cal kyr BP, there were large differences between lake water and leaf water, with leaf water substantially

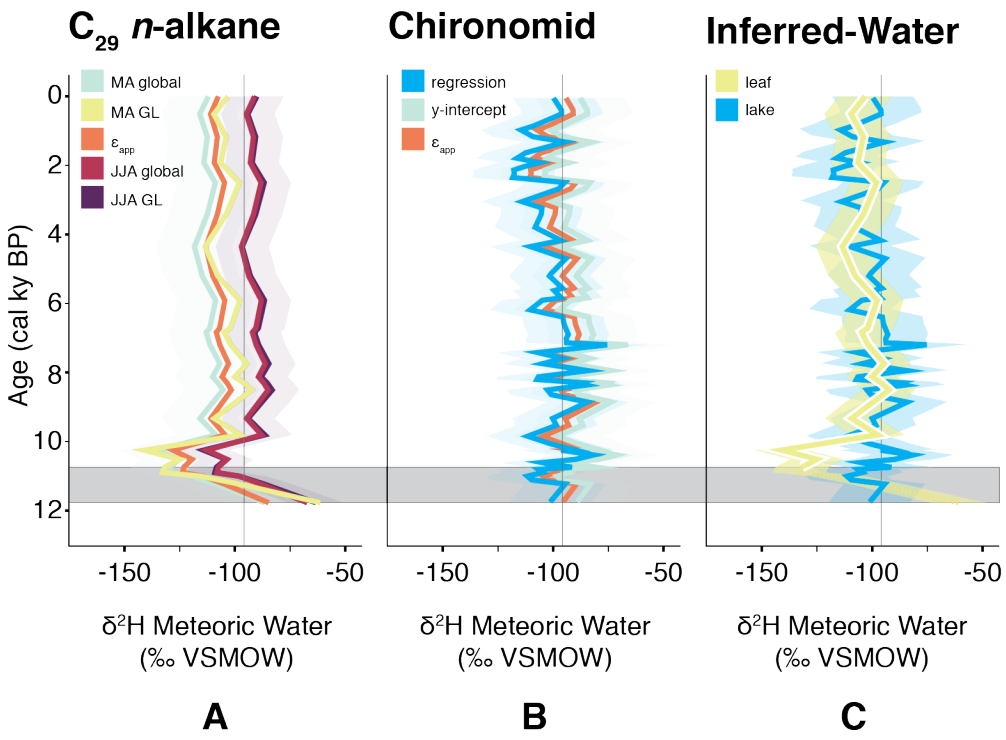

Figure 5.4 *Calculated δ^2H-values of A) leaf water from C_{29} n-alkanes and B) lake water from δ^{18}O-values of chironomid head capsules, with both A) and B) using different modelled relationships to show the range of possible values depending on the proxy-water relationship used. Shading around lines represents the root square error on the model estimate. MA = mean annual, GL = Greenland, JJA = June July August and C) calculated δ^2H-values of leaf water and lake water. Vertical gray line represents δ^2H-value of modern mean annual precipitation. Gray horizontal bar denotes where C_{23}:C_{29} >1, so C_{29} waxes are not clearly attributable to terrestrial plants and are thus not interpreted here*

^{2}H-depleted relative to lake water. This depletion appears in all sedimentary plant wax compounds except C_{31} and C_{33}. The observation that leaf water δ^2H values were more ^{2}H-

depleted than lake water values suggests that plants on the landscape from ~12-10 cal kyr BP were tapping into a more ^{2}H-depleted reservoir than the average annual isotopic composition of precipitation reflected in lake water, with hypothetical possibilities that include melting snowpack or glacial ice, or permafrost thaw following the Pleistocene-Holocene transition. Because lake water does not show this same ^{2}H-depletion from ~12-10 cal kyr BP, it is unlikely that the trends in leaf water during this period were driven by a change in the seasonality of precipitation (i.e. a shift towards strongly winter-biased precipitation, which would appear as ^{2}H-depleted source water). Following this period of depletion, leaf waters become more ^{2}H-enriched but otherwise demonstrate long-term low variability (δ^{2}H values varying <20‰).

Overall, both leaf water and lake water at Pincushion Lake show only modest changes in water isotopes from ~10-0 cal kyr BP, with a long-term trend towards more ^{2}H-depleted average values. This indicates that the moisture balance of this watershed undergoes very little long-term change throughout the Holocene: the isotopic composition of meteoric water, as inferred from the δ^{2}H values of leaf water and lake water, tracks the solar insolation curve of the Holocene, but otherwise shows little millennial-scale variability. A similar trend was observed from ~9-0 cal kyr BP in the δ^{18}O-values of chironomid head capsules at Qipisarqo Lake, ~130 km from Pincushion Lake (Wooller et al., 2004), and at NGRIP/GRIP ice core sites in $\delta^{18}O_{ice}$ (Vinther et al., 2009), both of which are interpreted as changes in annual air temperature. We hypothesize that any past prolonged periods of summer aridity would have resulted in leaf water ^{2}H-enrichment relative to lake water from enhanced transpiration, as reported elsewhere on Greenland in this dissertation. Because there are no major periods when leaf water was enriched relative to lake water, and indeed our two proxies suggest statistically indistinguishable isotopic compositions of those two waters on multi-millennial timescales throughout the entire Holocene

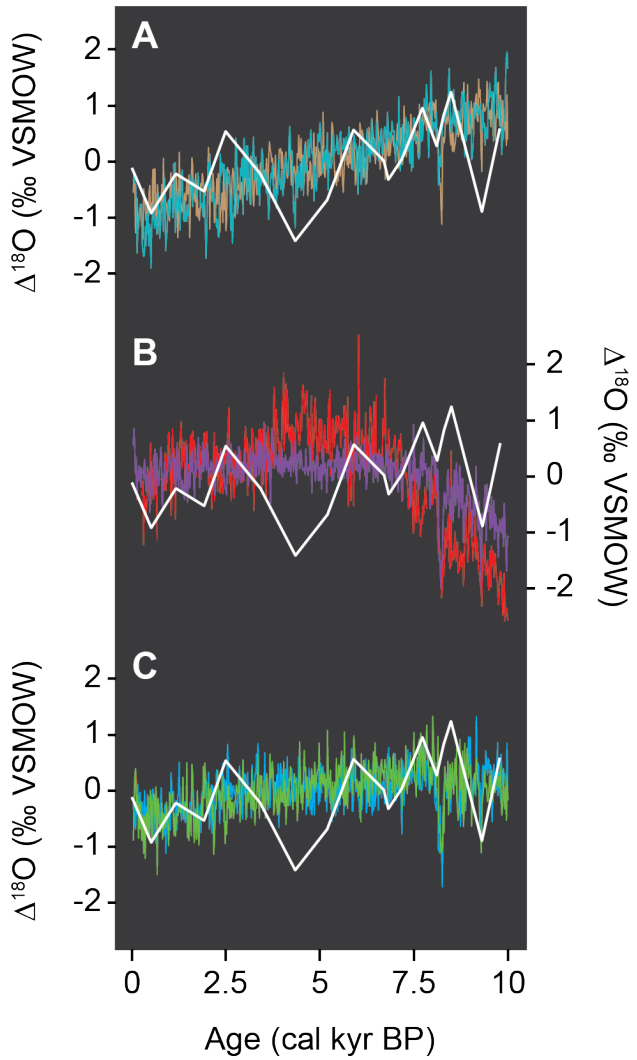

Figure 5.5 *Change in $\delta^{18}O$-values ($\Delta^{18}O = \delta^{18}O_x - \delta^{18}O_{mean}$) in ice through the Holocene from A) Renland (teal) and Agassiz (brown), B) DYE-3 (purple) and Camp Century (orange), and C) GRIP (blue) and NGRIP (green), compared against the change in $\delta^{18}O$-values of leaf waxes at Pincushion Lake (white line) calculated from $\delta^{2}H$-values leaf water using the GMWL*

after 10 cal kyr BP, we conclude that both lake water and leaf water track mean annual precipitation. In turn, this first-order trend in the isotopic composition of mean annual precipitation appears to be controlled largely by mean annual air temperature at these sites. This region, which is among the wettest in Greenland today, was consistently wet throughout the Holocene.

This conclusion is in contrast to some published records which infer distinct multi-millennial-scale changes in hydroclimate during the Holocene in the same or nearby regions (Andresen et al., 2004; Massa et al., 2012; Balascio et al., 2013; Balascio et al., 2015; Young and Briner, 2015; Thomas et al., 2016). Balascio et al. (2013) argue for aridity during the middle Holocene from ~8 to 4 cal kyr BP at Flower Valley Lake in southeast Greenland, ~650 km from Pincushion Lake, based on the deviation in $\delta^{2}H$ values between mid- and long-chain sedimentary plant waxes (Balascio et al.,

2013). Andresen et al. (2004) interpret changes in sediment composition at Lake N14, ~80 km from Pincushion Lake, as derived from changes in temperature and precipitation: they argue that clastic material and aquatic moss abundances indicate a warm and humid period from ~8-5 cal kyr BP, followed by drier and colder conditions from ~3.7 cal kyr BP to modern (Andresen et al., 2004). In contrast, Massa et al. (2012) interpret changes in sediment composition and pollen and diatom assemblages in Lake Igaliku, ~35 km from Pincushion Lake and ~120 km from Lake N14, as indicative of warm and dry conditions from ~8-5 cal kyr BP, followed by increased moisture and cooling in the region (Massa et al., 2012). In other words, nearly every possibility for hydroclimate in south Greenland has been inferred: 1) wet early Holocene relative to dry late Holocene, 2) dry early Holocene relative to wet late Holocene, and 3) presented here, no major change in moisture balance between the early and late Holocene. Our record agrees with evidence for a warm early-middle Holocene and a cool late Holocene, but does not support periods of aridity at any time in the Holocene in south Greenland. Given that our data demonstrate warming through the early Holocene and cooling in the late Holocene, it is possible that some evidence interpreted as aridity could be trends instead driven by changing temperature.

The sGrIS shows a strong response to Holocene climate change: ice at the Dye 3 site, for example, appears to have experienced some of the highest rates of elevation change on Greenland in the early Holocene (Vinther et al., 2009). More locally, land on the margin of the sGrIS demonstrates the earliest post-LGM deglaciation dates (Weidick et al., 2004; Funder et al., 2011; Carlson et al., 2014), with ice-free coastal areas as early as ~14 cal kyr BP (Björck et al., 2002; Andresen et al., 2004). Retraction of the sGrIS occurs throughout the Holocene, with maximum retreat from ~9 cal kyr BP until at least ~4 cal kyr BP, and even later for low-lying regions (Kaplan et al., 2002; Weidick et al., 2004; Larsen et al., 2011; Winsor et al., 2014; Woodroffe et al., 2014; Larsen et al., 2015; Larsen et al., 2016). Because we see no evidence for

changes in moisture balance in south Greenland, we suggest that negative SMB of the sGrIS must have been driven by insolation-driven warming and sustained higher air temperatures in the early Holocene rather than responding to changes in aridity.

We note that the $\delta^{18}O_{ice}$ at the nearest ice core site, DYE 3, shows almost no change over the Holocene from ~10-0 cal kyr BP, lacking a distinct HTM, and also lacking the long-term trend towards more ^{18}O-depleted values in the late Holocene observed in other records from Greenland ice (Vinther et al., 2009) and at Qipisarqo Lake (Wooller et al., 2004). We also do not observe agreement between leaf water or lake water at Pincushion Lake and $\delta^{18}O_{ice}$ at DYE 3; instead, the multi-millennial-scale changes in water isotopes at Pincushion Lake are similar in magnitude to the mutli-millennial-scale trends observed at NGRIP/GRIP, despite that the DYE 3 drill site is much closer. This evidence supports the idea that the $\delta^{18}O_{ice}$ of DYE 3 is not primarily tracking annual precipitation (and thus temperature) as discussed in Vinter et al. (2009), and that the temperature changes over the Holocene in southern Greenland were comparable to those in central Greenland at GRIP and NGRIP (see Figure 1.1).

5.6 Conclusions

The agreement between the $\delta^{2}H$ of leaf water and $\delta^{18}O_{ice}$ at NGRIP and GRIP, indicates that leaf water at this small lake in southern Greenland is derived from average annual precipitation, the isotopic composition of which is likely controlled by insolation-driven temperature change over the Holocene in this region (Wooller et al., 2004; Frechette and de Vernal, 2009; Vinther et al., 2009). These results indicate a relatively early deglaciation in south Greenland, followed by climate amelioration before ~10 cal kyr BP, with the amplitude of warming in south Greenland comparable to that of central Greenland. That water isotopes of leaf

water and lake water were indistinguishable at Pincushion Lake throughout the past 10 cal kyr BP indicates that the moisture balance of south Greenland did not undergo large, long-term changes. Therefore, we conclude that south Greenland has remained wet enough, on average, to prevent significant evapotranspiration of soil and leaf waters for the past 10 millennia, despite multi-millennial cooling throughout this period and some nearby evidence for hydroclimate changes. More broadly, compared to Holocene records from west (Thomas et al., 2016) and northwest Greenland (see Chapter 4), this reveals that the amplitude of warming and the direction of moisture balance across Greenland are spatiotemporally heterogeneous.

5.7 Acknowledgements

This work was funded by an NSF-CAREER award to Y. Axford (Office of Polar Programs grant 1454734); an NSF GRFP and a GSA graduate student research grant to J. McFarlin; internal Northwestern funding to M. Osburn; and an NSF GSS-DDRI award to Y. Axford, M. Osburn, J. McFarlin; H. Dion-Kirschner and S. Lee provided laboratory assistance; A. Hartz, G. Sinclair, and G. Lasher provided field assistance; A. Masterson performed all isotope measurements for O and H data; Much of this work was conducted in collaboration with M. Chipman, who developed the stratigraphic interpretation and age-depth model for Pincushion Lake, and also is responsible for the O isotope record of Pincushion Lake, which was generously shared for this chapter.

Chapter 6

Conclusions

6.1 Conclusions

When I started this dissertation work in 2013, the average pCO_2 level in the atmosphere was approaching 400 ppm. Since that time, pCO_2 has increased every year, with the current global average ~410 ppm. This places modern atmospheric pCO_2 at ~100 ppm above the highest level of pCO_2 observed in the last 800,000 years (Lüthi et al., 2008), and this trend is expected to accelerate in the coming decades (Collins et al., 2013). There is high confidence that, with this increasing atmospheric pCO_2, ongoing warming in Arctic regions will continue at an unprecedented rate, albeit the magnitude of warming, and the associated environmental changes, are uncertain on the regional scale (Collins et al., 2013). At present, one of the biggest unknowns in climate science is how and where precipitation patterns will change in response to global atmospheric reorganization driven by warming. In the Arctic, this has major implications, for vegetation (albedo) and landscape dynamics (permafrost), and for predicting the surface mass balance of parts of the Greenland Ice Sheet (Fettweis et al., 2008; Vernon et al., 2013).

Geologic archives that record components of local hydroclimate can provide useful insight into precipitation-related changes that occur in tandem with warming. In general, few proxies directly relate to past precipitation (Sundqvist et al., 2014). The hydrogen isotopic composition of sedimentary leaf waxes is emerging as one of the best tools available for reconstructing past isotopes of precipitation, but prior to this work, there were few observations to support the fidelity of this proxy in the Arctic. Chapter 2 of this dissertation presents a test for this tool in Greenland, and affirms there is a strong correlation between the H isotopic composition of many sedimentary leaf wax compounds and that of precipitation. Pairing this tool

with complimentary proxies, like chironomid species assemblages for summer air temperature (Chapter 3) and/or oxygen isotopes of aquatic chironomid larvae head capsules for lake water isotopes (Chapters 4 and 5), on appropriate archives can further elucidate how some aspects of hydroclimate change with warming.

One of the major benefits to this work is that calibration data from Chapter 2 can be used to calculate the isotopes of past water from the isotopes of leaf waxes on Greenland. This allows reconstructions from the H isotopes of leaf waxes to be interpreted as water isotope values, comparable to other water isotopes proxies, instead of as relative changes within the proxy through time.

The application of H isotopes of sedimentary leaf waxes with calibration data (Chapter 2) and a paired-proxy approach (Chapters 3, 4, 5) revealed large differences between the relatively warm early-middle Holocene and the cool late Holocene in northwest Greenland (Chapter 3). Unlike the early-middle Holocene, summer precipitation inferred from leaf wax is strongly ^{2}H-enriched in the late Holocene relative to modern summer precipitation isotope values. This trend is not observed in lake water isotopes inferred from chironomid isotopes, interpreted also as summer precipitation but without the effects of transpiration, and thus reveals a period of low relative humidity (i.e. aridity) in the late Holocene that drove high rates of transpiration during the growth season (Chapter 4). In contrast, this same comparison between leaf water and lake water isotopes in south Greenland revealed a consistently wet climate throughout the Holocene (Chapter 5). The spatial heterogeneity in early Holocene hydroclimate of Greenland could be tied to the extent of sea ice in the Baffin Bay, or to changes in the distal transportation of moisture to these regions related to atmospheric and oceanic circulation patterns.

This work contributes to greater regional understanding of changes in precipitation patterns across Greenland associated with insolation-driven warming and indicates future

changes in precipitation will likely be heterogeneous across the island. In at least the northwest and south Greenland, periods of relative warmth are coupled to relatively wet conditions. This suggests that ongoing and future warming of these regions will be accompanied by an increase in atmospheric moisture, but the contribution of higher precipitation over the island is unlikely to surmount temperature-driven mass loss of the Greenland Ice Sheet.

6.2 Future Directions

In evaluating sedimentary wax compounds both on modern Greenland (Chapter 2) and in downcore archives from Greenland (Chapters 4, 5), it became apparent that mid-chain wax compounds on Greenland, commonly ascribed to aquatic plants and mosses (see Chapter 2), did not fit within the prevailing proxy framework (Castañeda and Schouten, 2011; Gao et al., 2011; Sachse et al., 2012). These compounds are in generally low absolute abundance in Greenland sediments (Chapter 2), and the H isotopic composition of modern mid-chain waxes poorly correlates to that of modern lake water on the island (Chapter 4, 5). Further, the downcore H isotopic trends of C_{23} *n*-alkanes in both lacustrine archives evaluated here (Chapter 4,5) did not match the trends of a definitive lake water proxy evaluated in parallel (i.e. the O isotopes of chironomid larvae head capsules). The sum of this evidence suggests mid-chain wax compounds do not track the average isotopic composition of lake water on Greenland now, and have not at any point in the Holocene. Therefore, both the source of these compounds and the driver of the H isotopic composition of this proxy remain, at best, ambiguous. Interestingly though, in both records presented here, it was also observed that mid-chain waxes expressed strong and unique trends, distinct from the trends expressed by other proxies (i.e. the O isotopic composition of chironomids, the H isotopic composition of long-chain waxes). The consistency in the trends expressed by C_{23} compounds in both of these Greenland sedimentary records suggests that the

trends expressed by mid-chain waxes are likely meaningful, and future work should be aimed at homing in on the source(s), and source water, of these compounds.

References

Aebly F. A. and Fritz S. C. (2009) Paleohydrology of Kangerlussuaq (Sondre Stromfjord), West Greenland during the last ~8000 years. *The Holocene* **19**, 91–104.

Aichner B., Herzschuh U. and Wilkes H. (2010) Influence of aquatic macrophytes on the stable carbon isotopic signatures of sedimentary organic matter in lakes on the Tibetan Plateau. *Org. Geochem.* **41**, 706–718.

Aichner B., Hilt S., Périllon C., Gillefalk M. and Sachse D. (2017) Biosynthetic hydrogen isotopic fractionation factors during lipid synthesis in submerged aquatic macrophytes: Effect of groundwater discharge and salinity. *Org. Geochem.* **113**, 10–16.

Alley R. B., Andrews J. T., Brigham-Grette J., Clarke G. K. C., Cuffey K. M., Fitzpatrick J. J., Funder S., Marshall S. J., Miller G. H., Mitrovica J. X., Muhs D. R., Otto-Bliesner B. L., Polyak L. and White J. W. C. (2010) History of the Greenland Ice Sheet: paleoclimatic insights. *Quat. Sci. Rev.* **29**, 1728–1756.

Alley R. B., Meese D. A., Shuman C. A., Gow A. J., Taylor K. C., Grootes P. M., White J. W. C., Ram M., Waddington E., Mayewski P. A. and Zielinski G. A. (1993) Abrupt increase in Greenland snow accumulation at the end of the Younger Dryas event. *Nature* **362**, 527–529.

Anderson N. J. and Leng M. J. (2004) Increased aridity during the early Holocene in West Greenland inferred from stable isotopes in laminated-lake sediments. *Quat. Sci. Rev.* **23**, 841–849.

Anderson N. J., Liversidge A. C., Mcgowan S. and Jones M. D. (2012) Lake and catchment response to Holocene environmental change : spatial variability along a climate gradient in southwest Greenland. *J. Paleolimnol.* **48**, 209–222.

Andresen C., Björck S., Bennike O. and Bond G. (2004) Holocene climate changes in southern Greenland : evidence from lake sediments. *J. Quat. Sci.* **19**, 783–795.

Axford Y., Briner J. P., Francis D. R., Miller G. H., Walker I. R. and Wolfe A. P. (2011) Chironomids record terrestrial temperature changes throughout Arctic interglacials of the past 200,000 yr. *Bull. Geol. Soc. Am.* **123**, 1275–1287.

Axford Y., Levy L. B., Kelly M. A., Francis D. R., Hall B. L., Langdon P. G. and Lowell T. V. (2017) Timing and magnitude of early to middle Holocene warming in East Greenland inferred from chironomids. *Boreas* **46**, 678–687.

Axford Y., Losee S., Briner J. P., Francis D. R., Langdon P. G. and Walker I. R. (2013) Holocene temperature history at the western Greenland Ice Sheet margin reconstructed from lake sediments. *Quat. Sci. Rev.* **59**, 87–100.

Baas M., Pancost R., Geel B. Van and Damste J. S. S. (2000) A comparative study of lipids in Sphagnum species. *Org. Geochem.* **31**, 535–541.

Bakkelund A., Porter T. J., Froese D. G. and Feakins S. J. (2018) Net fractionation of hydrogen isotopes in n-alkanoic acids from soils in the northern boreal forest. *Org. Geochem.* **125**, 1–13.

Bakker P., Masson-Delmotte V., Martrat B., Charbit S., Renssen H., Gröger M., Krebs-Kanzow U., Lohman G., Lunt D. J., Pfeiffer M., Phipps S. J., Prange M., Ritz S. P., Schulz M., Stenni B., Stone E. J. and Varma V. (2014) Temperature trends during the present and last interglacial periods - a multi-model-data comparison. *Quat. Sci. Rev.* **99**, 224–243.

Balascio N. L., D'Andrea W. J. and Bradley R. S. (2015) Glacier response to North Atlantic climate variability. *Clim. Past* **11**, 1587–1598.

Balascio N. L., D'Andrea W. J., Bradley R. S. and Perren B. B. (2013) Biogeochemical evidence for hydrologic changes during the Holocene in a lake sediment record from southeast Greenland. *The Holocene* **23**, 1428–1439.

Balco G., Stone J. O., Lifton N. A. and Dunai T. J. (2008) A complete and easily accessible

means of calculating surface exposure ages or erosion rates from 10Be and 26Al measurements. *Quat. Geochronol.* **3**, 174–195.

Barley E. M., Walker I. R., Kurek J., Cwynar L. C., Mathewes R. W., Gajewski K. and Finney B. P. (2006) A northwest North American training set: distribution of freshwater midges in relation to air temperature and lake depth. *J. Paleolimnol.* **36**, 295–314.

Bennike O., Bjo S. and Lambeck K. (2002) Estimates of South Greenland late-glacial ice limits from a new relative sea level curve. **197**, 171–186.

Bennike O. and Björck S. (2002) Chronology of the last recession of the Greenland ice sheet. *J. Quat. Sci.* **17**, 211–219.

Bennike O. and Böcher J. (1992) Early Weichselian interstadial land biotas at Thule, Northwest Greenland. *Boreas* **21**, 111–118.

Bennike O. and Böcher J. (1994) Land biotas of the last interglacial/glacial cycle on Jameson Land, East Greenland. *Boreas* **23**, 479–487.

Bennike O. and Weidick A. (2001) Late Quaternary history around Nioghalvfjerdsfjorden and Jøkelbugten, North-East Greenland. *Boreas* **30**, 205–227.

Berke M. A., Sierra A. C., Bush R., Cheah D. and O'Connor K. (2019) Controls on leaf wax d2H and fractionation values in tundra vegetation from western greenland. *Geochim. Cosmochim. Acta* **224**, 565–583.

Bierman P. R., Shakun J. D., Corbett L. B., Zimmerman S. R. and Rood D. H. (2016) A persistent and dynamic East Greenland Ice Sheet over the past 7.5 million years. *Nature* **540**, 256–260.

Björck S., Bennike O., Rosén P., Andresen C., Bohncke S., Kaas E. and Conley D. (2002) Anomalously mild Younger Dryas summer conditions in southern. *Geology* **30**, 427–430.

Blaauw M. and Christen J. (2011) Flexible Paleoclimate Age-Depth Models Using an

Autoregressive Gamma Process. *Bayesian Anal.* **6**, 457–474.

Borkent A. (1993) A world catalogue of fossil and extant Corethrellidae and Chaoboridae (Diptera), with a listing of references to keys, bionomic information and descriptions of each known life stage. *Insect Syst. Evol.* **24**, 1–24.

Born A. and Nisancioglu K. H. (2012) Melting of Northern Greenland during the last interglaciation. *Cryosph.* **6**, 1239–1250.

Bowen G. J. (2018) The Online Isotopes in Precipitation Calculator, version 3.1.

Bowen G. J. and Revenaugh J. (2003) Interpolating the isotopic composition of modern meteoric precipitation. *Water Resour. Res.* **39**, 1–13.

Bowen G. J., Wassenaar L. I. and Hobson K. A. (2005) Global application of stable hydrogen and oxygen isotopes to wildlife forensics. *Oecologia* **143**, 337–348.

Briner J. P., Axford Y., Forman S. L., Miller G. H. and Wolfe A. P. (2007) Multiple generations of interglacial lake sediment preserved beneath the Laurentide Ice Sheet. *Geology* **35**, 887–890.

Briner J. P., McKay N. P., Axford Y., Bennike O., Bradley R. S., de Vernal A., Fisher D., Francus P., Fréchette B., Gajewski K., Jennings A., Kaufman D. S., Miller G., Rouston C. and Wagner B. (2016) Holocene climate change in Arctic Canada and Greenland. *Quat. Sci. Rev.* **147**, 340–364.

Briner J. P., Michelutti N., Francis D. R., Miller G. H., Axford Y., Wooller M. J. and Wolfe A. P. (2006) A multi-proxy lacustrine record of Holocene climate change on northeastern Baffin Island, Arctic Canada. *Quat. Res.* **65**, 431–442.

van den Broeke M., Bamber J., Ettema J., Rignot E., Schrama E., Jan van de Berg W., van Meijgaard E., Velicogna I. and Wouters B. (2009) Partitioning Recent Greenland Mass Loss. *Science* **326**, 984–986.

Buizert C., Keisling B. A., Box J. E., He F., Carlson A. E., Sinclair G. and DeConto R. M. (2018) Greenland-wide seasonal temperature reconstructions for the last deglaciation. *Geophys. Res. Lett.* **45**, 1905–1914.

Bush R. T., Berke M. A. and Jacobson A. D. (2017) Plant water dD and d18O of tundra species from west Greenland. *Arctic, Antarct. Alp. Res.* **49**, 341–358.

Bush R. T. and McInerney F. A. (2013) Leaf wax n-alkane distributions in and across modern plants: Implications for paleoecology and chemotaxonomy. *Geochim. Cosmochim. Acta* **117**, 161–179.

CAPE-Last Interglacial Project Members (2006) Last Interglacial Arctic warmth confirms polar amplification of climate change. *Quat. Sci. Rev.* **25**, 1383–1400.

Cappa C. D., Hendricks M. B., Depaolo D. J. and Cohen R. C. (2003) Isotopic fractionation of water during evaporation. *J. Geophys. Res.* **108**, 1–10.

Cappelen J., Jørgensen B. V, Laursen E. V and Thomsen Lss. (2001) The Observed Climate of Greenland, 1958-99 - with Climatological Standard Normals, 1961-90. *Danish Meteorol. Institute, Tech. Rep.* **00**–**18**, 1–152.

Capron E., Govin A., Stone E. J., Masson-Delmotte V., Mulitza S., Otto-Bliesner B., Rasmussen T. L., Sime L. C., Waelbroeck C. and Wolff E. W. (2014) Temporal and spatial structure of multi-millennial temperature changes at high latitudes during the Last interglacial. *Quat. Sci. Rev.* **103**, 116–133.

Carlson A., Winsor K., Ullman D., Brook E., Rood D., Axford Y., LeGrande A., Anslow F. and Sinclair G. (2014) Earliest Holocene south Greenland ice sheet retreat within its late Holocene extent. *Geophys. Res. Lett.* **41**, 1–8.

Castañeda I. S. and Schouten S. (2011) A review of molecular organic proxies for examining modern and ancient lacustrine environments. *Quat. Sci. Rev.* **30**, 2851–2891.

Chikaraishi Y. and Naraoka H. (2003) Compound-specific dD-d13C analyses of n-alkanes extracted from terrestrial and aquatic plants. *Phytochemistry* **63**, 361–371.

Chikaraishi Y. and Naraoka H. (2007) δ13C and δD relationships among three n-alkyl compound classes (n-alkanoic acid, n-alkane and n-alkanol) of terrestrial higher plants. *Org. Geochem.* **38**, 198–215.

Church J. A., Clark P. U., Cazenave A., Gregory J. M., Jevrejeva S., Levermann A., Merrifield M. A., Milne G. A., Nerem R. ., Nunn P. D., Payne A. J., Pfeffer W. T., Stammer D. and Unnikrishnan A. S. (2013) Sea level change. In *Climate Change 2013: The Physical Science Basis. Contribution of Working Group 1 to the Fifth Assessment Report of the Intergovernmental Panel on Climate Change* Cambridge University Press, Cambridge, United Kingdom and New York, NY, USA. pp. 1137–1216.

Clark P. U., Shakun J. D., Marcott S. A., Mix A. C., Eby M., Kulp S., Levermann A., Milne G. A., Pfister P. L., Santer B. D., Schrag D. P., Solomon S., Stocker T. F., Strauss B. H., Weaver A. J., Winkelmann R., Archer D., Bard E., Goldner A., Lambeck K., Pierrehumbert R. T. and Plattner G. (2016) Consequences of twenty-first century policy for multi-millennial climate and sea-level change. *Nat. Clim. Chang.* **6**, 360–369.

Cohen J., Screen J. A., Furtado J. C., Barlow M., Whittleston D., Coumou D., Francis J., Dethloff K., Entekhabi D., Overland J. and Jones J. (2014) Recent Arctic amplification and extreme mid-latitude weather. *Nat. Geosci.* **7**, 627–637.

Collins M., Knutti R., Arblaster J., Fichefet T., Friedlingstein P., Gao X., Gutowski W. J., Johns T., Krinner G., Shongwe M., Tebaldi C., Weaver A. J. and Wehner M. (2013) Long-term Climate Change: Projections, Commitments and Irreversibility. In *Climate Change 2013: The Physical Science Basis. Contribution of Working Group 1 to the Fifth Assessment Report of the Intergovernmental Panel on Climate Change* Cambridge University Press,

Cambridge, United Kingdom and New York, NY, USA. pp. 1029–1136.

Colville E. J., Carlson A. E., Beard B. L., Hatfield R. G., Stoner J. S., Reyes A. V and Ullman D. J. (2011) Sr-Nd-Pb isotope evidence for ice-sheet presence on southern Greenland during the Last Interglacial. *Science* **333**, 620–623.

Contreras-Rosales L. A., Jennerjahn T., Tharammal T., Meyer V. and Lückge A. (2014) Evolution of the Indian Summer Monsoon and terrestrial vegetation in the Bengal region during the past 18 ka. *Quat. Sci. Rev.* **102**, 133–148.

Corbett L. B., Bierman P. R., Lasher G. E. and Rood D. H. (2015) Landscape chronology and glacial history in Thule, northwest Greenland. *Quat. Sci. Rev.* **109**, 57–67.

Criss R. E. (1999) *Principles of stable isotope distribution*., Oxford University Press on Demand.

Cuffey K. M. and Clow G. D. (1997) Temperature, accumulation, and ice sheet elevation in central Greenland through the last deglacial transition. *J. Geophys. Res.* **102**, 26383–26396.

D'Andrea W. J., Huang Y., Fritz S. C. and Anderson N. J. (2011) Abrupt Holocene climate change as an important factor for human migration in West Greenland. *Proc. Natl. Acad. Sci.* **108**, 9765–9769.

D'Odorico P., He Y., Collins S., De Wekker S. F. J., Engel V. and Fuentes J. D. (2013) Vegetation–microclimate feedbacks in woodland–grassland ecotones. *Glob. Ecol. Biogeogr.* **22**, 364–379.

Dahl-Jensen D., Albert M. R., Aldahan A., Azuma N., Balslev-Clausen D., Baumgartner M., Berggren A.-M., Bigler M., Binder T., Blunier T., Bourgeois J. C., Brook E. J., Buchardt S. L., Buizert C., Capron E., Chappellaz J., Chung J., Clausen H. B., Cvijanovic I., Davies S. M., Ditlevsen P., Eicher O., Fischer H., Fisher D. A., Fleet L. G., Gfeller G., Gkinis V., Gogineni S., Goto-Azuma K., Grinsted A., Gudlaugsdottir H., Guillevic M., Hansen S. B., Hansson M., Hirabayashi M., Hong S., Hur S. D., Huybrechts P., Hvidberg C. S., Iizuka Y.,

Jenk T., Johnsen S. J., Jones T. R., Jouzel J., Karlsson N. B., Kawamura K., Keegan K., Kettner E., Kipfstuhl S., Kjær H. a., Koutnik M., Kuramoto T., Köhler P., Laepple T., Landais A., Langen P. L., Larsen L. B., Leuenberger D., Leuenberger M., Leuschen C., Li J., Lipenkov V., Martinerie P., Maselli O. J., Masson-Delmotte V., McConnell J. R., Miller H., Mini O., Miyamoto A., Montagnat-Rentier M., Mulvaney R., Muscheler R., Orsi a. J., Paden J., Panton C., Pattyn F., Petit J.-R., Pol K., Popp T., Possnert G., Prié F., Prokopiou M., Quiquet A., Rasmussen S. O., Raynaud D., Ren J., Reutenauer C., Ritz C., Röckmann T., Rosen J. L., Rubino M., Rybak O., Samyn D., Sapart C. J., Schilt A., Schmidt a. M. Z., Schwander J., Schüpbach S., Seierstad I., Severinghaus J. P., Sheldon S., Simonsen S. B., Sjolte J., Solgaard a. M., Sowers T., Sperlich P., Steen-Larsen H. C., Steffen K., Steffensen J. P., Steinhage D., Stocker T. F., Stowasser C., Sturevik a. S., Sturges W. T., Sveinbjörnsdottir A., Svensson A., Tison J.-L., Uetake J., Vallelonga P., van de Wal R. S. W., van der Wel G., Vaughn B. H., Vinther B., Waddington E., Wegner A., Weikusat I., White J. W. C., Wilhelms F., Winstrup M., Witrant E., Wolff E. W., Xiao C. and Zheng J. (2013) Eemian interglacial reconstructed from a Greenland folded ice core. *Nature* **493**, 489–494.

Dahl-Jensen D., Mosegaard K., Gundestrup N., Clow G., Johnsen S., Hansen A. and Balling N. (1998) Past Temperatures Directly from the Greenland Ice Sheet. *Science* **282**, 268–281.

Daniels W. C., Huang Y., Russell J. M. and Giblin A. E. (2018) Effect of continuous light on leaf wax isotope ratios in Betula nana and Eriophorum vaginatum: implications for Arctic paleoclimate. *Org. Geochem.* **125**, 70–81.

Daniels W. C., Russell J. M., Giblin A. E., Welker J. M., Klein E. S. and Huang Y. (2017) Hydrogen isotope fractionation in leaf waxes in the Alaskan Arctic tundra. *Geochim. Cosmochim. Acta* **213**, 216–236.

Dansgaard W. (1964) Stable isotopes in precipitation. *Tellus* **16**, 436–468.

Diefendorf A. F. and Freimuth E. J. (2017) Extracting the most from terrestrial plant-derived n-alkyl lipids and their carbon isotopes from the sedimentary record: A review. *Org. Geochem.* **103**, 1–21.

Dion-Kirschner H., McFarlin J., Axford Y. and Osburn M. (2017) Constraining lipid biomarker paleoclimate proxies in a small arctic watershed. In *AGU Annual Fall Meeting* New Orleans.

Douglas P. M. J., Pagani M., Brenner M., Hodell D. A. and Curtis J. H. (2012) Aridity and vegetation composition are important determinants of leaf-wax δD values in southeastern Mexico and Central America. *Geochim. Cosmochim. Acta* **97**, 24–45.

Duan Y., Wu B., Xu L., He J. and Sun T. (2011) Characterization of n-alkanes and their hydrogen isotopic composition in sediments from Lake Qinghai, China. *Org. Geochem.* **42**, 720–726.

Duan Y. and Xu L. (2012) Distributions of n-alkanes and their hydrogen isotopic composition in plants from Lake Qinghai (China) and the surrounding area. *Appl. Geochemistry* **27**, 806–814.

Dutton A., Carlson A. E., Long A. J., Milne G. A., Clark P. U., DeConto R., Horton B. P., Rahmstorf S. and Raymo M. E. (2015) Sea-level rise due to polar ice-sheet mass loss during past warm periods. *Science* **349**, aaa40191-aaa40199.

Eglinton G. and Hamilton R. J. (1967) Leaf Epicuticular Waxes. *Science* **156**, 1322–1335.

Eisner W. R., Tornqvist T. E., Koster E. a, Bennike O. and Vanleeuwen J. F. N. (1995) Paleoecological Studies Of A Holocene Lacustrine Record From The Kangerlussuaq (Sondre Stromfjord) Region Of West Greenland. *Quat. Res.* **43**, 55–66.

Farnsworth L. B. (2016) Late Glacial and Holocene History of the Greenland Ice Sheet Margine

in Nunatarssuaq, Northwestern Greenland. Dartmouth College.

Farnsworth L. B., Kelley M. A., Bromley G. R. M., Axford Y., Osterberg E. C., Howley J. A., Jackson M. S. and Zimmerman S. R. (2018) Holocene history of the Greenland Ice Sheet margin in northern Nunatarssuaq, northwest Greenland. *Arktos J. Arct. Geosci.* **4**, 1–27.

Farquhar G. D., Cernusak L. A. and Barnes B. (2007) Heavy Water Fractionation during Transpiration. *Plant Physiol.* **143**, 11–18.

Feakins S. J. and Sessions A. L. (2010) Controls on the D/H ratios of plant leaf waxes in an arid ecosystem. *Geochim. Cosmochim. Acta* **74**, 2128–2141.

Feakins S. J., Warny S. and Lee J.-E. (2012) Hydrologic cycling over Antarctica during the Middle Miocene warming. *Nat. Geosci.* **5**, 557–560.

Fettweis X., Hanna E., Gallée H., Huybrechts P. and Erpicum M. (2008) The Cryosphere Estimation of the Greenland ice sheet surface mass balance for the 20th and 21st centuries. *Cryosph.* **2**, 117–129.

Ficken K. J., Li B., Swain D. L. and Eglinton G. (2000) An n-alkane proxy for the sedimentary input of submerged/floating freshwater aquatic macrophytes. *Org. Geochem.* **31**, 745–749.

Fortin M.-C., Medeiros A. S., Gajewski K., Barley E. M., Larocque-Tobler I., Porinchu D. F. and Wilson S. E. (2015) Chironomid-environment relations in northern North America. *J. Paleolimnol.* **54**, 223–237.

Francis D. R., Wolfe A. P., Walker I. R. and Miller G. H. (2006) Interglacial and Holocene temperature reconstructions based on midge remains in sediments of two lakes from Baffin Island, Nunavut, Arctic Canada. *Palaeogeogr. Palaeoclimatol. Palaeoecol.* **236**, 107–124.

Francis J. A., White D. M., Cassano J. J., Jr W. J. G., Hinzman L. D., Holland M. M., Steele M. A. and Vo C. J. (2009) An arctic hydrologic system in transition: Feedbacks and impacts on terrestrial, marine, and human life. *J. Geophys. Res.* **114**, 1–30.

Frechette B. and de Vernal A. (2009) of the Past Relationship between Holocene climate variations over southern Greenland and eastern Baffin Island and synoptic circulation pattern. *Clim. Past* **5**, 347–359.

Fréchette B., Wolfe A. P., Miller G. H., Richard P. J. H. and de Vernal A. (2006) Vegetation and climate of the last interglacial on Baffin Island, Arctic Canada. *Palaeogeogr. Palaeoclimatol. Palaeoecol.* **236**, 91–106.

Fredskild B. (1991) The genus Betula in Greenland - Holocene history , present distribution and synecology Immigration and Holocene history. *Nord. J. Bot.* **11**, 393–412.

Fredskild B. (1985) The Holocene vegetational development of Tugtuligssuaq and Qeqertat, Northwest Greenland. *Meddelelser om Grønland, Geosci.* **14**, 1–20.

Freimuth E. J., Diefendorf A. F. and Lowell T. V. (2017) Hydrogen isotopes of n-alkanes and n-alkanoic acids as tracers of precipitation in a temperate forest and implications for paleorecords. *Geochim. Cosmochim. Acta* **206**, 166–183.

Funder S. (1990) Late Quanternary stratigraphy and glaciology in the Thule area, Northwest Greenland. *Meddelelser om Grønland, Geosci.* **22**, 1–63.

Funder S., Kjeldsen K. K., Kjær K. H. and Ó Cofaigh C. (2011) The Greenland Ice Sheet During the Past 300,000 Years: A Review. *Dev. Quat. Sci.* **15**, 699–713.

Gajewski K. (2015) Quantitative reconstruction of Holocene temperatures across the Canadian Arctic and Greenland. *Glob. Planet. Change* **128**, 14–23.

Gao L., Hou J., Toney J., MacDonald D. and Huang Y. (2011) Mathematical modeling of the aquatic macrophyte inputs of mid-chain n-alkyl lipids to lake sediments: Implications for interpreting compound specific hydrogen isotopic records. *Geochim. Cosmochim. Acta* **75**, 3781–3791.

Garcin Y., Schwab V. F., Gleixner G., Kahmen A., Todou G., Séné O., Onana J. M.,

Achoundong G. and Sachse D. (2012) Hydrogen isotope ratios of lacustrine sedimentary n-alkanes as proxies of tropical African hydrology: Insights from a calibration transect across Cameroon. *Geochim. Cosmochim. Acta* **79**, 106–126.

Gat J. R. (1996) Oxygen and Hydrogen Isotopes in the Hydrologic Cycle. *Annu. Rev. Earth Planet. Sci.* **24**, 225–262.

Gibson J. J., Birks S. J. and Yi Y. (2016) Stable isotope mass balance of lakes: A contemporary perspective. *Quat. Sci. Rev.* **131**, 316–328.

Goelzer H., Huybrechts P., Loutre M.-F. and Fichefet T. (2016) Last Interglacial climate and sea-level evolution from a coupled ice sheet-climate model. *Clim. Past Discuss.* **12**, 2195–2213.

Guenther F., Aichner B., Siegwolf R., Xu B., Yao T. and Gleixner G. (2013) A synthesis of hydrogen isotope variability and its hydrological significance at the Qinghai-Tibetan Plateau. *Quat. Int.* **313**–**314**, 3–16.

van Hardenbroek M., Chakraborty A., Davies K. L., Harding P., Heiri O., Schilder J., Trueman C. N. and Wooller M. J. (2018) The stable isotope composition of organic and inorganic fossils in lake sediment records : Current understanding , challenges , and future directions. *Quat. Sci. Rev.* **196**, 154–176.

Hartmann D., Klein Tank A., Rusticucci M., Alexander L., Bronnimann S., Charabi Y., Dentener F., Dlugokencky E., Easterling D., Kaplan A., Soden B., Thorne P., Wild M. and Zhai P. (2013) Observations: Atmosphere and Surface. In *Climate Change 2013: The Physical Science Basis. Contribution of Working Group 1 to the Fifth Assessment Report of the Intergovernmental Panel on Climate Change* pp. 159–255.

Helliker B. and Ehleringer J. R. (2002) Differential 18 O enrichment of leaf cellulose in C 3 versus C 4 grasses. *Funct. Plant Biol.* **29**, 435–442.

Helsen M. M., van de Berg W. J., van de Wal R. S. W., van den Broeke M. R. and Oerlemans J. (2013) Coupled regional climate-ice-sheet simulation shows limited Greenland ice loss during the Eemian. *Clim. Past* **9**, 1773–1788.

Hepp J., Tuthorn M., Zech R., Mügler I., Schlütz F., Zech W. and Zech M. (2014) Reconstructing lake evaporation history and the isotopic composition of precipitation by a coupled d18O-d2H biomarker approach. *J. Hydrol.* **529**, 622–631.

Horita J. and Wesolowski D. J. (1994) Liquid-vapor fractionation of oxygen and hydrogen isotopes of water from the freezing to the critical temperature. *Geochim. Cosmochim. Acta* **58**, 3425–3437.

Hou J., D'Andrea W. J., MacDonald D. and Huang Y. (2007) Hydrogen isotopic variability in leaf waxes among terrestrial and aquatic plants around Blood Pond, Massachusetts (USA). *Org. Geochem.* **38**, 977–984.

Huang Y., Shuman B., Wang Y. and Webb T. (2004) Hydrogen isotope ratios of individual lipids in lake sediments as novel tracers of climatic and environmental change: A surface sediment test. *J. Paleolimnol.* **31**, 363–375.

IAEA/WMO (2017) Global Network of Isotopes in Precipitation. The GNIP Database.

Jensen D. B. and Christensen K. D. (2003) *The Biodiversity of Greenland – a country study*., Pinngortitaleriffik, Grønlands Naturinstitut, Nuuk, Greenland.

Kaplan M. R., Wolfe A. P. and Miller G. H. (2002) Holocene Environmental Variability in Southern Greenland Inferred from Lake Sediments. *Quat. Res.* **159**, 149–159.

Kaufman D. S., Ager T. A., Anderson N. J., Anderson P. M., Andrews J. T., Bartlein P. J., Brubaker L. B., Coats L. L., Cwynar L. C., Duvall M. L. and Dyke A. S. (2004) Holocene thermal maximum in the western Arctic (0–180_W). **23**, 529–560.

Kelly M., Funder S., Houmark-Nielsen M., Knudsen K. L., Kronborg C., Landvik J. and Sorby

L. (1999) Quaternary glacial and marine environmental history of northwest Greenland: a review and reappraisal. *Quat. Sci. Rev.* **18**, 373–392.

Kjeldsen K., Korsgaard N., Bjørk A., Khan S., Box J., Funder S., Larsen N., Bamber J., Colgan W., van den Broeke M., Siggaard-Andersen M.-L., Nuth C., Schomacker A., Andresen C., Willerslev E. and Kjær K. (2015) Spatial and temporal distribution of mass loss from the Greenland Ice Sheet since ad 1900. *Nature* **528**, 396–400.

Koch K. and Ensikat H. (2008) The hydrophobic coatings of plant surfaces: Epicuticular wax crystals and their morphologies, crystallinity and molecular self-assembly. *Micron* **39**, 759–772.

Kohn M. J. (2010) Carbon isotope compositions of terrestrial C3 plants as indicators of (paleo)ecology and (paleo)climate. *Proc. Natl. Acad. Sci.* **107**, 19691–19695.

Ladd S. N., Nelson D. B., Schubert C. J. and Dubois N. (2018) Lipid compound classes display diverging hydrogen isotope responses in lakes along a nutrient gradient. *Geochim. Cosmochim. Acta* **237**, 103–119.

Landais A., Masson-Delmotte V., Capron E., Langebroek P. M., Bakker P., Stone E. J., Merz N., Raible C. C., Fischer H., Orsi A., Prie F., Vinther B. and Dahl-Jensen D. (2016) How warm was Greenland during the last interglacial period? *Clim. Past* **12**, 1933–1948.

Larsen N., Find J., Kristensen A., Bjørk A., Kjeldsen K., Odgaard B., Olsen J. and Kjær K. (2016) Holocene ice marginal fluctuations of the Qassimiut lobe in South Greenland. *Nature* **6**, 22362.

Larsen N. K., Kjær K. H., Lecavalier B., Bjørk A. A., Colding S., Huybrechts P., Jakobsen K. E., Kjeldsen K. K., Knudsen K., Odgaard B. V and Olsen J. (2015) The response of the southern Greenland ice sheet to the Holocene thermal maximum. *Geology* **43**, 1–4.

Larsen N. K., Kjær K. H., Olsen J., Funder S., Kjeldsen K. K. and Nørgaard-pedersen N. (2011)

Restricted impact of Holocene climate variations on the southern Greenland Ice Sheet. *Quat. Sci. Rev.* **30**, 3171–3180.

Larsen N. K., Levy L. B., Strunk A., Søndergaard A. S., Olsen J. and Lauridsen T. L. (2019) Local ice caps in Finderup Land, North Greenland, survived the Holocene Thermal Maximum. *Boreas*.

Larsen N. K., Strunk A., Levy L. B., Olsen J., Bjørk A., Lauridsen T. L., Jeppesen E. and Davidson T. A. (2017) Strong altitudinal control on the response of local glaciers to Holocene climate change in southwest Greenland. **168**, 69–78.

Lasher G. E. and Axford Y. (2019) Medieval warmth confirmed at the Norse Eastern Settlement in Greenland. **47**, 267–270.

Lasher G. E., Axford Y., McFarlin J. M., Kelly M. A., Osterberg E. C. and Berkelhammer M. B. (2017) Holocene temperatures and isotopes of precipitation in Northwest Greenland recorded in lacustrine organic materials. *Quat. Sci. Rev.* **170**, 45–55.

Leary M. J. O., Hearty P. J., Thompson W. G., Raymo M. E., Mitrovica J. X., Webster J. M. and O'Leary M. J. (2013) Ice sheet collapse following a prolonged period of stable sea level during the last interglacial. *Nat. Geosci.* **6**, 796–800.

Lecavalier B. S., Fisher D. A., Milne G. A., Vinther B. M., Tarasov L., Huybrechts P., Lacelle D., Main B., Zheng J., Bourgeois J. and Dyke A. S. (2017) High Arctic Holocene temperature record from the Agassiz ice cap and Greenland ice sheet evolution. *Proc. Natl. Acad. Sci.* **114**, 5952–5957.

Lecavalier B. S., Milne G. A., Simpson M. J. R., Wake L., Huybrechts P., Tarasov L., Kjeldsen K. K., Funder S., Long A. J., Woodroffe S., Dyke A. S. and Larsen N. K. (2014) A model of Greenland ice sheet deglaciation constrained by observations of relative sea level and ice extent. *Quat. Sci. Rev.* **102**, 54–84.

Lecavalier B. S., Milne G., Vinther B. M., Fisher D. A., Dyke A. S. and Simpson M. J. R. (2013) Revised estimates of Greenland ice sheet thinning histories based on ice-core records. *Quat. Sci. Rev.* **63**, 73–82.

Leider A., Hinrichs K. U., Schefuß E. and Versteegh G. J. M. (2013) Distribution and stable isotopes of plant wax derived n-alkanes in lacustrine, fluvial and marine surface sediments along an Eastern Italian transect and their potential to reconstruct the hydrological cycle. *Geochim. Cosmochim. Acta* **117**, 16–32.

Linderholm H. W., Nicolle M., Francus P., Gajewski K., Helama S., Korhola A., Solomina O., Yu Z., Zhang P., D'Andrea W. J., Debret M., Divine D. V., Gunnarson B. E., Loader N. J., Massei N., Seftigen K., Thomas E. K., Werner J., Andersson S., Berntsson A., Luoto T. P., Nevalainen L., Saarni S. and Valiranta M. (2018) Arctic hydroclimate variability during the last 2000 years. *Clim. Past* **14**, 473–514.

Liu H. and Liu W. (2016) n-Alkane distributions and concentrations in algae, submerged plants and terrestrial plants from the Qinghai-Tibetan Plateau. *Org. Geochem.* **99**, 10–22.

Liu W. and Yang H. (2008) Multiple controls for the variability of hydrogen isotopic compositions in higher plant n-alkanes from modern ecosystems. *Glob. Chang. Biol.* **14**, 2166–2177.

Liu W., Yang H., Wang H., An Z., Wang Z. and Leng Q. (2015) Organic Geochemistry Carbon isotope composition of long chain leaf wax n -alkanes in lake sediments : A dual indicator of paleoenvironment in the Qinghai-Tibet Plateau. *Org. Geochem.* **83**–**84**, 190–201.

Liu Z., Zhu J., Rosenthal Y., Zhang X., Otto-bliesner B. L., Timmermann A., Smith R. S., Lohmann G., Zheng W. and Timm O. E. (2014) The Holocene temperature conundrum. *Proc. Natl. Acad. Sci.* **111**, E3501–E3505.

Lunt D. J., Abe-Ouchi A., Bakker P., Berger A., Braconnot P., Charbit S., Fischer N., Herold N.,

Jungclaus J. H., Khon V. C., Krebs-Kanzow U., Langebroek P. M., Lohmann G., Nisancioglu K. H., Otto-Bliesner B. L., Park W., Pfeiffer M., Phipps S. J., Prange M., Rachmayani R., Renssen H., Rosenbloom N., Schneider B., Stone E. J., Takahashi K., Wei W., Yin Q. and Zhang Z. S. (2013) A multi-model assessment of last interglacial temperatures. *Clim. Past* **9**, 699–717.

Lüthi D., Le Floch M., Bereiter B., Blunier T., Barnola J.-M., Siegenthaler U., Raynaud D., Jouzel J., Fischer H., Kawamura K. and Stocker T. F. (2008) High-resolution carbon dioxide concentration record 650,000-800,000 years before present. *Nature* **453**, 379–382.

Marcott S. A., Shakun J. D., Clark P. U. and Mix A. C. (2013) A Reconstruction of Regional and Global Temperature for the Past 11,300 Years. *Science* **339**, 1198–1201.

Massa C., Perren B. B., Gauthier É., Bichet V., Petit C. and Richard H. (2012) A multiproxy evaluation of Holocene environmental change from Lake Igaliku , South Greenland. *J. Paleolimnol.* **48**, 241–258.

Masson-Delmotte V., Schulz M., Abe-Ouchi A., Beer J., Ganopolski A., Gonzalez Rouco J. F., Jansen E., Lambeck K., Luterbacher J., Naish T., Osborn T., Otto-Bliesner B., Quinn T., Ramesh R., Rojas M., Shao X. and Timmermann A. (2013) Information from Paleoclimate Archives. In *Climate Change 2013: The Physical Science Basis. Contribution of Working Group 1 to the Fifth Assessment Report of the Intergovernmental Panel on Climate Change* (eds. T. F. Stocker, D. Qin, G. K. Plattner, M. Tignor, S. K. Allen, J. Boschung, A. Nauels, Y. Xia, B. Bex, and B. M. Midgley). Cambridge University Press, Cambridge, United Kingdom and New York, NY, USA. pp. 383–464.

Masson-Delmotte V., Steen-Larsen H. C., Ortega P., Swingedouw D., Popp T., Vinther B. M., Oerter H., Sveinbjörnsdóttir Á. E., Gudlaugsdottir H., Box J. ., Falourd S., Fettweis X., Gallee H., Garnier E., Gkinis V., Jouzel J., Landais A., Minster B., Paradis N., Orsi A., Risi

C., Werner M. and White J. W. C. (2015) Recent changes in north-west Greenland climate documented by NEEM shallow ice core data and simulations , and implications for past-temperature reconstructions. *Cryosph.* **9**, 1481–1504.

McFarlin J. M., Axford Y., Osburn M. R., Kelly M. A., Osterberg E. C. and Farnsworth L. B. (2018) Pronounced summer warming in northwest Greenland during the Holocene and Last Interglacial. *Proc. Natl. Acad. Sci.***115**, 6357-6362.

McFarlin J., Osburn M., Axford Y. and Masterson A. (2018) A calibration of hydrogen isotope ratios of sedimentary plant waxes as a proxy for meteoric water in the Arctic. In *AGU Annual Fall Meeting* Washington D.C.

McGowan S. M., Ryves D. B. and Anderson N. J. (2003) Holocene records of effective precipitation in West Greenland. *The Holocene* **2**, 239–249.

Medley B. and Thomas E. R. (2019) Increased snowfall over the Antarctic Ice Sheet mitigated twentieth-century sea-level rise. *Nat. Clim. Chang.* **9**, 34–39.

Merz N., Born A., Raible C. C., Fischer H. and Stocker T. F. (2014) Dependence of Eemian Greenland temperature reconstructions on the ice sheet topography. *Clim. Past* **10**, 1221–1238.

Miller G. H., Alley R. B., Brigham-Grette J., Fitzpatrick J. J., Polyak L., Serreze M. C. and White J. W. C. (2010) Arctic amplification: can the past constrain the future? *Quat. Sci. Rev.* **29**, 1779–1790.

Mügler I., Sachse D., Werner M., Xu B., Wu G., Yao T. and Gleixner G. (2008) Effect of lake evaporation on δD values of lacustrine n-alkanes: A comparison of Nam Co (Tibetan Plateau) and Holzmaar (Germany). *Org. Geochem.* **39**, 711–729.

Muschitiello F., Pausata F. S. R., Watson J. E., Smittenberg R. H., Salih A. A. M., Brooks S. J., Whitehouse N. J., Karlatou-Charalampopoulou A. and Wohlfarth B. (2015) Fennoscandian

freshwater control on Greenland hydroclimate shifts at the onset of the Younger Dryas. *Nat. Commun.* **6**, 8939.

Nelson D. B., Ladd S. N., Schubert C. J. and Kahmen A. (2018) Rapid atmospheric transport and large-scale deposition of recently synthesized plant waxes. *Geochim. Cosmochim. Acta* **222**, 599–617.

NGRIP Project Members (2004) High-resolution record of Northern Hemisphere climate extending into the last interglacial period. *Nature* **431**, 147–151.

Nichols J., Booth R. K., Jackson S. T., Pendall E. G. and Huang Y. (2010) Differential hydrogen isotopic ratios of Sphagnum and vascular plant biomarkers in ombrotrophic peatlands as a quantitative proxy for precipitation-evaporation balance. *Geochim. Cosmochim. Acta* **74**, 1407–1416.

Nichols J. E., Booth R. K., Jackson S. T., Pendall E. G. and Huang Y. (2006) Paleohydrologic reconstruction based on n -alkane distributions in ombrotrophic peat. *Org. Geochem.* **37**, 1505–1513.

Nott C. J., Xie S., Avsejs L. A., Maddy D., Chambers F. M. and Evershed R. P. (2000) n -Alkane distributions in ombrotrophic mires as indicators of vegetation change related to climatic variation. *Org. Geochem.* **31**, 231–235.

Otto-Bliesner B. L., Marshall S. J., Overpeck J. T., Miller G. H., Hu A. and CAPE-Last Interglacial Project Members (2006) Simulating Arctic Climate Warmth and Icefield Retreat in the Last Interglaciation. *Science* **311**, 1751–1753.

Overpeck J. T., Webb III T. and Prentice I. C. (1985) Quantitative interpretation of fossil pollen spectra: Dissimilarity coefficients and the method of modern analogs. *Quat. Res.* **23**, 87–108.

Pagani M., Pedentchouk N., Huber M., Sluijs A., Schouten S., Brinkhuis H., Damsté J. S. S. and

Dickens G. R. (2006) Arctic hydrology during global warming at the Palaeocene/Eocene thermal maximum. *Nature* **442**, 671–675.

Perren B. B., Anderson N. J., Douglas M. S. V and Fritz S. C. (2012) The influence of temperature , moisture , and eolian activity on Holocene lake development in West Greenland. *J. Paleolimnol.* **48**, 223–239.

Plach A., Nisancioglu K. H., Le S., Born A., Langebroek P. M., Guo C., Imhof M. and Stocker T. (2018) Eemian Greenland SMB strongly sensitive to model choice. *Clim. Past* **14**, 1463–1485.

Polissar P. J. and Freeman K. H. (2010) Effects of aridity and vegetation on plant-wax δD in modern lake sediments. *Geochim. Cosmochim. Acta* **74**, 5785–5797.

Polissar P. J., Freeman K. H., Rowley D. B., McInerney F. A. and Currie B. S. (2009) Paleoaltimetry of the Tibetan Plateau from D/H ratios of lipid biomarkers. *Earth Planet. Sci. Lett.* **287**, 64–76.

Rach O., Kahmen A., Brauer A. and Sachse D. (2017) A dual-biomarker approach for quantification of changes in relative humidity from sedimentary lipid D/H ratios. *Clim. Past* **13**, 741–757.

Rao Z., Jia G., Qiang M. and Zhao Y. (2014) Assessment of the difference between mid- and long chain compound specific δDn-alkanes values in lacustrine sediments as a paleoclimatic indicator. *Org. Geochem.* **76**, 104–117.

Rasmussen S. O., Abbott P. M., Blunier T., Bourne A. J., Brook E., Buchardt S. L., Buizert C. and Chappellaz J. (2013) of the Past A first chronology for the North Greenland Eemian Ice Drilling (NEEM) ice core. *Clim. Past* **9**, 2713–2730.

Reimer P. J., Bard E., Bayliss A., Beck J. W., Blackwell P. G., Ramsey C. B., Buck C. E., Cheng H., Edwards R. L., Friedrich M., Grootes P. M., Guilderson T. P., Haflidason H., Hajdas I.,

Hatte C., Heaton T. J., Hoffmann D. J., Hogg A. G., Hughen K. A., Kaiser K. F., Kromer B., Manning S. W., Niu M., Reimer R. W., Richards D. A., Scott E. M., Southon J. R., Staff R. A., Turney C. S. M. and van der Plicht J. (2013) IntCal13 and Marine13 Radiocarbon Age Calibration Curves 0–50,000 Years cal BP. *Radiocarbon* **55**, 1869–1887.

Reusche M., Marcott S., Ceperley E. and Barth A. (2018) Early to Late Holocene Surface Exposure Ages From Two Marine-Terminating Outlet Glaciers in Northwest Greenland Early to Late Holocene Surface Exposure Ages From Two Marine-Terminating Outlet Glaciers in Northwest Greenland. *Geophys. Res. Lett.* **45**, 7028–7039.

Robinson A., Calov R. and Ganopolski A. (2012) Multistability and critical thresholds of the Greenland ice sheet. *Nat. Clim. Chang.* **2**, 429–432.

Roden J. S. and Ehleringer J. R. (1999) Observations of Hydrogen and Oxygen Isotopes in Leaf Water Confirm the Craig-Gordon Model under Wide-Ranging Environmental Conditions. *Plant Physiol.* **120**, 1165–1174.

Sachse D., Billault I., Bowen G. J., Chikaraishi Y., Dawson T. E., Feakins S. J., Freeman K. H., Magill C. R., McInerney F. a., van der Meer M. T. J. J., Polissar P., Robins R. J., Sachs J. P., Schmidt H.-L., Sessions A. L., White J. W. C., West J. B. and Kahmen A. (2012) Molecular paleohydrology: interpreting the hydrogen-isotopic composition of lipid biomarkers from photosynthesizing organisms. *Annu. Rev. Earth Planet. Sci.* **40**, 221–249.

Sachse D., Radke J. and Gleixner G. (2004) Hydrogen isotope ratios of recent lacustrine sedimentary n-alkanes record modern climate variability. *Geochim. Cosmochim. Acta* **68**, 4877–4889.

Schaefer J. M., Finkel R. C., Balco G., Alley R. B., Caffee M. W., Briner J. P., Young N. E., Gow A. J. and Schwartz R. (2016) Greenland was nearly ice-free for extended periods during the Pleistocene. *Nature* **540**, 252–255.

Serreze M. C., Barrett A. P., Stroeve J. C., Kindig D. N. and Holland M. M. (2009) The emergence of surface-based Arctic amplification. *Cryosph.* **3**, 11–19.

Sessions A. L. (2016) Factors controlling the deuterium contents of sedimentary hydrocarbons. *Org. Geochem.* **96**, 43–64.

Shanahan T. M., Hughen K. A., Ampel L., Sauer P. E. and Fornace K. (2013) Environmental controls on the 2H/1H values of terrestrial leaf waxes in the eastern Canadian Arctic. *Geochim. Cosmochim. Acta* **119**, 286–301.

Sime L. C., Risi C., Tindall J. C., Sjolte J., Wolff E. W., Masson-Delmotte V. and Capron E. (2013) Warm climate isotopic simulations: what do we learn about interglacial signals in Greenland ice cores? *Quat. Sci. Rev.* **67**, 59–80.

Simpson G. L. (2007) Analogue Methods in Palaeoecology : Using the analogue Package. *J. Stat. Softw.* **22**, 1–29.

Simpson M. J. R., Milne G. A., Huybrechts P. and Long A. J. (2009) Calibrating a glaciological model of the Greenland ice sheet from the Last Glacial Maximum to present-day using field observations of relative sea level and ice extent. *Quat. Sci. Rev.* **28**, 1631–1657.

Sjolte J., Hoffmann G. and Johnsen S. J. (2014) Modelling the response of stable water isotopes in Greenland precipitation to orbital configurations of the previous interglacial. *Tellus B Chem. Phys. Meteorol.* **66**, 1–16.

Steen-Larsen H. C., Masson-Delmotte V., Sjolte J., Johnsen S. J., Vinther B. M., Bréon F. M., Clausen H. B., Dahl-Jensen D., Falourd S., Fettweis X., Gallée H., Jouzel J., Kageyama M., Lerche H., Minster B., Picard G., Punge H. J., Risi C., Salas D., Schwander J., Steffen K., Sveinbjörnsdóttir A. E., Svensson A. and White J. (2011) Understanding the climatic signal in the water stable isotope records from the NEEM shallow firn/ice cores in northwest Greenland. *J. Geophys. Res. Atmos.* **116**, 1–20.

Stone E. J., Lunt D. J., Annan J. D. and Hargreaves J. C. (2013) Quantification of the Greenland ice sheet contribution to Last Interglacial sea level rise. *Clim. Past* **9**, 621–639.

Stuiver M., Reimer P. J. and Reimer R. W. (2017) CALIB 7.1 [WWW program]. Available at: http://calib.org [Accessed May 1, 2017].

Sundqvist H., Kaufman D., McKay N., Balascio N., Briner J., Cwynar L., Sejrup H., Seppa H., Subetto D. and Andrews J. (2014) Arctic Holocene proxy climate database–new approaches to assessing geochronological accuracy and encoding climate variables. *Clim. Past* **10**, 1605–1631.

Taylor D. J., Ballinger M. J., Medeiros A. S. and Kotov A. A. (2015) Climate-associated tundra thaw pond formation and range expansion of boreal zooplankton predators. *Ecography (Cop.).* **39**, 43–53.

Thomas E. K., Briner J. P., Ryan-Henry J. J. and Huang Y. (2016) A major increase in winter snowfall during the middle Holocene on western Greenland caused by reduced sea ice in Baffin Bay and the Labrador Sea. *Geophys. Res. Lett.* **43**, 5302–5308.

Thomas E. K., Castañeda I. S., McKay N. P., Briner J. P., Salacup J. M., Nguyen K. Q. and Schweinsberg A. D. (2018) A wetter Arctic coincident with hemispheric warming 8000 years ago. *Geophys. Res. Lett.*

Thomas E. K., McGrane S., Briner J. P. and Huang Y. (2012) Leaf wax δ2H and varve-thickness climate proxies from proglacial lake sediments, Baffin Island, Arctic Canada. *J. Paleolimnol.* **48**, 193–207.

Tierney J. E., Russell J. M., Huang Y., Sinninghe Damsté J. S., Hopmans E. C. and Cohen A. S. (2008) Northern Hemisphere Controls on. *Science* **322**, 252–255.

Tierney J. E., Russell J. M., Sinninghe J. S., Huang Y. and Verschuren D. (2011) Late Quaternary behavior of the East African monsoon and the importance of the Congo Air

Boundary. *Quat. Sci. Rev.* **30**, 798–807.

Tipple B. J., Hambach B., Barnette J. E., Chesson L. A. and Ehleringer J. R. (2016) The influences of cultivation setting on inflorescence lipid distributions, concentrations, and carbon isotope ratios of Cannabis sp. *Forensic Sci. Int.* **262**, 233–241.

Turney C. S. M. and Jones R. T. (2010) Does the Agulhas Current amplify global temperatures during super-interglacials? *J. Quat. Sci.* **25**, 839–843.

Vernon C. L., Bamber J. L., Box J. E., Broeke M. R. Van Den, Fettweis X., Hanna E. and Huybrechts P. (2013) The Cryosphere Surface mass balance model intercomparison for the Greenland ice sheet. *The Cryosphere* **7,** 599–614.

Vinther B. M., Buchardt S. L., Clausen H. B., Dahl-Jensen D., Johnsen S. J., Fisher D. a, Koerner R. M., Raynaud D., Lipenkov V., Andersen K. K., Blunier T., Rasmussen S. O., Steffensen J. P. and Svensson a M. (2009) Holocene thinning of the Greenland ice sheet. *Nature* **461**, 385–388.

Weidick A., Kelly M. and Bennike O. (2004) Late Quaternary development of the southern sector of the Greenland Ice Sheet, with particular reference to the Qassimiut lobe. *Boreas* **33**, 284–299.

Wilkie K. M. K., Chapligin B., Meyer H., Burns S., Petsch S. and Brigham-Grette J. (2013) Modern isotope hydrology and controls on dD of plant leaf waxes at Lake El'gygytgyn, NE Russia. *Clim. Past* **9**, 335–352.

Winsor K., Carlson A. E., Caffee M. W. and Rood D. H. (2015) Rapid last-deglacial thinning and retreat of the marine-terminating southwestern Greenland ice sheet. *Earth Planet. Sci. Lett.* **426**, 1–12.

Winsor K., Carlson A. E. and Rood D. H. (2014) Be dating of the Narsarsuaq moraine in southernmost Greenland : evidence for a late-Holocene ice advance exceeding the Little Ice

Age maximum. *Quat. Sci. Rev.* **98**, 135–143.

Wong G. J., Osterberg E. C., Hawley R. L., Courville Z. R., Ferris D. G. and Howley J. A. (2015) Coast-to-interior gradient in recent northwest Greenland precipitation trends (1952–2012). *Environ. Res. Lett.* **10**, 114008.

Woodroffe S. A., Long A. J., Lecavalier B. S., Milne G. A. and Bryant C. L. (2014) Using relative sea-level data to constrain the deglacial and Holocene history of southern Greenland. *Quat. Sci. Rev.* **92**, 345–356.

Woodward F. I., Lomas M. R. and Kelly C. K. (2004) Global climate and the distribution of plant biomes. *Philos. Trans. R. Soc. B Biol. Sci.* **359**, 1465–1476.

Wooller M. J., Francis D., Fogel M. L., Miller G. H., Walker I. R. and Wolfe A. P. (2004) Quantitative paleotemperature estimates from d18O of chironomid head capsules preserved in arctic lake sediments. *J. Paleolimnol.* **31**, 267–274.

Xia Z., Xu B., Mügler I., Wu G., Gleixner G., Sachse D. and Zhu L. (2008) Climatic implication of hydrogen isotope ratios of terrigenous n-alkanes in lacustrine surface sediment of the Tibetan Plateau. *Geochem. J.* **20**, 695–704.

Yang H., Liu W., Leng Q., Hren M. T. and Pagani M. (2011) Variation in n-alkane δD values from terrestrial plants at high latitude: Implications for paleoclimate reconstruction. *Org. Geochem.* **42**, 283–288.

Yang H., Pagani M., Briggs D. E. G., Equiza M. A., Jagels R., Leng Q. and Lepage B. A. (2009) Carbon and hydrogen isotope fractionation under continuous light: implications for paleoenvironmental interpretations of the High Arctic during Paleogene warming. *Oecologia* **160**, 461–470.

Yau A. M., Bender M. L., Robinson A. and Brook E. J. (2016) Reconstructing the last interglacial at Summit, Greenland: Insights from GISP2. *Proc. Natl. Acad. Sci.* **113**, 9710–

9715.

Young N. E. and Briner J. P. (2015) Holocene evolution of the western Greenland Ice Sheet: Assessing geophysical ice-sheet models with geological reconstructions of ice-margin change. *Quat. Sci. Rev.* **114**, 1–17.

Young N. E., Briner J. P., Rood D. H., Finkel R. C., Corbett L. B. and Bierman P. R. (2013) Age of the Fjord Stade moraines in the Disko Bugt region, western Greenland, and the 9.3 and 8.2 ka cooling events. *Quat. Sci. Rev.* **60**, 76–90.

Zhang X., Xu B., Günther F., Mügler I., Lange M., Zhao H., Li J. and Gleixner G. (2017) Hydrogen isotope ratios of terrestrial leaf wax n-alkanes from the Tibetan Plateau: Controls on apparent enrichment factors, effect of vapor sources and implication for altimetry. *Geochim. Cosmochim. Acta* **211**, 10–27.

Zhang Y., Renssen H. and Seppä H. (2016) Effects of melting ice sheets and orbital forcing on the early Holocene warming in the extratropical Northern Hemisphere. *Clim. Past* **12**, 1119–1135.

Appendix A

Supplementary Information Data Tables for Chapter 2

Tables A.1-A.6

Table A.1 Sedimentary wax concentrations (μg/g dry sediment) in Greenland lakes

Lake	Region	C_{20} acid	C_{22} acid	C_{24} acid	C_{26} acid	C_{28} acid	C_{30} acid	C_{21} alk	C_{23} alk	C_{25} alk	C_{27} alk	C_{29} alk	C_{31} alk	C_{33} alk	C_{23}:C_{29}
STR	Thule	0.3	0.8	1.8	1.4	1.4	0.7	0.8	1.5	1.6	2.0	1.1	0.5	0.2	1.4
WLL	Thule	2.1	6.2	7.7	5.6	3.8	1.2	2.5	5.3	8.0	10.0	4.7	1.5	0.1	1.1
NS1	Thule	0.4	0.8	0.8	0.6	0.4	0.1	0.0	0.1	0.1	0.0	0.0	0.0	0.0	1.6
SEC	Thule	0.5	0.9	1.9	0.9	0.6	0.2	1.0	2.4	2.6	3.2	2.0	1.1	0.4	1.2
USHL	Kangerlussuaq	1.2	2.3	3.0	1.6	1.0	0.4	0.2	0.3	0.2	0.2	0.4	0.4	0.1	0.9
SHL	Kangerlussuaq	0.3	0.4	0.6	0.3	0.2	0.1	0.4	0.6	0.4	0.5	0.6	0.6	0.2	0.9
RTL1	Kangerlussuaq	0.2	0.6	1.1	1.3	1.3	0.3	0.5	1.2	1.6	2.8	2.5	2.2	0.8	0.5
RTL2	Kangerlussuaq	1.3	3.8	7.4	5.4	3.5	1.3	1.3	3.3	4.7	4.7	3.4	2.3	0.9	1.0
RTL3	Kangerlussuaq	0.4	1.7	2.4	0.9	0.4	0.1	0.4	0.7	0.7	0.9	0.8	0.6	0.2	0.9
RTL4	Kangerlussuaq	3.2	9.1	20.3	7.7	5.3	2.2	3.1	9.7	5.5	7.3	6.3	1.3	0.3	1.5
RTL5	Kangerlussuaq	0.9	2.7	5.	4.30	1.9	0.9	0.7	1.9	1.7	2.1	2.4	1.0	0.3	0.8
LSL	Kangerlussuaq	1.3	2.6	4.8	3.4	2.2	0.9	0.4	1.0	1.3	1.3	1.1	0.7	0.2	1.0
LHN	Kangerlussuaq	0.2	0.5	0.9	0.6	0.3	0.1	--	--	--	--	--	--	--	--
T1	Nuuk	1.7	3.2	3.7	3.5	2.5	0.8	0.7	1.5	1.7	1.7	2.3	2.4	0.8	0.7
T2	Nuuk	2.1	4.0	5.2	4.3	2.9	0.9	0.2	0.5	0.5	0.5	0.8	1.0	0.4	0.6
T3	Nuuk	0.4	0.6	0.9	0.9	0.6	0.2	0.1	0.1	0.1	0.2	0.3	0.4	0.2	0.3
PLK	Nuuk	0.0	0.0	0.0	0.0	0.0	0.0	0.0	0.1	0.1	0.1	0.1	0.2	0.1	0.4
PIN	Narsaq	1.3	1.7	0.8	0.9	0.4	0.2	8.3	2.4	3.1	3.6	6.0	7.6	2.4	0.4
SCP	Narsaq	0.7	1.1	0.8	0.7	0.5	0.1	1.5	2.9	4.9	8.2	11.2	12.5	4.0	0.3
NAR	Narsaq	4.4	8.3	7.4	6.2	4.8	1.5	4.7	3.5	5.2	5.8	6.3	6.0	1.9	0.6
LNR	Narsaq	1.1	1.3	1.4	0.8	0.6	0.2	1.9	3.1	3.9	4.7	3.7	3.4	1.3	0.8
TUP	Narsaq	0.1	0.1	0.1	0.1	0.1	0.0	0.0	0.0	0.0	0.0	0.1	0.1	0.0	0.5
average, all lakes		1.1	2.4	3.6	2.3	1.6	0.6	1.4	2.0	2.3	2.9	2.7	2.2	0.7	0.8
average, nonglacial lakes		1.4	3.0	4.6	3.0	2.0	0.7	1.9	2.7	3.1	3.9	3.6	2.9	0.9	0.8
average, glacial lakes		0.4	0.7	0.9	0.6	0.4	0.3	0.1	0.2	0.2	0.2	0.3	0.3	0.1	0.7

Values expressed as zero here indicate concentration <0.05 but >0.00 μg/g dry sediment

Table A.2 Relative wax abundances (% contribution to sediments of total acids and total alkanes for each compound) in Greenland lakes

Lake	Region	C_{20} acid	C_{22} acid	C_{24} acid	C_{26} acid	C_{28} acid	C_{30} acid	C_{21} alk	C_{23} alk	C_{25} alk	C_{27} alk	C_{29} alk	C_{31} alk	C_{33} alk
STR	Thule	5	13	28	22	22	11	10	19	21	26	14	7	3
WLL	Thule	8	23	29	21	14	5	8	16	25	31	15	5	0
NS1	Thule	14	25	26	18	13	4	15	20	19	16	12	12	6
SEC	Thule	9	18	38	19	13	3	8	19	21	26	16	8	3
USHL	Kangerlussuaq	12	24	31	17	10	5	12	17	12	11	19	22	6
SHL	Kangerlussuaq	14	24	30	17	10	4	12	18	14	14	20	18	5
RTL1	Kangerlussuaq	5	12	23	27	27	6	4	11	14	24	22	19	7
RTL2	Kangerlussuaq	6	17	33	24	15	6	6	16	23	23	17	11	4
RTL3	Kangerlussuaq	7	29	40	16	6	2	9	17	17	20	19	14	4
RTL4	Kangerlussuaq	7	19	43	16	11	5	9	29	16	22	19	4	1
RTL5	Kangerlussuaq	6	16	34	27	11	6	7	19	17	21	24	10	3
LSL	Kangerlussuaq	8	17	32	23	14	6	7	17	22	22	18	11	3
LHN	Kangerlussuaq	9	20	34	22	11	4	--	--	--	--	--	--	--
T1	Nuuk	11	21	24	23	16	5	7	13	15	16	21	22	7
T2	Nuuk	11	21	27	22	15	5	5	12	14	14	20	26	9
T3	Nuuk	11	17	26	25	16	6	4	7	10	12	25	30	13
PLK	Nuuk	7	20	33	21	14	5	4	9	11	15	21	28	12
PIN	Narsaq	24	32	16	16	8	3	25	7	9	11	18	23	7
SCP	Narsaq	19	27	21	18	12	3	3	6	11	18	25	28	9
NAR	Narsaq	13	26	23	19	15	5	14	10	16	17	19	18	6
LNR	Narsaq	21	24	25	15	11	3	9	14	18	21	17	15	6
TUP	Narsaq	16	20	25	21	12	5	4	11	11	11	23	29	11
average, all lakes		11	21	29	20	13	5	9	15	16	19	19	17	6
average, nonglacial lakes		10	21	29	21	14	5	9	15	17	21	19	15	5
average, glacial lakes		12	22	29	20	13	5	8	13	13	13	20	23	9

Table A.3 δ^2H values (VSMOW) of Greenland sedimentary *n*-alkanes and associated measurement error

Lake	C21	C21error	C23	C23error	C25	C25error	C27	C27error	C29	C29error	C31	C31error	C33	C33error
STR	-332	4	-287	22	-251	13	-249	7	-248	6	-218	7		
WLL	-280	6	-272	6	-273	5	-274	5	-264	7	-204	21		
NS1	-243	4	-263	4	-230	5	-245	4	-235	4	-237	4	-212	4
SEC	-280	4	-273	4	-258	4	-254	4	-246	4	-234	4	-171	4
USHL	-259	5	-252	4	-238	4	-247	4	-257	4	-252	4	-235	4
SHL	-250	4	-251	4	-251	4	-239	5	-251	4	-250	4	-230	6
RTL1	-260	10	-225	5	-225	4	-230	4	-240	4	-246	4	-230	4
RTL2	-246	18	-230	5	-233	4	-232	16	-224	6	-242	7	-257	4
RTL3	-190	6	-214	4	-226	4	-226	4	-232	6	-214	4		
RTL4	-270	4	-262	4	-253	4	-256	4	-255	4	-241	4	-185	10
RTL5	-241	4	-241	4	-234	4	-250	4	-251	4	-244	4	-207	4
LSL			-233	5	-223	10	-236	4	-237	5	-224	4		
LHN														
T1	-194	5	-210	4	-212	5	-201	5	-203	4	-204	4	-192	4
T2	-223	5	-231	5	-218	4	-215	4	-218	4	-218	4	-210	5
T3			-191	5	-201	4	-207	5	-216	4	-213	4	-180	4
PLK	-160	4	-189	4	-192	6	-195	4	-206	4	-211	4	-172	4
PIN	-171	4	-191	5	-190	5	-201	4	-216	6	-215	5	-196	15
SCP	-210	4	-199	6	-205	4	-202	4	-211	4	-212	4	-201	6
NAR	-184	5	-205	7	-215	8	-211	5	-210	4	-209	5	-180	12
LNR	-215	4	-214	6	-202	5	-197	8	-203	6	-206	4	-178	6
TUP			-184	5	-181	11	-192	4	-215	4	-211	4	-184	4

Table A.4 δ^2H values (VSMOW) of Greenland sedimentary *n*-alkanoic acids and associated measurement error

Lake	C20	C20error	C22	C22error	C24	C24error	C26	C26error	C28	C28error	C30	C30error
STR			-322.4	5.3	-303.4	5.1	-242.1	5.1	-226.7	5.1	-229.6	6.7
WLL	-289.7	6.8	-295.4	5.1	-277.7	5.3	-269.9	5.9	-279.7	5.7	-263.0	7.0
NS1	-242.2	5.2	-247.0	8.2	-247.1	6.8	-243.1	5.7	-239.1	5.7		
SEC	-268.6	5.6	-294.2	5.2	-319.4	5.1	-264.1	5.1	-260.3	5.3		
USHL	-240.4	5.1	-245.7	5.4	-243.6	5.1	-241.0	5.2	-230.4	5.2	-235.4	5.1
SHL	-243.1	5.2	-242.3	5.2	-237.7	5.2	-240.5	5.2	-229.7	5.2		
RTL1	-225.1	5.3	-223.0	5.1	-226.5	5.1	-207.2	5.1	-196.1	5.2	-186.3	7.3
RTL2	-246.7	9.5	-245.1	7.0	-232.6	5.2	-209.2	5.2	-195.0	6.2	-190.5	5.1
RTL3			-191.7	5.2	-206.5	5.1	-222.0	5.6	-195.7	6.8		
RTL4	-233.0	5.1	-240.4	5.1	-253.5	5.1	-241.9	5.1	-245.7	5.1	-251.9	5.2
RTL5	-221.8	5.2	-207.9	5.2	-233.5	5.1	-234.1	5.2	-223.3	5.3	-233.4	5.2
LSL	-237.6	5.8	-220.5	5.2	-236.6	5.1	-237.2	5.1	-220.4	5.1	-213.3	5.2
LHN	-218.7	5.5	-217.3	5.6	-230.6	5.2	-218.1	5.5	-201.1	5.5	-200.8	5.5
T1	-196.5	5.2	-206.8	5.1	-204.1	5.1	-192.0	5.4	-183.2	5.2		
T2	-198.9	5.5	-209.1	5.1	-219.9	5.3	-202.6	5.1	-200.1	5.1	-202.9	5.4
T3	-193.8	5.5	-204.7	5.2	-209.0	5.2	-206.7	5.6	-201.2	5.5		
PLK												
PIN	-161.0	5.7	-169.3	5.2	-188.0	6.0	-177.2	5.2	-193.7	5.7		
SCP	-190.7	5.2	-197.0	5.1	-196.7	5.1	-187.8	5.3	-185.4	5.9		
NAR	-192.1	5.4	-202.3	5.2	-209.0	5.1	-207.7	5.1	-216.3	5.2	-208.5	5.1
LNR	-216.5	5.1	-221.5	5.1	-229.3	5.2	-198.4	5.1	-187.9	5.2		
TUP	-198.1	5.3	-194.5	6.4	-190.2	5.5	-195.6	5.1				

Table A.5 $\delta^{13}C$ values (VPDB) of Greenland sedimentary *n*-alkanes and associated measurement error

Lake	C21	C21error	C23	C23error	C25	C25error	C27	C27error	C29	C29error	C31	C31error	C33	C33error
STR	-31.1	0.9	-29.8	0.3	-31.6	0.3	-30.5	0.3	-30.6	0.6	-34.1	0.9	-39.2	0.3
WLL	-29.0	0.3	-29.1	0.2	-30.7	0.2	-30.8	0.2	-30.8	0.2	-33.1	0.4		
NS1	-37.4	0.2	-33.5	0.2	-34.4	0.3	-33.4	0.2	-34.2	0.3	-34.5	0.4	-35.9	0.2
SEC	-35.0	0.3	-34.6	0.2	-34.6	0.2	-35.0	0.2	-34.1	0.2	-34.3	0.2	-35.9	0.2
USHL														
SHL	-33.5	0.2	-33.1	0.3	-33.1	0.2	-33.1	0.2	-32.9	0.2	-32.1	0.2	-32.0	0.2
RTL1	-31.2	0.4	-27.7	0.8	-30.6	0.5	-30.5	0.5	-31.4	0.4	-32.9	0.5	-34.4	0.3
RTL2	-24.1	1.5	-23.2	1.7	-28.6	1.2	-27.4	1.1	-28.7	0.4	-32.3	0.8	-34.8	2.7
RTL3			-19.3	0.2	-22.2	0.2	-24.6	0.5	-28.8	0.4	-31.5	0.5	-35.5	0.3
RTL4	-31.5	0.2	-30.0	0.3	-33.8	0.3	-33.2	0.3	-33.9	0.2	-33.9	0.3		
RTL5	-31.4	0.3	-29.7	0.2	-29.1	0.2	-34.9	0.2	-34.4	0.2	-33.9	0.2	-35.8	0.3
LSL	-30.6	0.4	-26.6	0.5	-27.5	1.3	-27.8	0.6	-31.5	0.4	-34.0	0.5	-39.4	1.0
LHN														
T1	-34.1	0.3	-31.0	0.3	-31.7	0.3	-30.7	0.5	-30.3	0.2	-30.8	0.3	-32.0	0.3
T2														
T3														
PLK	-35.8	0.2	-32.7	0.2	-33.2	0.4	-32.0	0.2	-31.7	0.4	-31.4	0.3	-33.5	0.2
PIN	-45.4	0.2	-35.9	0.3	-37.0	0.2	-33.1	0.2	-30.7	0.2	-30.4	0.2	-30.7	0.2
SCP	-33.5	0.3	-31.3	0.2	-32.4	0.2	-31.4	0.2	-30.0	0.2	-30.0	0.3	-30.4	0.2
NAR	-39.9	0.2	-32.0	0.4	-32.5	0.9	-31.3	0.2	-30.3	0.3	-30.1	0.4	-31.7	0.4
LNR	-32.7	0.3	-30.0	0.3	-31.1	0.3	-31.2	0.2	-30.7	0.2	-31.2	0.3	-32.3	0.6
TUP	-36.0	0.5	-32.9	0.2	-34.5	0.2	-32.7	0.2	-32.5	0.2	-32.5	0.2	-34.2	0.2

Table A.6 $\delta^{13}C$ values (VPDB) of Greenland sedimentary *n*-alkanoic acids and associated measurement error

Lake	C20	C20error	C22	C22error	C24	C24error	C26	C26error	C28	C28error	C30	C30error
STR	-29.2	0.3	-30.0	0.3	-28.8	0.2	-26.7	0.6	-27.7	0.5	-27.4	0.3
WLL	2.9	0.3	-27.6	0.3	-28.5	0.3	-31.0	0.3	-32.0	0.3		
NS1	-34.5	0.3	-35.4	0.2	-32.7	0.3	-33.7	0.2	-33.0	0.2	-33.1	0.2
SEC	2.9	0.3	-35.6	0.4	-36.6	0.3	-34.8	0.3	-36.2	0.3		
USHL	-31.0	0.4	-30.8	0.3	-30.5	0.2	-31.4	0.2	-32.4	0.2		
SHL	-31.7	0.3	-31.3	0.3	-30.4	0.3	-30.9	0.5	-31.5	0.4	-32.4	0.3
RTL1			-30.3	0.3	-29.3	0.3	-28.5	0.3	-30.4	0.3	-33.2	0.3
RTL2	-27.9	0.3	-25.6	0.4	-22.8	0.3	-23.4	0.3	-25.1	0.4		
RTL3	-20.1	0.3	-17.0	0.3	-15.2	0.3	-16.4	0.3	-22.4	0.3		
RTL4	-32.9	0.3	-32.5	0.3	-30.6	0.3	-32.7	0.3	-35.2	0.3	-35.3	0.3
RTL5	-34.3	0.3	-29.9	0.3	-29.4	0.3	-27.9	0.4	-34.4	0.4		
LSL	-31.8	0.2	-28.8	0.3	-26.2	0.2	-27.0	0.2	-31.2	0.2	-32.3	0.2
LHN	-35.8	0.3	-33.3	0.3	-29.0	0.3	-30.0	0.3	-32.5	0.3	-34.2	0.4
T1	-32.4	0.3	-32.1	0.3	-30.4	0.3	-31.0	0.3	-30.2	0.3	-30.6	0.3
T2	-31.7	0.3	-31.8	0.3	-29.9	0.3	-31.4	0.2	-30.9	0.4		
T3	-31.2	0.3	-30.7	0.4	-30.3	0.3	-30.8	0.3	-31.2	0.2	-31.0	0.2
PLK												
PIN	-40.0	0.2	-39.3	0.6	-34.3	0.3	-37.0	0.4	-33.5	0.4		
SCP	-35.4	0.3	-34.3	0.3	-31.5	0.4	-33.8	0.3	-32.2	0.3		
NAR	-34.1	0.2	-33.3	0.3	-30.3	0.2	-31.2	0.4	-32.2	0.2		
LNR	-29.2	0.5	-28.8	0.4	-28.0	0.3	-29.3	0.3	-30.6	0.2	-29.2	0.2
TUP	-32.0	0.3	-31.4	0.3	-31.6	0.3	-31.3	0.3	-31.4	0.3		

Appendix B

Supplementary Information Text and Data for Chapter 3

Figures B.1-B.5

Tables B.1-B.3

Methods

Core Information. Core 14WLL-2A is 216 cm long and was split into two sections (2A-1, 2A-2) in the field for transport and storage. Cores were split and processed at the LacCore National Lacustrine Core Facility at the University of Minnesota. MS was measured every 0.3 cm using a Bartington MS2 meter and MS2E sensor mounted to a Geotek MSCL-XYZ with a sampling time of 10 s. Gamma density was measured with a ^{137}Cesium source and detector mounted to a Geotek MSCL-S every 0.5 cm with a count time of 10 s. Results from sections for which data were not recorded by the instrument or where there is clearly interference in the measurement (e.g. on core 14WLL-2A at the tube coupling where density measurements are not directly comparable due to doubled tube thickness, at the top and bottom 3 cm of each core section, 2A-1 and 2A-2, and the bottom ~5 cm of core 12WLL-1C) are not presented here (see main text, Figure 2). To assess preservation of stratigraphy in the deepest sediments, core 14WLL-2A was imaged at The Field Museum using digital x-radiography at a resolution of ca. 200 dpi (Figure S1).

Core Dating. ^{14}C ages were calibrated to cal yr BP using CALIB html version 7.1 (1) and the IntCal13 calibration curve (2) (Table S1). A live aquatic moss recovered from WLL with an Ekman dredge in 2014 yielded a post-bomb ("modern") age. Dating by optically stimulated

luminescence (OSL) was attempted, but quartz content in core material was too low for traditional OSL methods.

^{10}Be Dating. Quartz was isolated and beryllium extracted from the 250-710 μm fraction of crushed, sieved samples following methods modified from Schaefer et al. (2009) (3). Ages were calculated as described in Methods (see main text) and using time-invariant scaling (4–6) (i.e., "St" scaling; other scaling methods result in a less than 2% difference in ^{10}Be ages) (Figure S2, Table S2).

Glaciolacustrine "Gray Mud" Units. WLL sediments are organic-rich brown muds with abundant aquatic moss macrofossils, except for two discrete inorganic gray, fine-grained mud layers (one each within the Holocene and pre-LGM sediments) which have the appearance of glaciolacustrine sediments. The timing of deposition of the Holocene gray mud layer (constrained by ^{14}C to between 3.5 and 2.4 ka; see main text, Figure 2) corresponds with nearby advances between ~3.2 and 2.1 ka of Tunge and Nuna Rampen, two lobate outlet glaciers of the Greenland Ice Sheet that dammed the adjacent glacial lake Nordsø (for location of Nordsø, see Figure S2) by blocking its outlet (7). Their advance created a larger, deeper Nordsø glacial lake, evidenced by a system of higher shorelines around the modern lake Nordsø (7), and we infer that the enlarged glacial lake Nordsø temporarily flooded WLL. During this brief period of distal glaciofluvial input to WLL via Nordsø, midge assemblages were affected by greater water depth, increased turbidity and input of cold water in the summer. Therefore, we mark assemblages from this unit, and a similarly composed gray mud layer in the LIG, as not necessarily accurately recording summer air temperatures.

Midges. Midge subfossil preparation followed protocols described by Walker et al. (2001) (8). Aliquots of wet sediment (0.1-1 g) were deflocculated in 100 ml of 5% KOH at 75°C for twenty minutes. Sediment was sieved using 106 μm mesh. Head capsules and mandibles were then hand-picked from suspended bulk material in a Bogorov tray and mounted with Euparal. Midge larvae are aquatic and shed morphologically distinct chitinous head capsules during ecdysis which are often well preserved in lake sediments. Surveys of modern midge assemblages show a strong relationship between midge distribution and summer air temperature (9). Consequently, quantitative transfer functions for inferring paleotemperature from subfossil assemblages are used in many Arctic and sub-Arctic regions including North America and Scandinavia (10–14). This method may be especially well-suited for reconstructions of the late Quaternary in very high-latitude regions where soil and vegetation development, and thus secondary environmental controls, are limited (15, 16). Most relevant to this study, midges have been used to infer Holocene temperatures in several lakes in east and west Greenland (16–18) and LIG temperatures in three lakes on Baffin Island and one in Denmark (10, 19, 20).

Midge head capsules are abundant (concentrations range from ~100 to 1200 g^{-1} wet sediment) and well preserved in the sediments of WLL. Every head capsule in each sediment sample was picked and enumerated. All samples included in the study yielded a minimum of 50 identifiable, whole head capsules, the standard for quantitative analysis of assemblages (21, 22). Midges were identified to the highest degree of taxonomic certainty using the classification of Brooks et al. (2007) (23) and with Larocque and Rolland (2006) (24) also referenced. WLL subfossil assemblages contain 40 distinct morphotypes, 39 of which (representing >99% of assemblage compositions) are in the training set. After identification, some downcore taxa were lumped into larger taxonomic groups to harmonize with the lower taxonomic resolution of the training set

(10). Lumping included all members of the subtribe Tanytarsini, genera of Pentaneurini were lumped as tribe Pentaneurini, *Procladius* and *Macropelopia* were lumped together as *Procladius*-type, and all morphotypes of the following genera or groups of genera were lumped at the genus level: *Chironomus, Cricotopus*/*Orthocladius*, *Heterotrissocladius*, *Hydrobaenus*/*Oliveridia*, *Corynoneura*/*Thienemanniella*, *Eukiefferiella*/*Tvetenia*, *Zalutschia*, and *Psectrocladius*. *Chaoborus* were similarly identified to the genus level and lumped together (Figures S3, S4, S5). Up to 8% of head capsules in a subfossil community used in temperature reconstructions could not be identified (e.g. had lost morphological ornaments). One taxon, *Diamesa aberrata*, with maximum contribution to the taxonomic composition of <1%, is not represented in the Francis et al. (2006) training set and thus was not utilized in temperature reconstructions or in Figure 3 (main text). Our maximum peak early Holocene temperature estimate is derived from averaging the three consecutive temperature reconstructions between 10-8 ka and the anomaly for this period is generated by subtracting the modern (AD 1952-2014 climate norm) July air temperature value of 6.2°C (25) from that average. Our minimum peak LIG temperature estimate was similarly derived from averaging the warmest three consecutive temperature reconstructions in the unit below the hiatus, and the LIG peak anomaly was found by subtracting 6.2°C from that average.

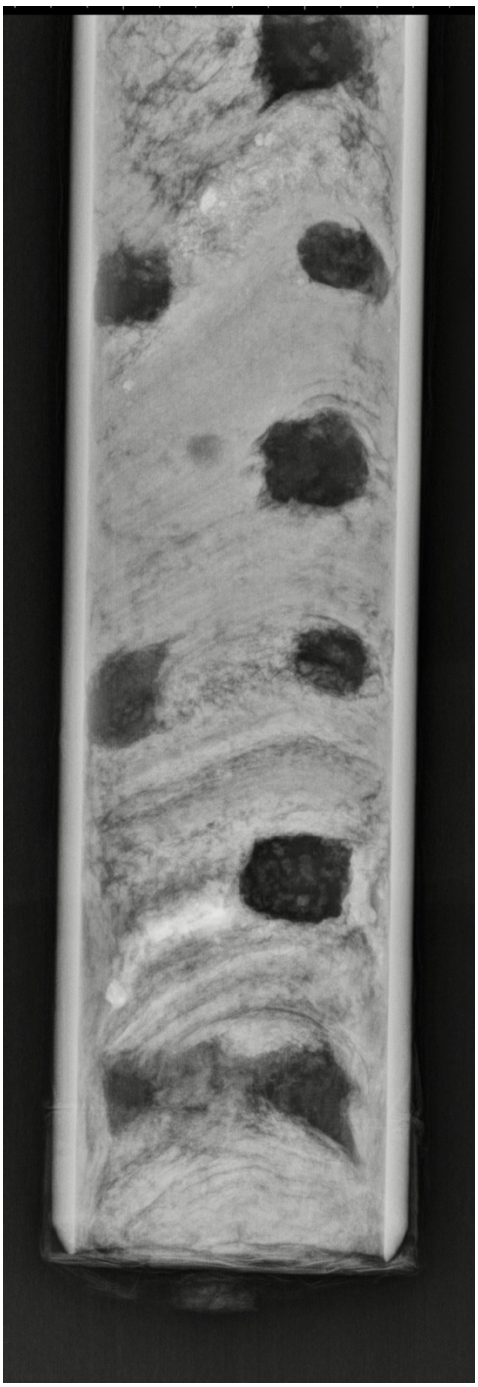

Figure B.1 *X-radiograph of sampled basal sediments of core 14WLL-2A, demonstrating the laminated nature of the deepest LIG sediments (dark areas disrupting the stratigraphy are holes created by sampling).*

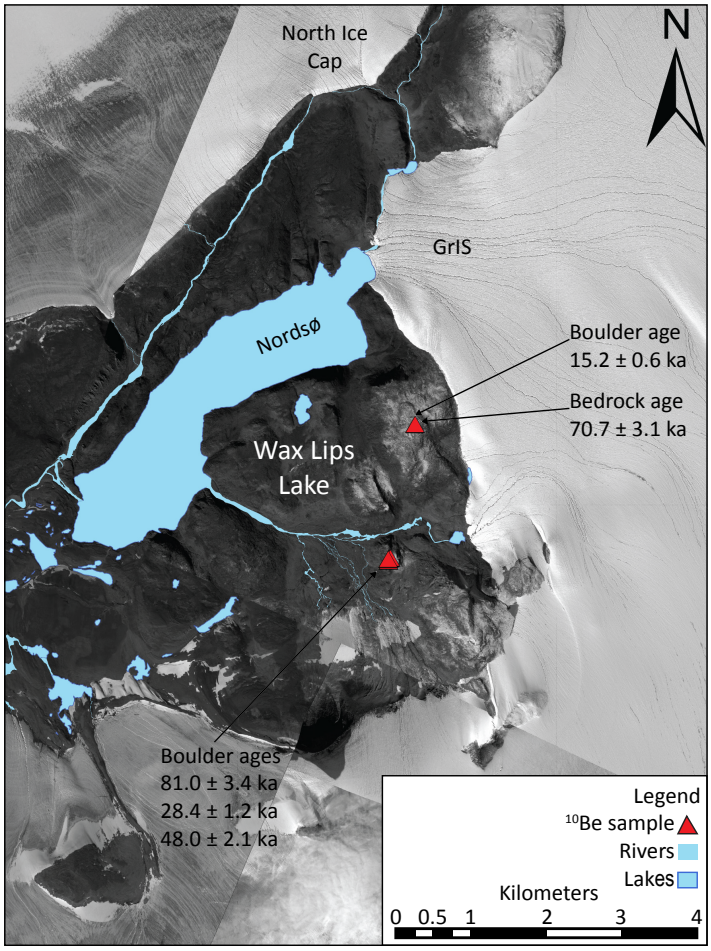

Figure B.2 *^{10}Be ages of exposed bedrock surfaces and perched boulders associated with the weathered drift surrounding WLL. Also shown are locations of WLL, the nearby glacial lake Nordsø, and the present-day GrIS. Worldview 1 and 2 satellite imagery was collected in 2010 and 2012.*

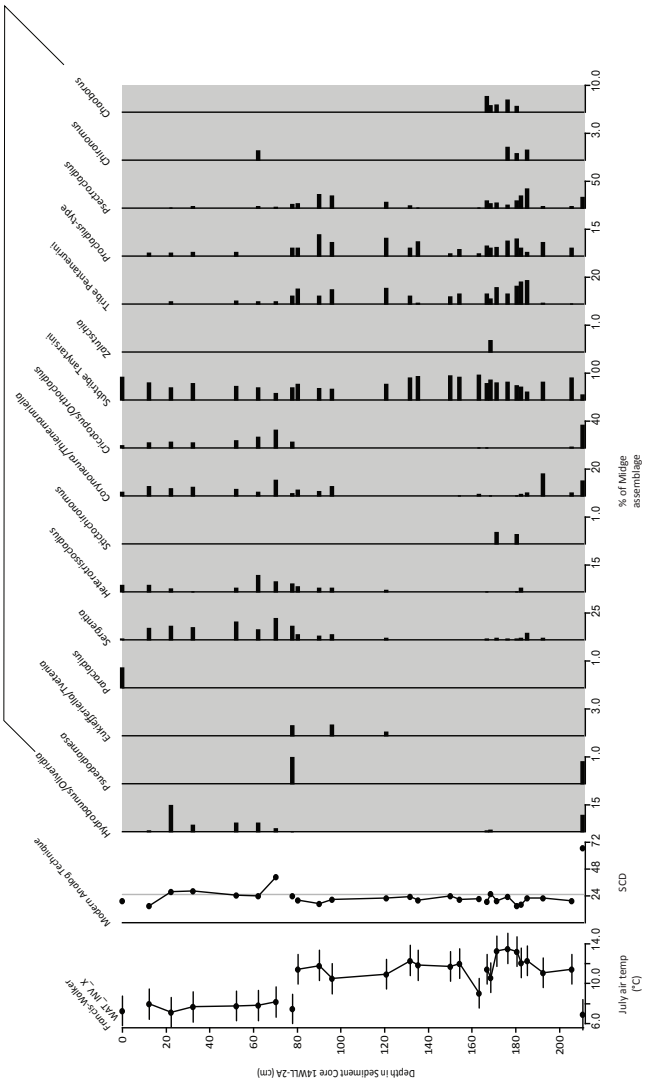

Figure B.3. *Standard biostratigraphic diagram showing modeled temperatures (modeled as described in the paper text, using C2 (26)); squared chord distances (SCD) for subfossil assemblages relative to the training set (10), with 5th percentile of the modern training set represented by gray vertical line; and percentages of enumerated taxa.*

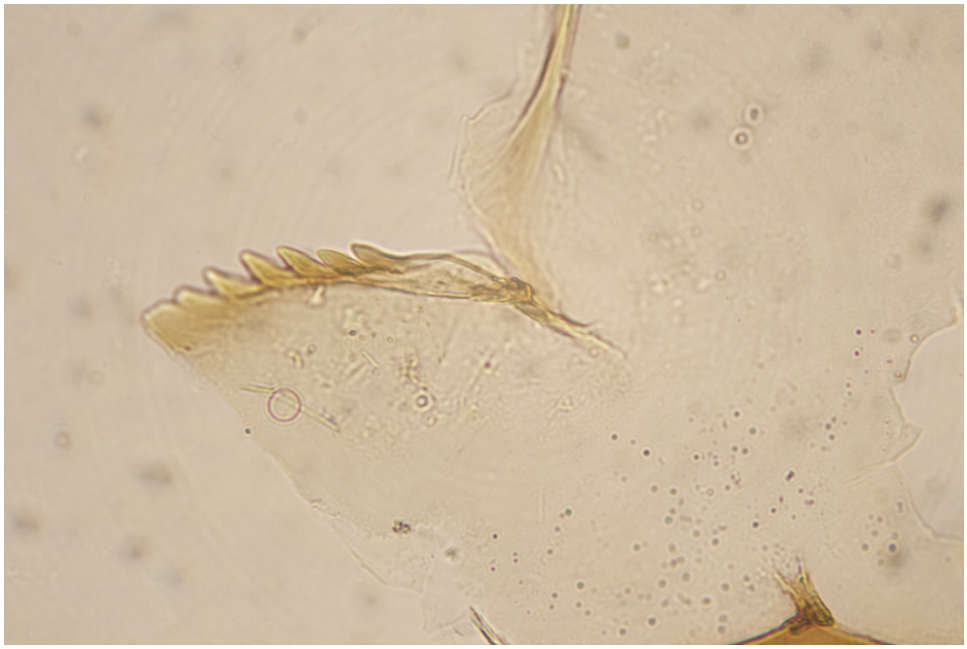

Figure B.4 *Half head capsule of Hydrobaenus/Oliveridia from Holocene sediments of WLL*

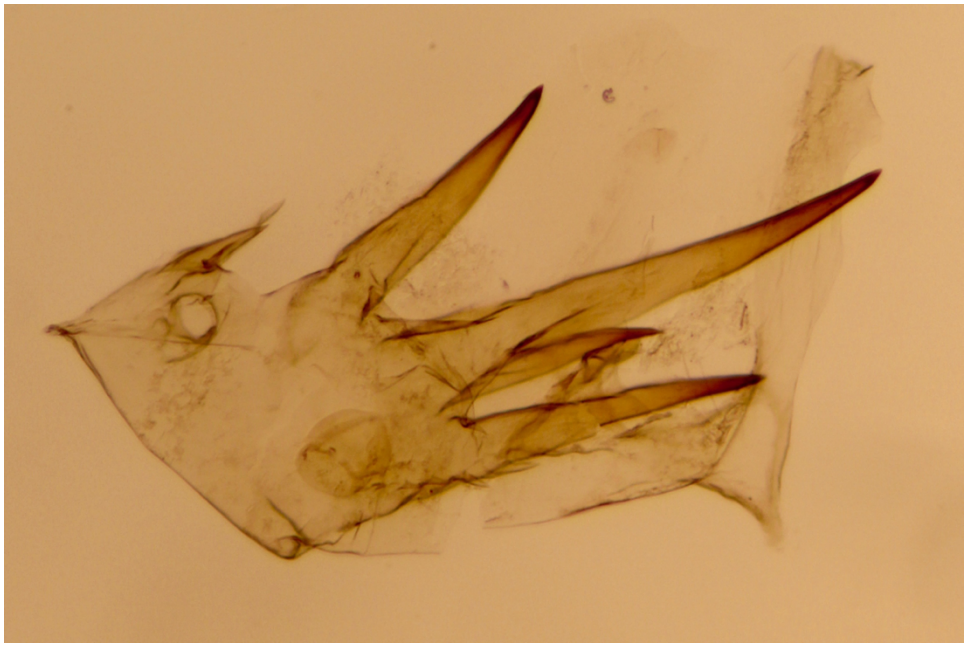

Figure B.5 *Chaoborus mandible from LIG sediments of WLL*

Table B.1 Radiocarbon ages

Targets prepared and measured at Woods Hole Oceanographic Institution and calibrated using IntCal13v7.1 (1)

Source	Material Dated	Depth in Section (cm)	Composite Core Depth (cm)	Fraction Modern	$\delta^{13}C$ (‰)	Radiocarbon Age (^{14}C yr BP)	Calibrated Age (2σ cal yr BP)
Ekman dredge							
14WLL-N1-E	Living aquatic moss			1.1685±0.0025	-24.92	>modern	modern
14WLL-U1-E2	Aquatic moss			0.9283±0.0020	-20.37	595±15	546-644
Sediment cores							
14WLL-2A-1	Aquatic moss	5-6	5.5	0.9078±0.0019	-22.01	775±15	677-726
14WLL-2A-1	Aquatic moss	24-25	24.5	0.8609±0.0017	-22.18	1200±15	1070-1177
14WLL-2A-1	Aquatic moss	47-48	47.5	0.8612±0.0017	-22.24	1200±15	1070-1177
14WLL-2A-1	Aquatic moss	56-57	56.5	0.7783±0.0017	-22.54	2010±15	1903-1995
14WLL-2A-2	Aquatic moss	5-6	70.5	0.7454±0.0023	-21.43	2360±25	2337-2458
14WLL-2A-2	Aquatic moss	29.5-30.5	95	0.6001±0.0016	-19.89	4100±20	4526-4803
14WLL-2A-2	Aquatic moss	66.5-67.5	132	0.4086±0.0016	-20.85	7190±30	7946-8049
14WLL-2A-2	Aquatic moss	93.5-94.5	159	0.3317±0.0017	-26.56	8870±40	9783-10173
14WLL-2A-2	Aquatic moss	115.5-116.5	181	0.0019±0.0021	-22.18	>44400	non-finite
14WLL-2A-2	Aquatic moss	145.5-146.5	211	-0.0005±0.0005	-21.59	>48000	non-finite
12WLL-1A	Aquatic moss	2-2.5	2.25	0.652±0.0029	-20.84	3440±35	3611-3828
12WLL-1A	Aquatic moss	14.5-15	14.75	0.5819±0.0020	-21.48	4350±25	4853-4972
12WLL-1A	Aquatic moss	22.5-23	22.75	0.3252±0.0016	-25.48	9020±40	9967-10248
12WLL-1A	Aquatic moss	40.5-41	40.75	0.4894±0.0031	-21.44	5740±50	6414-6656
12WLL-1A	Aquatic moss	44-44.5	44.25	-0.0039±0.0029	-22.23	>44200	non-finite
12WLL-1C	Aquatic moss	1.5	1.5	0.6641±0.0022	-21.2	3290±25	3457-3571
12WLL-1C	Aquatic moss	30	30	0.5332±0.0021	-23.66	5050±30	5726-5901
12WLL-1C	Aquatic moss	45.5	45.5	0.4286±0.0025	-22.36	6810±45	7578-7718
12WLL-1C	Aquatic moss	50	50	0.0265±0.0016	-23.63	29200±470	32735-33919
12WLL-1C	Aquatic moss	54.5	54.5	0.0028±0.0008	-23.42	47300±2200	non-finite

Table B.2 ^{10}Be ages of samples of bedrock and boulders associated with weathered drift

[a]Samples were measured with beryllium standard 07KNSTD (Nishiizumi et al., 2007) (27)

[b]Uncertainty is internal AMS uncertainty

*Sample taken from bedrock

	Lat. (ºN)	Long. (ºW)	Elevation (m a.s.l.)	Thickness (cm)	Shielding Correction	^{10}Be Conc.[a] (atoms/g)	Uncertainty[b] (atoms/g)	Age ± uncertainty
NT-14-1	76.8389	-66.887	618	4.48	0.999	3.65E+05	6.59E+03	48,040 ± 2050
NT-14-2	76.8391	-66.8861	614	4.43	0.995	6.06E+05	1.01E+04	80,970 ± 3440
NT-14-4	76.8387	-66.8864	614	5.69	0.999	2.14E+05	4.17E+03	28,410 ± 1230
NT-14-5	76.8552	-66.9005	722	5.77	1	1.27E+05	2.24E+03	15,170 ± 640
NT-14-6*	76.8552	-66.9005	722	2.75	1	5.98E+05	1.16E+04	70,670 ± 3080

Table B.3 WLL core locations

Core	Coring system	Lat. (ºN)	Long. (ºW)	Water depth at core site (m)	Core length (m)
12WLL-1A	Modified-Bolivia	76.85205	-66.9598	8.25	0.70
12WLL-1C	Modified-Bolivia	76.85212	-66.9595	8.20	0.67
14WLL-2A	Nesje	76.85184	-66.9592	7.19	2.16

References

1. Stuiver M, Reimer PJ, Reimer RW (2017) CALIB 7.1 [WWW program]. Available at: http://calib.org [Accessed May 1, 2017].
2. Reimer PJ, et al. (2013) IntCal13 and Marine13 radiocarbon age calibration curves 0–50,000 Years cal BP. *Radiocarbon* 55(4):1869–1887.
3. Schaefer JM, et al. (2009) High-frequency Holocene glacier fluctuations in New Zealand differ from the northern signature. *Science* 324(5927):622–625.
4. Balco G, Stone JO, Lifton NA, Dunai TJ (2008) A complete and easily accessible means of calculating surface exposure ages or erosion rates from ^{10}Be and ^{26}Al measurements. *Quat Geochronol* 3:174–195.
5. Lal D (1991) Cosmic ray labeling of erosion surfaces: in situ nuclide production rates and erosion models. *Earth Planet Sci Lett* 104:424–439.
6. Stone JO (2000) Air pressure and cosmogenic isotope production. *J Geophys Res* 105(B10):23753–23759.
7. Farnsworth LB, et al. (2018) Holocene history of the Greenland Ice Sheet margin in northern Nunatarssuaq, northwest Greenland. *Arktos J Arct Geosci* 4:10. doi: 10.1007/s41063-018-0044-0
8. Walker IR (2001) Midges: Chironomidae and Related Diptera. *Tracking Environmental Change Using Lake Sediments. Volume 4: Zoological Indicators*, eds Smol JP, Birks HJB, Last WM (Kluwer Academic Publishers, Dordrecht, The Netherlands), pp 43–66.
9. Walker IR, Levesque AJ, Cwynar LC, Lotter AF (1997) An expanded surface-water palaeotemperature inference model for use with fossil midges from eastern Canada. *J Paleolimnol* 18(2):165–178.
10. Francis DR, Wolfe AP, Walker IR, Miller GH (2006) Interglacial and Holocene

temperature reconstructions based on midge remains in sediments of two lakes from Baffin Island, Nunavut, Arctic Canada. *Palaeogeogr Palaeoclimatol Palaeoecol* 236(1–2):107–124.

11. Barley EM, et al. (2006) A northwest North American training set: distribution of freshwater midges in relation to air temperature and lake depth. *J Paleolimnol* 36(3):295–314.
12. Fortin M-C, et al. (2015) Chironomid-environment relations in northern North America. *J Paleolimnol* 54(2–3):223–237.
13. Langdon PG, Holmes N, Caseldine CJ (2008) Environmental controls on modern chironomid faunas from NW Iceland and implications for reconstructing climate change. *J Paleolimnol* 40(1):273–293.
14. Brooks SJ (2006) Fossil midges (Diptera: Chironomidae) as palaeoclimatic indicators for the Eurasian region. *Quat Sci Rev* 25(15–16):1894–1910.
15. Brooks SJ, Axford Y, Heiri O, Langdon PG, Larocque-Tobler I (2012) Chironomids can be reliable proxies for Holocene temperatures. A comment on Velle et al. (2010). *The Holocene* 22(12):1495–1500.
16. Axford Y, et al. (2017) Timing and magnitude of early to middle Holocene warming in East Greenland inferred from chironomids. *Boreas* 46(4):678–687.
17. Axford Y, et al. (2013) Holocene temperature history at the western Greenland Ice Sheet margin reconstructed from lake sediments. *Quat Sci Rev* 59:87–100.
18. Wooller MJ, et al. (2004) Quantitative paleotemperature estimates from $\delta^{18}O$ of chironomid head capsules preserved in arctic lake sediments. *J Paleolimnol* 31(3):267–274.
19. Axford Y, et al. (2011) Chironomids record terrestrial temperature changes throughout

Arctic interglacials of the past 200,000 yr. *Bull Geol Soc Am* 123(7–8):1275–1287.

20. Jones RT, et al. (2017) Delayed maximum northern European summer temperatures during the Last Interglacial as a result of Greenland Ice Sheet melt. *Geology* 45(1):23–26.
21. Heiri O, Lotter AF (2001) Effect of low count sums on quantitative environmental reconstructions: an example using subfossil chironomids. *J Paleolimnol* 26(3):343–350.
22. Larocque I (2001) How many chironomid head capsules are enough? A statistical approach to determine sample size for palaeoclimatic reconstructions. *Palaeogeogr Palaeoclimatol Palaeoecol* 172(1–2):133–142.
23. Brooks SJ, Langdon PG, Heiri O (2007) *The Identification and Use of Palaearctic Chironomidae Larvae in Palaeoecology* (Quaternary Research Assocation, London, UK).
24. Larocque I, Rolland N (2006) *A Visual Guide to Sub-fossil Chironomids from Quebec to Ellesmere Island* (Institut National de la Recherche Scientifique, Québec).
25. Wong GJ, et al. (2015) Coast-to-interior gradient in recent northwest Greenland precipitation trends (1952–2012). *Environ Res Lett* 10(11):114008.
26. Juggins S (2007) C2 Version 1.7.7: software for ecological and paleoecological data analysis and visualisation.
27. Nishiizumi K, et al. (2007) Absolute calibration of ^{10}Be AMS standards. *Nucl Instruments Methods Phys Res Sect B Beam Interact with Mater Atoms* 258(2):403–413.

Appendix C

Supplementary Information Data Tables for Chapter 4

Tables C.1 – C.5

Table C.1 Concentration (ug/g dry sediment) of sedimentary *n*-alkanes in 14WLL2A by depth

Depth	Median Age	C_{21}	C_{23}	C_{25}	C_{27}	C_{29}	C_{31}	C_{23}:C_{29}	C_{23}:C_{27}	P_{aq}
9	780	2.2	5.0	6.2	7.3	3.7	1.7	1.3	0.7	0.7
14	890	3.1	6.0	6.5	7.9	4.2	1.8	1.4	0.8	0.7
19	995	-	-	-	-	-	-	-	-	-
24	1079	2.9	5.9	5.7	7.3	3.5	1.9	1.7	0.8	0.7
***29**	1119	3.1	7.1	5.6	7.7	3.3	1.6	2.2	0.9	0.7
***39**	1180	3.8	8.2	6.0	8.5	3.4	1.7	2.4	1.0	0.7
44	1210	-	-	-	-	-	-	-	-	-
***49**	1276	6.3	16.3	11.8	13.8	5.5	2.2	3.0	1.2	0.8
***54**	1792	1.6	7.3	5.5	6.1	3.1	1.5	2.4	1.2	0.7
***59**	2055	2.2	7.5	6.2	7.0	3.0	1.3	2.5	1.1	0.8
68.5	2347	2.6	4.5	4.2	5.0	3.6	3.0	1.2	0.9	0.6
75.5	2824	0.4	0.8	0.8	0.9	0.6	0.4	1.3	0.9	0.6
80.5	3282	5.8	9.2	9.1	14.1	5.1	1.5	1.8	0.7	0.7
85.5	3831	7.5	11.4	11.9	17.5	7.2	2.3	1.6	0.7	0.7
95.5	4657	6.0	9.0	9.6	13.4	5.7	1.7	1.6	0.7	0.7
99.5	4999	7.0	11.8	14.6	21.7	9.6	2.6	1.2	0.5	0.7
105.5	5572	5.5	9.3	10.8	15.7	6.8	2.1	1.4	0.6	0.7
115.5	6526	8.4	9.2	6.4	10.9	4.5	1.5	2.0	0.9	0.7
125.5	7498	9.5	9.8	9.4	18.4	6.5	1.5	1.5	0.5	0.7
***135.5**	8286	4.8	12.1	7.3	12.8	5.2	1.8	2.3	0.9	0.7
***145.5**	9028	7.6	14.5	6.7	9.7	3.9	1.1	3.7	1.5	0.8
***155.5**	9756	3.3	11.5	7.1	8.7	4.7	1.3	2.5	1.3	0.8
***160.5**	9902	5.0	14.5	11.0	15.1	5.8	1.6	2.5	1.0	0.8
***164.5**	LIG	8.3	27.5	26.0	15.2	7.0	2.9	3.9	1.8	0.8
***169.5**	LIG	8.9	28.6	25.6	14.3	7.0	3.3	4.1	2.0	0.8
175.5	LIG	-	-	-	-	-	-	-	-	-
180	LIG	-	-	-	-	-	-	-	-	-
185.5	LIG	3.0	7.8	5.3	11.4	6.6	2.6	1.2	0.7	0.6
189.5	LIG	5.7	12.2	10.8	11.2	6.6	4.3	1.8	1.1	0.7
***195.5**	LIG	7.5	15.0	10.6	11.7	7.2	4.5	2.1	1.3	0.7
***199.5**	LIG	9.9	30.8	19.9	26.2	12.9	8.9	2.4	1.2	0.7
205.5	LIG	2.6	7.2	7.9	9.9	5.5	2.8	1.3	0.7	0.6
209.5	LIG	6.6	15.3	25.7	39.1	19.9	5.2	0.8	0.4	0.6
215.5	LIG	5.6	13.3	29.3	43.8	21.7	4.6	0.6	0.3	0.6

*indicates samples where the C23:C29 ratio is >2 and the C23:C27 ratio is >1 . These samples are not used for inferring terrestrial leaf water

Table C.2 Hydrogen isotope values relative to VSMOW of sedimentary *n*-alkanes from WLL by depth

Depth	Median Age	C_{21}	C_{23}	C_{25}	C_{27}	C_{29}	C_{31}
0	600	-224.2	-278.1	-278.6	-278.1	-270.1	-203.2
9	780	-164.2	-204.9	-347.3	-201.9	-173.4	-132.6
14	890	-247.8	-254.7	-231.1	-230.1	-209.7	-150.7
19	995	-267.9	-288.5	-249.1	-232.2	-221.8	-179.2
24	1079	-260.7	-279.2	-252.6	-238.2	-219.5	-168.3
29	1119	-199.5	-200.3	-170.4	-135.3	-96.2	-74.3
39	1180	-285.4	-272.4	-247.7	-237.3	-228.4	-201.8
44	1210	-236.6	-246.0	-217.1	-213.5	-193.5	-165.8
49	1276	-260.9	-244.1	-218.7	-204.6	-198.1	-141.7
54	1792	-260.3	-247.1	-232.2	-222.6	-200.7	-167.6
59	2055	-244.1	-245.7	-229.6	-226.7	-207.8	-169.8
68.5	2347	-248.1	-236.8	-214.7	-203.6	-177.7	-152.3
75.5	2824	-225.1	-241.1	-233.6	-222.5	-215.8	-194.6
80.5	3282	-329.7	-306.5	-271.7	-267.4	-256.3	-178.0
85.5	3831	-328.8	-308.0	-281.9	-274.5	-264.6	-214.9
95.5	4657	-334.8	-308.8	-283.4	-277.2	-267.7	-194.8
100.5	5085	-273.6	-271.9	-254.2	-253.8	-236.5	-167.8
105.5	5572	-319.1	-301.7	-282.3	-278.1	-271.2	-222.4
115.5	6526	-356.5	-314.9	-256.2	-244.9	-232.4	-191.1
125.5	7498	-360.3	-300.8	-246.2	-234.0	-228.7	-191.3
135.5	8286	-313.1	-310.0	-252.6	-243.5	-234.7	-201.3
145.5	9028	-362.2	-346.2	-255.3	-241.4	-246.9	-206.1
155.5	9756	-329.7	-320.8	-262.8	-259.5	-268.7	-220.8
160.5	9902	-285.1	-272.5	-239.8	-241.7	-240.1	-220.8
164.5	LIG	-290.0	-257.4	-233.6	-232.9	-227.4	-176.8
166.5	LIG	-305.0	-255.5	-229.3	-234.6	-238.6	-223.7
169.5	LIG	-298.0	-254.1	-232.1	-234.7	-235.3	-208.0
175.5	LIG	-253.2	-254.8	-229.6	-232.5	-235.7	-231.9
180.5	LIG	-266.0	-304.0	-250.6	-258.5	-250.3	-223.7
185.5	LIG	-278.3	-317.7	-253.9	-281.4	-283.9	-253.4
189.5	LIG	-260.9	-267.7	-252.1	-259.4	-231.8	-201.9
195.5	LIG	-321.4	-297.3	-273.2	-275.2	-268.0	-237.5
199.5	LIG	-139.1	-243.5	-276.1	-296.2	-237.1	-307.3

205.5	LIG	-267.5	-277.3	-268.9	-275.3	-274.1	-241.8
209.5	LIG	-286.4	-295.9	-289.3	-295.9	-293.3	-242.9
215.5	LIG	-297.1	-302.0	-305.3	-318.1	-307.7	-244.5

Table C.3 Carbon isotope values relative to VPDB of sedimentary *n*-alkanes from WLL by depth

Depth	Median Age	C_{21}	C_{23}	C_{25}	C_{27}	C_{29}	C_{31}
0	600	-28.99	-28.9	-30.7	-30.75	-30.07	-33.26
14	890	-30.2	-28.35	-29.95	-30.14	-30.36	-37.05
19	995	-30.32	-28.69	-30.22	-32.42	-31.3	-36.35
24	1079	-29.76	-28.16	-29.94	-29.77	-30.66	-34.55
29	1119	-29.53	-27.64	-29.74	-29.68	-30.37	-35.54
36	1162	-29.24	-28.03	-28.68	-29.37	-29.38	-31.83
39	1180	-27.51	-26.71	-28.96	-28.5	-30.23	-33.99
44	1210	-28.13	-27.24	-29.26	-29.01	-32.74	-35.12
49	1276	-28.27	-27.17	-29.38	-30.76	-31.71	-34.44
54	1792	-29.27	-27.69	-29.73	-29.88	-30.62	-31.17
59	2055	-30.01	-27.92	-29.93	-29.91	-32.45	-33.07
68.5	2347	-31.53	-29.22	-29.73	-29.39	-29.49	-29.42
75.5	2824	-36.97	-32.74	-32.8	-33.39	-33.43	-32.72
80.5	3282	-29.5	-28.44	-29.47	-29.75	-30.41	-31.92
85.5	3831	-29.71	-28.33	-28.99	-29.26	-29.93	-32.42
95.5	4657	-28.91	-27.76	-28.59	-29.17	-29.47	-31.61
105.5	5572	-28.53	-27.51	-28.89	-29.06	-29.71	-31.34
115.5	6526	-30.93	-28.58	-28.67	-30.06	-30.16	-31.52
125.5	7498	-30.39	-28.57	-28.72	-29.9	-29.9	-31.64
135.5	8286	-28.47	-28.04	-29.16	-29.16	-29.95	-32.19
145.5	9028	-27.69	-27.53	-26.27	-28.29	-28.48	-31.86
155.5	9756	-28.16	-26.49	-26.72	-28.73	-28.77	-32.55
160.5	9902	-26.89	-25.86	-27.24	-28.15	-29.69	-32.34
164.5	LIG	-27.37	-24.39	-25.74	-27.99	-29.72	-32.32
166.5	LIG	-27.66	-24.78	-26.25	-28.46	-29.12	-30.88
169.5	LIG	-27.59	-24.91	-26.31	-28.36	-30.33	-32.45
175.5	LIG	-25.59	-25.46	-26.62	-28.35	-29.58	-30.79
182.5	LIG	-24.45	-24.34	-28.04	-28.38	-29.08	-31.45
185.5	LIG	-24.24	-23.63	-27.68	-28.9	-29.81	-31.68
189.5	LIG	-30.97	-31.25	-32.52	-33.03	-34.37	-34.76
195.5	LIG	-31.1	-31.75	-32.73	-32.23	-32.97	-33.23
199.5	LIG	-31.67	-32.35	-33.49	-32.95	-33.41	-32.66
205.5	LIG	-31.47	-30.65	-31.94	-31.09	-31.91	-32.79

209.5	LIG	-28.02	-27.97	-31.86	-31.94	-32.87	-34.93
215.5	LIG	-25.97	-27.1	-31.69	-31.43	-31.85	-32.96

Table C.4 Oxygen isotope values relative to VSMOW of chironomid chitin by depth, and calculated hydrogen isotope values using the global meteoric water line (GMWL) and a local evaporation line (LEL)

Depth	Age	$\delta^{18}O_{chiron}$	$\delta^{18}O_{lake/precip}$	$\delta^{2}H_{precip}$ (GMWL)	$\delta^{2}H_{precip}$ (LEL)
0	600	4.59	-17.71	-131.7	-142.4
19	995	4.68	-17.62	-131.0	-141.9
29	1119	2.94	-19.36	-144.9	-151.5
39	1180	3.15	-19.15	-143.2	-150.3
49	1276	2.85	-19.45	-145.6	-152.0
59	2055	2.81	-19.49	-145.9	-152.2
81	3333	3.52	-18.78	-140.2	-148.3
91	4342	1.85	-20.45	-153.6	-157.5
101	5132	2.21	-20.09	-150.7	-155.5
111	6098	3.69	-18.61	-138.9	-147.4
121	7080	1.62	-20.68	-155.4	-158.7
131	7948	2.82	-19.48	-145.8	-152.1
141	8697	2.83	-19.47	-145.8	-152.1
151	9434	2.96	-19.34	-144.7	-151.4
161	9975	3.42	-18.88	-141.0	-148.8
168.25	LIG	7.39	-14.91	-109.3	-127.0
171	LIG	4.91	-17.39	-129.1	-140.6
176	LIG	6.62	-15.68	-115.4	-131.2
181	LIG	5.16	-17.14	-127.1	-139.3
186	LIG	5.28	-17.02	-126.2	-138.6
191	LIG	4.23	-18.07	-134.6	-144.4
196	LIG	6.69	-15.61	-114.9	-130.9
201	LIG	3	-19.3	-144.4	-151.2
206	LIG	6.48	-15.82	-116.6	-132.0
211	LIG	3.23	-19.07	-142.6	-149.9

Table C.5. Calculation of leaf water hydrogen isotopic composition from biomarker hydrogen isotopic composition using calibrated data (C_{29}-MAP apparent fractionation) from Chapter 2

Depth	Median Age	δ^2H_{C23}	$\delta^2H_{C23\text{-}MAP}$	$\delta^2H_{C23\text{-}JJA}$	δ^2H_{C29}	δ^2H_{leaf}
0	600	-278.1	-194.0	-126.9	-270.1	-171.5
9	780	-204.9	-112.7	-70.6	-173.4	-61.8
14	890	-254.7	-168.0	-108.9	-209.7	-102.9
19	995	-288.5	-205.5	-134.9	-221.8	-116.6
24	1079	-279.2	-195.2	-127.8	-219.5	-114.1
29	1119	-200.3	-107.6	-67.1	-96.2	25.9
39	1180	-272.4	-187.6	-122.5	-228.4	-124.2
44	1210	-246.0	-158.3	-102.2	-193.5	-84.5
49	1276	-244.1	-156.3	-100.8	-198.1	-89.8
54	1792	-247.1	-159.5	-103.0	-200.7	-92.7
59	2055	-245.7	-158.0	-102.0	-207.8	-100.8
68.5	2347	-236.8	-148.1	-95.1	-177.7	-66.6
75.5	2824	-241.1	-152.9	-98.5	-215.8	-109.8
80.5	3282	-306.5	-225.5	-148.7	-256.3	-155.8
85.5	3831	-308.0	-227.2	-149.9	-264.6	-165.3
95.5	4657	-308.8	-228.1	-150.5	-267.7	-168.8
100.5	5085	-271.9	-187.2	-122.2	-236.5	-133.4
105.5	5572	-301.7	-220.2	-145.0	-271.2	-172.8
115.5	6526	-314.9	-234.9	-155.2	-232.4	-128.8
125.5	7498	-300.8	-219.2	-144.4	-228.7	-124.5
135.5	8286	-310.0	-229.5	-151.5	-234.7	-131.3
145.5	9028	-346.2	-269.7	-179.3	-246.9	-145.2
155.5	9756	-320.8	-241.4	-159.8	-268.7	-169.9
160.5	10000	-272.5	-187.8	-122.6	-240.1	-137.5
164.5	LIG	-257.4	-171.0	-111.0	-227.4	-123.1
166.5	LIG	-255.5	-168.9	-109.5	-238.6	-135.8
169.5	LIG	-254.1	-167.3	-108.4	-235.3	-132.0
175.5	LIG	-254.8	-168.1	-109.0	-235.7	-132.4
180.5	LIG	-304.0	-222.7	-146.8	-250.3	-149.1
185.5	LIG	-317.7	-238.0	-157.4	-283.9	-187.2
189.5	LIG	-267.7	-182.4	-118.9	-231.8	-128.1
195.5	LIG	-297.3	-215.3	-141.7	-268.0	-169.2
199.5	LIG	-243.5	-155.5	-100.3	-237.1	-134.0

205.5	LIG	-277.3	-193.1	-126.3	-274.1	-176.1
209.5	LIG	-295.9	-213.8	-140.6	-293.3	-197.8
215.5	LIG	-302.0	-220.6	-145.3	-307.7	-214.2

Appendix D

Supplementary Information Data Table for Chapter 5

Tables D.1 – D.4

Table D.1 Radiocarbon ages of organic material from Pincushion Lake cores U11 and U2 (sections A and B)

Source	Material Dated	Section Depth (cm)	Composite Core Depth (cm)	Fraction Modern	$\delta^{13}C$ (‰)	^{14}C Age (yr BP)	Calibrated 2-sigma age (cal yr BP)	Median Age (cal yr BP)
surface	Aq. moss		0	1.0409 ± 0.0021	-23.65	modern		-66
U11	Terr.	6-7	6-7	0.8498 ± 0.0017	-25.7	1,310 ± 15	1186-1288	1268
U11	Terr.	16-17	16-17	0.7349 ± 0.0017	-25.54	2,480 ± 20	2473-2715	2589
U11	Misc.	25-26	25-26	0.6190 ± 0.0018	-25.56	3,850 ± 25	4156-4406	4269
U11	Misc.	40-41	40-41	0.4916 ± 0.0064	-24.88	5,710 ± 110	6297-6737	6512
U11	Terr.	53-54	53-54	0.4130 ± 0.0018	-26.57	7,100 ±35	7851-7996	7937
U11	Misc.	65-66	65-66	0.3913 ± 0.0055	-26.78	7,540 ± 110	8063-8580	8343
U11	Misc.	78-79	78-79	0.4595 ± 0.0019	-26.05	6,250 ± 30	7027-7259	7201
U11	Aq. moss	98-99*	86.15-86.23	0.3293 ± 0.0015	-26.83	8,920 ± 35	9915-10189	10041
U11	Aq. moss	98-99*	86.15-86.23	0.3274 ± 0.0019	-27.22	8,970 ± 45	9919-10232	10147
U2A	Aq. moss	83-84	79-80	0.3378 ± 0.0020	-25.66	8,720 ± 45	9550-9887	9676
U2A	Aq. moss	92-93	88-89	0.3106 ± 0.0020	-27.34	9,390 ± 50	10500-10741	10622
U2A	Aq. moss	104-105	100-101	0.3854 ± 0.0018	-28	7,660 ± 40	8394-8539	8449
U2A	Aq. moss	113-114	109-110	0.3029 ± 0.0020	-24.95	9,590 ± 50	10742-11143	10937
U2B	Aq. moss	2-3	124.5-125.5	0.3193 ± 0.0021	-25.6	9,170 ± 50	10234-10489	10336

**These sample results were combined to create a single point for the age-depth model*

Table D.2 Concentration (ug/g dry sediment) of sedimentary *n*-alkanes in 16SWL (Pincushion Lake) Composite Core by depth

Depth	Median Age	C_{21}	C_{23}	C_{25}	C_{27}	C_{29}	C_{31}	C_{33}	C_{23}:C_{29}	C_{23}:C_{27}	P_{aq}
0	0	22.9	5.3	6.2	7.8	12.5	12.8	4.1	0.4	0.7	0.3
2.5	514	18.9	6.4	8.4	10.6	18.8	18.9	5.4	0.3	0.6	0.3
5.5	1171	13.8	6.6	8.8	10.0	19.0	19.6	5.8	0.4	0.7	0.3
10.5	1923	13.1	5.7	6.4	8.5	17.0	18.5	5.6	0.3	0.7	0.3
15.5	2498	14.3	5.4	6.1	9.2	20.7	21.6	6.3	0.3	0.6	0.2
20.5	3421	5.8	5.5	7.1	9.4	21.6	23.4	7.3	0.3	0.6	0.2
25.5	4353	28.6	28.6	32.1	44.3	90.5	104.5	36.0	0.3	0.7	0.2
30.5	5204	5.2	5.3	7.1	8.4	16.7	18.3	6.2	0.3	0.6	0.3
35.5	5907	13.6	20.2	23.9	26.0	54.0	61.4	21.5	0.4	0.8	0.3
41.5	6713	3.3	5.0	8.1	7.7	16.4	19.6	6.7	0.3	0.7	0.3
42.5	6835	4.8	7.1	9.4	10.5	20.6	23.0	7.8	0.4	0.7	0.3
45.5	7195	15.7	26.3	32.4	35.7	79.6	93.7	34.2	0.3	0.7	0.3
50.5	7743	2.1	3.1	4.0	4.0	8.9	9.9	3.4	0.3	0.8	0.3
60.5	8308	2.9	4.5	4.7	5.6	9.6	9.4	3.8	0.5	0.8	0.3
65.5	8504	10.1	17.2	17.0	20.6	31.6	40.1	27.2	0.6	0.8	0.3
70.5	8856	2.6	4.1	4.5	5.6	10.1	12.0	7.3	0.4	0.7	0.3
75.5	9328	7.0	13.3	13.2	19.0	38.1	49.8	38.2	0.4	0.7	0.2
80.5	9805	0.6	1.1	1.9	1.8	4.2	4.0	1.3	0.3	0.7	0.3
88.5	10247	4.0	10.4	14.5	18.7	20.8	13.9	4.9	0.5	0.6	0.4
93.5	10513	0.9	1.7	2.7	3.4	3.9	2.8	1.0	0.4	0.5	0.4
99.5	10741	1.3	3.3	5.2	6.8	8.0	5.9	2.0	0.4	0.5	0.4
104.5	10894	1.6	2.9	2.9	3.6	11.1	5.8	1.6	0.3	0.8	0.3
108	11000	1.4	2.9	3.4	3.7	4.6	2.9	0.8	0.6	0.8	0.5
113.5	11227	0.9	1.7	2.2	2.0	2.3	1.5	0.4	0.8	0.9	0.5
124.5	11770	1.7	3.8	2.3	1.9	1.2	0.5	0.2	3.2	2.0	0.8
128.5	12092	0.2	0.3	0.3	0.2	0.2	0.2	0.1	1.5	1.6	0.6
132.5	12464	0.2	0.2	0.3	0.1	0.1	0.1	0.0	2.5	2.1	0.8

Table D.3 Hydrogen isotope values relative to VSMOW of sedimentary *n*-alkanes from 16SWL (Pincushion Lake) Composite Core by depth

Depth	Median Age	C_{21}	C_{23}	C_{25}	C_{27}	C_{29}	C_{31}	C_{33}
0	0	-167.5	-189.2	-193.8	-197.8	-215.5	-214.5	-197.4
2.5	514	-174.4	-188.0	-193.9	-204.5	-218.6	-215.9	-196.9
5.5	1171	-180.8	-193.2	-190.2	-198.7	-215.9	-215.3	-195.1
10.5	1923	-182.4	-188.4	-186.3	-200.5	-217.1	-215.7	-200.2
15.5	2498	-177.2	-188.4	-187.0	-195.8	-213.0	-213.1	-192.9
20.5	3421	-192.9	-195.4	-192.3	-198.8	-215.9	-216.4	-195.9
25.5	4353	-185.2	-206.5	-198.8	-204.4	-220.5	-215.6	-203.8
30.5	5204	-193.0	-196.8	-189.5	-201.5	-217.7	-217.0	-217.1
35.5	5907	-189.8	-199.7	-195.3	-195.9	-212.9	-212.5	-199.9
41.5	6713	-188.7	-199.6	-194.4	-201.2	-215.0	-215.5	-199.8
42.5	6835	-190.9	-201.3	-192.1	-201.9	-216.3	-215.0	-202.8
45.5	7195	-193.6	-204.2	-192.6	-202.4	-214.9	-215.1	-199.5
50.5	7743	-194.0	-204.8	-182.2	-191.8	-211.4	-210.5	-190.4
60.5	8308	-231.4	-210.0	-204.2	-206.1	-214.0	-211.8	-203.1
65.5	8504	-232.9	-214.4	-187.1	-199.2	-211.9	-210.1	-194.7
70.5	8856	-225.2	-222.6	-195.5	-202.5	-210.3	-212.3	-211.3
75.5	9328	-226.4	-226.3	-194.6	-208.3	-213.8	-213.9	-206.1
80.5	9805	-216.5	-228.1	-205.7	-214.9	-218.5	-211.5	-216.0
88.5	10247	-187.8	-184.2	-182.5	-201.2	-212.8	-208.2	-188.9
93.5	10513	-236.8	-245.2	-236.2	-246.1	-233.7	-213.4	-194.9
99.5	10741	-243.3	-235.7	-223.1	-238.1	-226.0	-210.1	-195.1
104.5	10894	-238.4	-249.3	-232.0	-253.8	-229.3	-210.8	-200.3
108	11000	-230.9	-190.0	-189.2	-214.2	-229.8	-211.0	-198.2
113.5	11227	-183.0	-180.8	-186.7	-219.8	-221.5	-209.8	-193.8
124.5	11770	-174.6	-171.8	-163.0	-199.9	-213.1	-204.7	-189.5
128.5	12092	-	-	-	-	-	-	-
132.5	12464	-	-	-	-	-	-	-

Table D.4 Calculation of leaf water hydrogen isotopic composition from biomarker hydrogen isotopic composition using calibrated data from Chapter 2, where MAP = mean annual precipitation, JJA = summer precipitation, GL = Greenland-specific regression, GB = global data regression

Depth	Median Age	ε (C_{29}-MAP)	MAP GL	MAP GB	JJA GL	JJA GB
0	0	-109.5	-103.1	-112.0	-90.0	-91.1
2.5	514	-113.1	-109.6	-115.9	-94.1	-94.8
5.5	1171	-110.0	-104.0	-112.5	-90.5	-91.5
10.5	1923	-111.4	-106.5	-114.1	-92.1	-93.0
15.5	2498	-106.7	-97.9	-108.9	-86.7	-88.1
20.5	3421	-110.0	-104.0	-112.5	-90.5	-91.5
25.5	4353	-115.2	-113.5	-118.4	-96.7	-97.0
30.5	5204	-112.0	-107.7	-114.8	-92.9	-93.7
35.5	5907	-106.6	-97.7	-108.7	-86.5	-88.0
41.5	6713	-109.0	-102.1	-111.4	-89.3	-90.5
42.5	6835	-110.4	-104.8	-113.0	-91.1	-92.0
45.5	7195	-108.9	-101.9	-111.3	-89.2	-90.4
50.5	7743	-104.9	-94.6	-106.8	-84.5	-86.2
60.5	8308	-107.8	-100.0	-110.1	-88.0	-89.3
65.5	8504	-105.4	-95.6	-107.5	-85.2	-86.8
70.5	8856	-103.6	-92.3	-105.4	-83.1	-84.9
75.5	9328	-107.6	-99.6	-109.9	-87.7	-89.0
80.5	9805	-112.9	-109.4	-115.8	-94.0	-94.6
88.5	10247	-106.5	-97.5	-108.6	-86.4	-87.9
93.5	10513	-130.2	-141.0	-135.1	-114.3	-112.7
99.5	10741	-121.5	-125.0	-125.3	-104.0	-103.6
104.5	10894	-125.2	-131.9	-129.5	-108.4	-107.5
108	11000	-125.8	-132.9	-130.1	-109.1	-108.1
113.5	11227	-116.3	-115.6	-119.6	-98.0	-98.2
124.5	11770	-106.8	-98.1	-109.0	-86.8	-88.2
128.5	12092	-	-	-	-	-
132.5	12464	-	-	-	-	-